Dissertation presented

as a partial requirement for the degree of
Doctor of Science

Measurement of Neutrino Cross Sections interactions in the Shallow Inelastic Scattering region in Hydrocarbon at $< E_\nu > \approx 6\ GeV$ in the MINERνA experiment

Gian Fredy Ricardo Caceres Vera

Advisor:
Hélio da Motta Filho

Centro Brasileiro de Pesquisas Físicas

Rio de Janeiro, December 2020

To my mother

Acknowledgements

I would like to express my gratitude to my advisor Dr. Helio da Motta for giving me the opportunity to work in the MINERνA collaboration, for the advices and support given, and for the trust placed in me to do this work.

To all the MINERνA collaboration, specially to Dr. Jorge Morfin for all the support and the insightfull physics conversations.

I want to thank to the professors at the Centro Brasileiro de Pesquisas Físicas and to CAPES for the scholarship (2016-2020).

My most profound gratitude goes to my family, whose love and guidance are with me in whatever I pursue.

Abstract

MINERνA (Main Injector Experiment for ν-A) is a dedicated neutrino scattering experiment at Fermilab Muon Neutrino beamline (NuMI beamline), aimed to understand the nature of neutrino-nucleus interactions. MINERνA identifies nuclear effects and tests neutrino interaction models, measures exclusive and inclusive final states and their correlations with leptons, and also characterizes neutrino interactions for oscillation experiments.

In this dissertation, the neutrino differential cross section in the Shallow Inelastic Scattering region in hydrocarbon scintillator at neutrino energy $< E_\nu > \approx 6$ GeV as a function of Bjorken-x is presented. Significant differences between the simulation and SIS data are observed at low Bjoken-x values. These measurements are the world's first neutrino-SIS cross sections to be produced.

Contents

List of Figures

List of Tables

Chapter 1

Introduction

In the last decades neutrino physics has become a very active and exciting research field. Many experiments around the world are currently trying to understand the properties of these elusive particles that play an important role in various branches of subatomic physics, astrophysics and cosmology. Neutrinos are very abundant in the universe, second only to photons, and they are very difficult to detect. To have an idea, to reliably stop a neutrino it is calculated that a few light-years of solid lead would be needed. Experiments have confirmed there are three flavours of neutrinos and that neutrinos oscillate from one flavour to another as they travel through space. Neutrino oscillation phenomenom is only possible if neutrinos have mass, which is not predicted by the standard model of particle physics. Therefore, the understanding of the neutrino properties will surely expand the human knowledge and will provide a greater view of the universe.

Chapter 2 presents the relevant neutrino physics theory. Chapter 3 details Shallow Inelastic Scattering (SIS), the relevant scattering for this analysis. Chapter 4 presents the MINERvA detector and experiment. Chapter 5 describes how we reconstruct the data collected in the detector. Chapter 6 shows the background studies necessary for the analysis. Chapter 7 explains the systematics that affect our results. Chapter 8 details the unfolding process. Chapter 9 finally presents the the cross section calculation. Chapter 10 presents the conclusion and future perspectives.

Appendixes A, B, C, D, E, F, and G detail some of the aspects of the analysis. Apendix H resumes the author's contribution to the MINERνA experiment.

Chapter 2

Introduction to Neutrino Physics

2.1 Brief History

The study of the β decay gave the first hint of the existence of neutrinos. In the early twentieth century it was believed that the energy spectrum of the β decay was discrete. However, in 1911, Von Bayer, Otto Hahn and Lise Meitner ran an experiment that suggested that the β decay energy spectrum had a continuous instead of discrete spectrum [1] as the one observed in the alpha decay. In 1927, Ellis and Wooster confirmed that in the β decay the kinetic energy spectrum of the emitted electrons was really continuous [2]. This was contradicting the energy conservation law.

In 1930, in order to resolve this contradiction and preserve the conservation of energy principle Wolfgang Ernst Pauli proposed in his famous letter to the "Dear Radioactive Ladies and Gentlemen" addressed to the participants of the physics conference in Tubingen [3] the existence of a spin $\frac{1}{2}$ particle that had charge zero which he called "neutron". He was, however, skeptical about his idea saying "I have done something very bad today by proposing a particle that cannot be detected; it is something no theorist should never do".

In 1932, James Chadwick discovered a neutral particle of mass similar to that of the proton which was also named "neutron" [4]. In 1934 Enrico Fermi succeeded on developing a β decay theory integrating the particle proposed by Pauli [5]. He understood Pauli's particle should have mass of the order of the mass of an electron so he named it "neutrino" (Italian for "small neutron").

It took 22 years for the first observation of neutrinos made by Reines and Cowan [6], [7], [8], in 1956. They used the antineutrino flux of the order of 10^{12} $cm^{-2}s^{-1}$ coming from a nuclear reactor. Antineutrinos coming from beta decays were detected via inverse beta decay (equation 2.1), where positrons were detected in a tank full of liquid scintillator.

$$\overline{\nu}_e + p \rightarrow n + e^+, \tag{2.1}$$

In 1958 Goldhaber measured the left helicity of neutrinos [9] and Davis was able to discriminate ν from its antiparticle $\overline{\nu}$ [10]. In 1959 Chien-Shiung Wu discovered parity violation in weak interaction [11] when a preferred direction of the produced electrons respect to the spin of the ^{60}Co nuclei was observed in the β decay of ^{60}Co.

In 1962 Schwartz, Lederman, Steinberg and colleagues published results of the first accelerator produced neutrinos at Brookhaven National Laboratory. They showed that neutrinos produced by the charged pions beam interacted producing only muons[12]. This was evidence of a new kind of neutrino: the muon neutrino ν_μ.

In 1973 neutral current induced process was announced by the Gargamelle bubble chamber collaboration at CERN [13] and later confirmed by the same collaboration in 1974.

In the seventies, studies of solar neutrinos began measuring the solar neutrino flux. In 1968 Davis' studies showed a discrepancy between the measured solar neutrino flux and the theoretical prediction [14]. This was known as the "solar neutrino problem". The same discrepancy was also observed in atmospheric neutrino fluxes[1] and was known as the "atmospheric neutrino anomaly". In 1988, for the first time, neutrino oscillations were suggested as the reason for this discrepancy in the results given by the Kamiokande detector [15].

In 1967, Gribov And Pontecorvo considered a scheme of neutrino mixing and oscillations [16] that explained the flux discrepancy of the solar neutrinos. Mass terms had to be included in order to explain the oscillation of neutrinos[2].

Mainly because of the τ short life time it was not until 2000 that the ν_τ could be observed at the Fermilab DONUT experiment[3] [17]. There is no doubt new surprises and discoveries are ahead. Many neutrino facilities around the world have been built to perform detailed studies of neutrinos.

Along the time, the studies of neutrino interactions with matter and oscillation phenomena have been an amazing journey on creativity and innovation of mankind willing to better understand the nature of what we are made of. A new era of physics has started looking for expanding the limits of our understanding of the universe.

[1] Measurements made in 1986 by IMB [18] and Kamiokande [19] did not have a zenith angle dependence and were not given much attention.

[2] Neutrino oscillation is not predicted by the Standard Model and it is then an indication of a physics beyond the Standard Model.

[3] Long before the discovery of the ν_{tau} the existence of just three light neutrinos was predicted at Large Electron-Positron collider (LEP) at CERN [20], [21], [22], [23].

2.2 The Standard Model

The standard model is the theory that describes the elementary building blocks of matter and how they interact. However it is incomplete and describes just three of the four forces known in nature[4]:electromagnetic, strong and weak. The Standard Model describes nature in terms of elementary particles (quarks and leptons) and particles that mediate the interactions (bosons).

There are six quarks and six leptons (all of them fermions that have spin 1/2), that come in three generations or pairs. The first generation consists of the lightest and most stable particles whereas the heavier and less stable particles belong to the second and third generations. The quarks generations are: up(u) and down(d); strange (s) and charm (c); bottom (b) and top (t). Leptons can be charged (e, μ and τ) and neutral (ν_e, ν_μ and ν_τ). Figure 2.1 shows the three generations of the elementary particles.

$$\begin{pmatrix} u \\ d \end{pmatrix} \begin{pmatrix} s \\ c \end{pmatrix} \begin{pmatrix} b \\ t \end{pmatrix}$$

$$\begin{pmatrix} e \\ \nu_e \end{pmatrix} \begin{pmatrix} \mu \\ \nu_\mu \end{pmatrix} \begin{pmatrix} \tau \\ \nu_\tau \end{pmatrix}$$

Figure 2.1: Elementary particles generations: quarks (top) and lepton (bottom). Each charged lepton (e, μ and τ is associated to a corresponding neutral lepton (ν_e, ν_μ and ν_τ).

There are four bosons (spin 1) that mediate the forces of the Standard Model: the gluon (g) that mediates the strong force; the photon (γ) that mediates the electromagnetic force; the $W^\pm$ and Z bosons that mediate the weak force. The fifth boson, the Higgs boson (H), has spin 0 and is the responsible for giving mass to the other particles, except for neutrinos that are massless in the Standard Model.

The 16+1 fundamental particles are summarized in Table 2.1.

2.2.1 Neutrinos in the Standard Model

Neutrinos are the only fermions in the Standard Model that interact only by means of the weak interaction. Two different processes can be observed: Neutral Current interaction (NC) mediated by the boson Z^0; and Charged Current interaction (CC) mediated by the bosons $W^\pm$. In a NC interaction the outcoming neutrino is the same incoming neutrino, however in a CC interaction there is no outcoming neutrino and a charged lepton is produced instead. In a CC interaction the interacting neutrino and the lepton produced are from the same generation,

[4]Gravitation is not included in the Standard Model.

QUARKS		
Quarks	Mass	Electric charge
up (u)	$2.16^{+0.49}_{-0.26}$ MeV/c^2	$+\frac{2}{3}$
down (d)	$4.67^{+0.48}_{-0.17}$ MeV/c^2	$-\frac{1}{3}$
strange (s)	93^{+11}_{-5} MeV/c^2	$-\frac{1}{3}$
charm (c)	1.27$\pm$0.02 GeV/c^2	$+\frac{2}{3}$
bottom (b)	$4.18^{0.03}_{0.02}$ GeV/c^2	$-\frac{1}{3}$
top (t)	172.9 $\pm$ 0.4 GeV/c^2	$+\frac{2}{3}$
LEPTONS		
Leptons	Mass	Electric charge
electron (e)	0.5109989461 $\pm$ 0.0000000031 MeV/c^2	-1
electron neutrino (ν_e)	$<$ 460 eV/c^2	0
muon (μ)	105.6583745 $\pm$ 0.0000024 MeV/c^2	-1
muon neutrino (ν_μ)	$<$ 0.19 MeV/c^2	0
tau (τ)	1776.86 $\pm$ 0.12 MeV/c^2	-1
tau neutrino (ν_τ)	$<$ 18.2 MeV/c^2	0
BOSONS		
Bosons	Mass	Electric charge
photon(γ)	$< 1 \times 10^{-18}$ eV/c^2	0
W$^\pm$	80.379$\pm$ 0.012 GeV/c^2	$\pm$1
Z^0	91.1876 $\pm$ 0.0021 GeV/c^2	0
gluon (g)	0	0
Higgs	125.35 $\pm$0.15 GeV/c^2	0

Table 2.1: Particles in the Standard Model [24].

thus we know to which of the three families the interacting neutrino belongs by the kind of lepton produced in the CC interaction.

2.2.2 Helicity

Helicity is the projection of the spin onto the direction of the momentum. As shown in Figure 2.2 the particle helicity can have two possible states: spin and momentum having same directions (positive helicity); spin and momentum having opposite directions (negative helicity). For particles having mass any of these states can be possible because the momentum depends of the relative velocity to the frame of reference. However, left-handed antineutrinos and right-handed neutrinos have never been observed, and it was in 1957 that Goldhaber determined that neutrinos are left handed while antineutrinos are right handed [9].

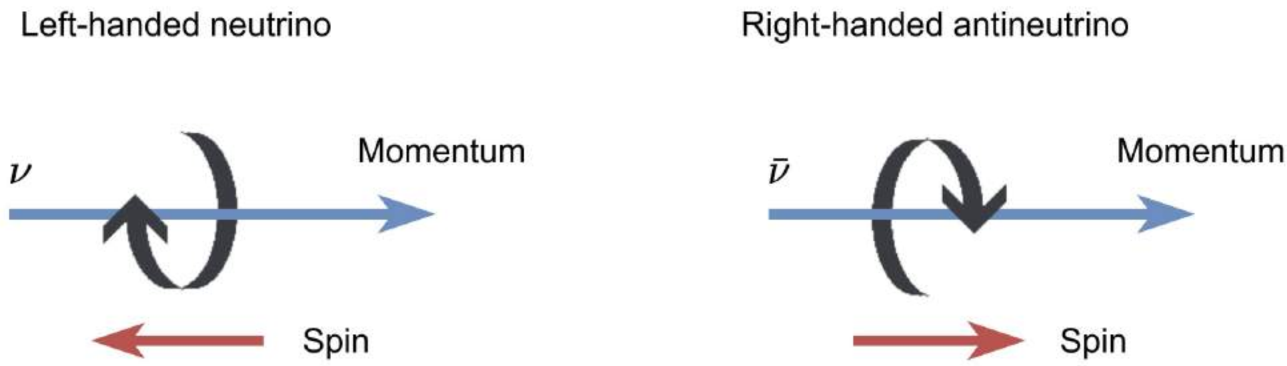

Figure 2.2: In the Standard Model of particle physics, for neutrinos the spin is always opposite the linear momentum, this is referred as "left-handed", where as the antineutrinos are always "right-handed".

2.2.3 Neutrino Oscillation and Masses

Neutrino oscillations are possible only if neutrinos are massive. Each neutrino flavor (ν_e, ν_μ, ν_τ) is understood as a combination of three mass states[5] (ν_1,ν_2,ν_3). The flavour eigenstates are related to the mass eigenstates by the Pontecorvo-Maki-Nakagawa-Sakata (PMNS) matrix,

$$\begin{pmatrix} \nu_e \\ \nu_\mu \\ \nu_\tau \end{pmatrix} = \begin{pmatrix} U_{e1} & U_{e2} & U_{e3} \\ U_{\mu1} & U_{\mu2} & U_{\mu3} \\ U_{\tau1} & U_{\tau2} & U_{\tau3} \end{pmatrix} \begin{pmatrix} \nu_1 \\ \nu_2 \\ \nu_3 \end{pmatrix} \tag{2.2}$$

[5]This idea was first introduced by Gribov and Pontecorvo [16].

with

$$U = \begin{pmatrix} c_{12}c_{13} & s_{12}c_{13} & s_{13}e^{-i\delta} \\ -s_{12}c_{23} - c_{12}s_{23}s_{13}e^{i\delta} & c_{12}c_{23} - s_{12}s_{23}s_{13}e^{i\delta} & s_{23}c_{13} \\ s_{12}s_{23} - c_{12}c_{23}s_{13}e^{i\delta} & -c_{12}c_{23} - s_{12}c_{23}s_{13}e^{i\delta} & c_{23}c_{13} \end{pmatrix} \tag{2.3}$$

where $c_{ij} = cos(\theta_{ij})$ and $s_{ij} = sen(\theta_{ij})$ are the cosine and sine of the three mixing angles and δ is a charge-parity (CP) violating phase of the oscillation which has yet to be measured.

When a neutrino is produced with a specific flavor, its quantum state evolves to a combination of mass states with the proportions oscillating in time. The probability of detecting a specific neutrino flavor depends on the amplitude of the respective mass state. The evolution in time of the mass eigenstate of a neutrino with energy E_i is dictated by:

$$|\nu_i(t)\rangle = e^{-iE_it}|\nu_i(0)\rangle. \tag{2.4}$$

Using equation 2.2 and 2.3, and considering for simplicity a system consisting of two neutrino flavors ν_α ans ν_β, we can write their states as superposition of mass eigenstates ν_1 and ν_2 with masses m_1 and m_2 respectively:

$$|\nu_\alpha\rangle = |\nu_1\rangle cos\theta + |\nu_2\rangle sin\theta, \tag{2.5}$$

$$|\nu_\beta\rangle = -|\nu_1\rangle sin\theta + |\nu_2\rangle cos\theta, \tag{2.6}$$

where θ is the neutrino mixing angle. The evolution in time of the state is dictated by the free Hamiltonian. The state at $t = 0$ is

$$|\nu_\beta(t = 0)\rangle = -|\nu_1\rangle sin\theta + |\nu_2\rangle cos\theta \tag{2.7}$$

and at time t the state will be given by

$$|\nu_\beta(t)\rangle = -|\nu_1\rangle sin\theta e^{-\frac{iE_1t}{\hbar}} + |\nu_2\rangle cos\theta e^{-\frac{iE_2t}{\hbar}}. \tag{2.8}$$

We take $\hbar$=c=1 and consider the extreme relativistic approximation for very small neutrino masses $E_{1,2} = \sqrt{(p^2 + m_{1,2}^2)} \sim p + \frac{m_{1,2}^2}{2p}$. Then we have for the state in any time t,

$$|\nu_\beta(t)\rangle = -|\nu_1\rangle sin\theta e^{-i(p+\frac{m_1^2}{2p})t} + |\nu_2\rangle cos\theta e^{-i(p+\frac{m_2^2}{2p})t}. \tag{2.9}$$

Using $\Delta m^2 = m_2^2 - m_1^2$ and the relativistic substitution $p = E$, the probability of finding a different neutrino flavor is:

$$P(\nu_\beta \to \nu_\alpha, t) = |\langle\nu_\alpha|\nu_\beta(t)\rangle|^2 = sin^2(2\theta) sin^2(\frac{\Delta m^2 L}{4E}) \tag{2.10}$$

The last line is valid for highly relativistic particles with L being the distance traveled by the neutrino. For a given Δm^2 the probability of oscillation will change as one moves away from the detector, or scans over different neutrino energy. Experimentally we have the control to choose the L and E parameters and we can build experiments to be maximally sensitive to the oscillation propability.

In the three neutrino flavour system we have three squared mass differences Δm^2_{12}, Δm^2_{13}, Δm^2_{23}. Because only mass square differences appear in the probability definitions, measuring oscillation probabilities can only tell that at least one of the neutrinos has non-zero mass. The most likely way to explain how neutrinos got their mass is through the seesaw mechanism [25], which predicts the existence a right handed neutrino of much higher mass and that the ratio between this and light left-handed neutrino mass is constant. Thus, the lighter the left-handed neutrino is, the heavier the right-handed neutrino is. The heavy righ-handed neutrino have yet to be measured. In the Standard Model the neutrinos are massless, which is why the understanding of neutrino interactions will surely reveal new physics.

2.3 Neutrino Interactions

In the neutrino energy region of a few GeV a neutrino scatters off a nucleon or an entire nucleus via Charged Current (CC) or Neutral Current (NC) interaction. CC and NC interactions are mediated by $W^{\pm}$ and Z^0 bosons respectively. In this section we briefly discuss the processes: Elastic and Quasielastic, Resonant Meson production via Baryon Resonances, Non-resonant meson production, Coherent Pion Production, Deep Inelastic Scattering (DIS).

2.3.1 Elastic and Quasielastic scattering

In both of these scatterings the neutrino scatters off an entire nucleon. In the case of a CC interaction the process is called "Quasielastic scattering" and in the case of a Neutral Current interaction it is called "Elastic scattering". These interactions for neutrinos are as follows:

$$(CC)\ \nu_l + n \rightarrow l^- + p \tag{2.11}$$

$$(NC)\ \nu_l + N \rightarrow \nu_l + N. \tag{2.12}$$

Where l^- refers to any of the charged leptons e^-, μ^-, τ^-, n to neutron, p to proton and N to any nucleon. The Charged Current Quasielastic interaction is the more dominant for $E_\nu < 2$ GeV. The CC antineutrino interaction produce the respective positive lepton, while the NC (neutrino and anitneutrino) interactions are not that easily identified.

2.3.2 Coherent Pion Production

One type of interaction that produces pions is that of the neutrino interacting coherently with an entire nucleus which remains unchanged in its ground state after the interaction.No nuclear breakup occurs; however, the nucleus gets excited, decays and come back to its ground state by emitting a Pion. The outgoing pion and lepton tend to go in the same direction as the incoming neutrino. The CC and NC neutrino interactions are as follows:

$$(CC)\ \nu_l + A \rightarrow l^- + A + \pi^+ \tag{2.13}$$

$$(NC)\ \nu_l + A \rightarrow \nu_l + A + \pi^0. \tag{2.14}$$

Where A is the nucleus in its ground state.

2.3.3 Resonant Meson production via Baryon Resonances

Neutrino-nucleus interaction can excite baryon resonances which decay into a nucleon and a meson or more in the final state. In the few GeV energy range the intermediate state is dominated by the $\Delta(1232)$ resonance which mainly decays into a nucleon and a pion. The CC and NC for resonant single pion production are as follows:

$$(CC)\ \nu_l + N \rightarrow l^- + \Delta \rightarrow l^- + N^{'} + \pi^{'} \tag{2.15}$$

$$(NC)\ \nu_l + N \rightarrow \nu_l + \Delta \rightarrow \nu_l + N^{'} + \pi^{'}. \tag{2.16}$$

Here $N^{'}$ refers to a nucleon different to the original N. A variety of final states can exist and the $\pi^{'}$ produced could be π^-, π^0 or π^+. These two types of interactions are known as CC1π and NC1π interactions.

2.3.4 Non-resonant Meson production

Non-resonant meson production is also characterized by one or more mesons in the final state; however, these mesons are not coming from baryon resonances decays but created at the interaction vertex. The CC and NC neutrino interactions for single pion production are as follows:

$$(CC)\ \nu_l + N \rightarrow l^- + N^{'} + \pi^{'} \tag{2.17}$$

$$(NC)\ \nu_l + N \rightarrow \nu_l + N^{'} + \pi^{'}. \tag{2.18}$$

Here $N^{'}$ refers to a nucleon different to the original N. A variety of final states can exist and the $\pi^{'}$ produced could be π^{-}, π^{0} or π^{+}. These two types of interactions are known as non-resonant CC1π and NC1π interactions. The Feynman diagram for non-resonant CC1π production is shown in figure 2.3.

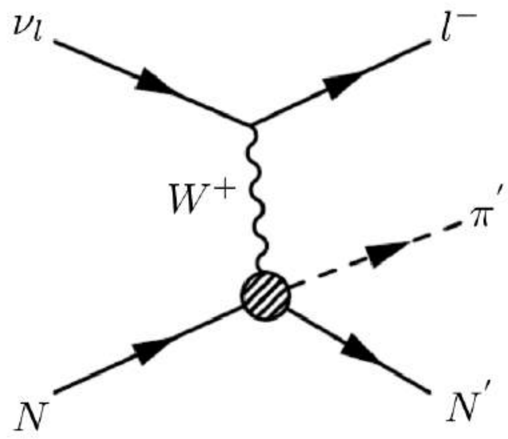

Figure 2.3: Feynman diagram for non-resonant CC1π production

2.3.5 Shallow Inelastic Scattering (SIS)

Along the SIS region non-resonant meson production increases, resonant meson production decreases and Deep Inelastic Scattering begins. The SIS region is, therefore, a transition region where the physics of hadrons meet the physics of quarks. We give a technical and experimental definition of the SIS region in more detail in chapter 3.

2.3.6 Deep Inelastic Scattering (DIS)

In this region the neutrino interacts with quarks instead of with nucleus or nucleons. The four-momentum transferred to the nucleus is known as q in Mandelstam invariants [26]. The $-q^2$ value (this quantity will be refered just as four-momentum transfer in the rest of the text) determines the probing capacity of the interaction and, therefore, an interaction with higher four-momentum transfer is more likely to occur with quarks in the nucleon (figure 2.4). The high momentum transfer breaks the nucleon and the struck quark produces hadrons in the final state. The CC and NC neutrino interactions are as follows:

$$\nu_l + N \to l^- + hadrons \tag{2.19}$$

$$\nu_l + N \to \nu_l + hadrons. \tag{2.20}$$

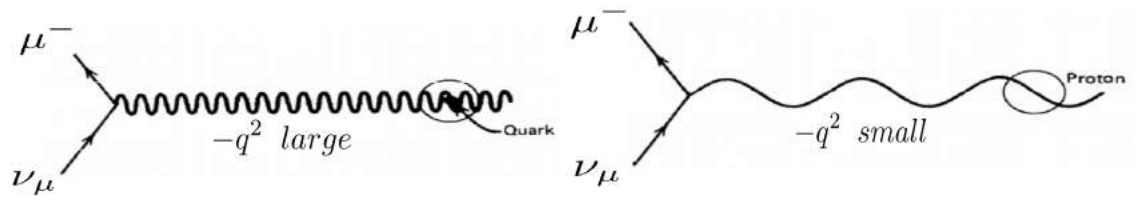

Figure 2.4: Probing capacity of the four-momentum transferred ($-q^2$) in a Charged Current ν_μ interaction

Figure 2.5 shows Feynman diagrams for some CC proccesses and Figure 2.6 shows current neutrino and antineutrino CC Cross Sections. In figure 2.6 the non-resonant and resonant pion production predictions are labelled 'RES', and the deep inelastic scattering event prediction are labelled 'DIS'. Both predicitons overlap in the SIS region and it is important to highlight that there is no measured data for this region yet.

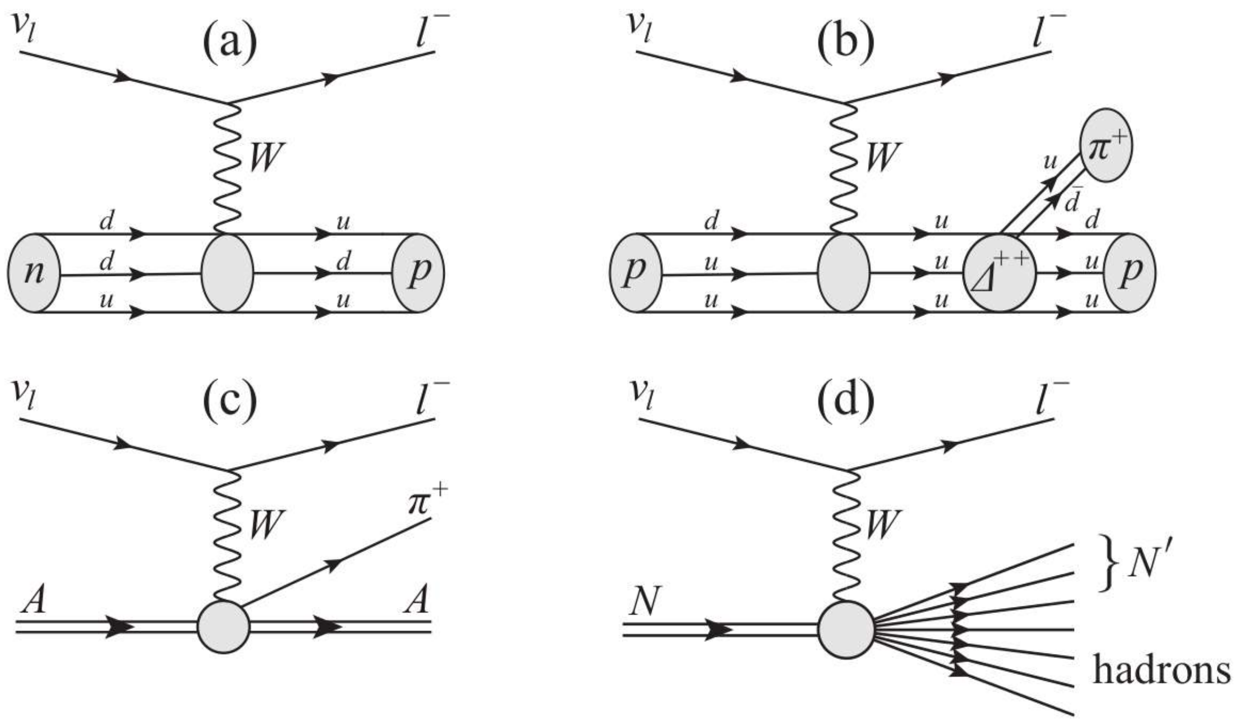

Figure 2.5: Feynman diagrams for some CC neutrino interactions. (a) Quasielastic (b)Resonant production (c)Coherent Pion production (d)Deep Inelastic Scattering.

2.4 Neutrino Oscillation Experiments

In this section it is shown important measurements that led to the discovery of neutrino oscillations. A summary of neutrino oscillation parameters measurements for different neutrino

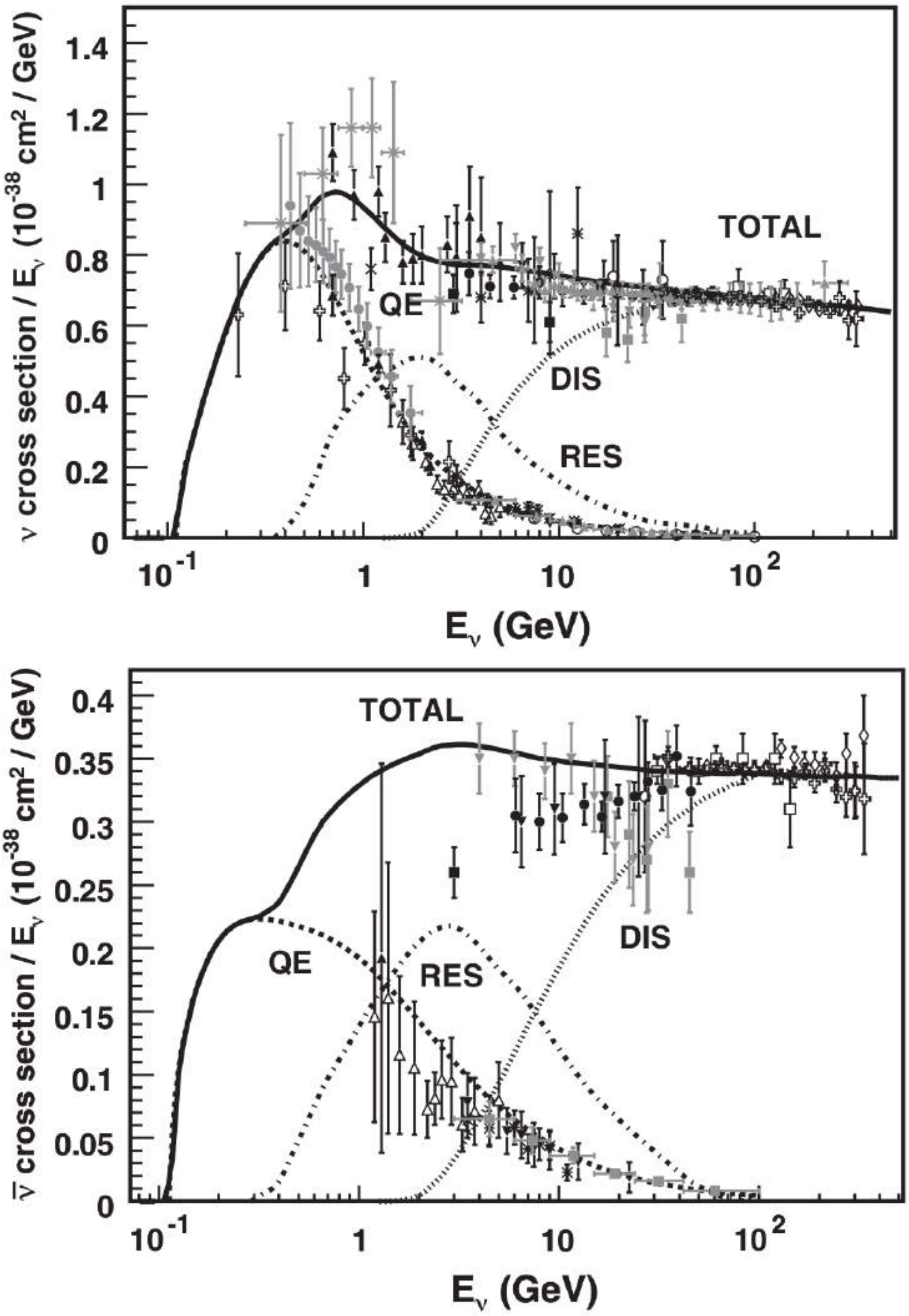

Figure 2.6: Existing measurements for total neutrino and antineutrino per nucleon CC cross sections (for an isoscalar target) and additional CC inclusive data for lower energy as a function of energy are shown [27]. There are no cross sections measurement for the RES and DIS simulations, and contributions from quasielastic scattering (dashed), resonance production (dot-dashed), and deep inelastic scattering (dotted) are predicted by the NUANCE generator [28] are shown.

flux sources is presented.

2.4.1 Solar Neutrinos

The first hint of neutrino oscillations came from the Homestake experiment headed by Raymond Davis. The Homestake Solar Neutrino detector was designed to be sensitive to the electron neutrino via $\nu_e +^{37} Cl \rightarrow e^- +^{37} Ar$, where radioactive isotopes of Argon-37 were identified and counted to detect the electron neutrino [14]. The experiment collected data from the late 1960s to 1996. The final results for the production of Argon atoms was [29] $2.56 \pm 0.16(stat) \pm 0.16(syst)$ SNU[6]. Prediction of the Standard Solar Model (model BP04) is $8.5^{+1.8}_{-1.8}$ SNU [30]. This discrepancy, as mentioned in Section 2.1, was called the "solar neutrino problem".

The solar neutrino experiment Sudbury Neutrino Observatory (SNO) started observations in 1999 and completed in 2006. The SNO was a water-Cherenkov detector that used ultra-pure heavy water (D_2O) as neutrino target. This experiment was sensitive to three reactions:

$$\nu_x + e^- \rightarrow \nu_x + e^- \ (elastic\ scattering), \tag{2.21}$$

$$\nu_e + d \rightarrow e^- + p + p \ (\nu_e\ charged - current), \tag{2.22}$$

$$\nu_x + d \rightarrow \nu_x + p + n \ (neutral\ current). \tag{2.23}$$

The CC reaction is only sensitive to electron neutrino and the NC reaction is equally sensitive to all neutrino flavors. The elastic scattering (ES) reaction is sensitive to all neutrino flavors but less sensitive to ν_τ and ν_μ. In 2001 a first measurement of solar neutrino flux deduced from ES [$\phi^{ES}(\nu_x)$] and CC [$\phi^{CC}(\nu_e)$] reactions showed that $\phi^{CC}(\nu_e) < \phi^{ES}(\nu_x)$ suggesting electron neutrinos change into other active flavor [31]. In 2002 these fluxes were updated and the flux deduced from the NC reaction was measured [32]. These measured fluxes, in $10^6\ cm^{-2}sec^{-1}$, were:

$$\phi^{SNO}_{CC} = 1.76^{+0.06}_{-0.05}(stat)^{+0.09}_{-0.09}(syst), \tag{2.24}$$

$$\phi^{SNO}_{ES} = 2.39^{+0.24}_{-0.23}(stat)^{+0.12}_{-0.12}(syst), \tag{2.25}$$

$$\phi^{SNO}_{NC} = 5.09^{+0.44}_{-0.43}(stat)^{+0.46}_{-0.43}(syst), \tag{2.26}$$

[6] 1 SNU = 1 Solar Neutrino Unit = $10^{-36} captures \times s^{-1}\ per\ atom$.

The measurement of the total flux ϕ_{NC}^{SNO} confirmed that ν_e indeed oscillates to other neutrino flavors.

The Super-Kamiokande detector holds 50,000 tons of water and detects charged particles via Cherenkov radiation. Here, solar neutrinos interactions are detected via the elastic scattering reaction. The neutral current reaction can measure interaction rate of any neutrino flavor,

$$\nu_x + e^- \rightarrow \nu_x + e^-(via\ neutral - current). \tag{2.27}$$

However the sensitivity to ν_e neutral current interaction,

$$\nu_e + e^- \rightarrow \nu_e + e^- \tag{2.28}$$

is higher relative to ν_τ and ν_μ neutral current interactions, because it is enhanced by the ν_e charged current interactions measured. For events over the 5 MeV threshold in Super-Kamiokande the measured ^8B flux was $(2.35 \pm 0.02(stat.) \pm 0.08(syst.))10^6 cm^{-2} sec^{-1}$ [33] and the computed theoretical flux was $(5.69 \pm 1.0)10^6 cm^{-2} sec^{-1}$ [34]. This discrepancy agrees with results from other experiments.

2.4.2 Neutrinos from Nuclear Reactors

In 2002 the Kamioka Liquid-scintillator Anti-Neutrino Detector's (KamLAND) results gave the first remarkable evidence on neutrino oscillation coming from nuclear reactors [35]. The liquid scintillator was developed by the KamLAND Research Center for Neutrino Science group [36] and it detected electron anti-neutrinos via inverse β decay:

$$\overline{\nu}_e + p \rightarrow e^+ + n. \tag{2.29}$$

The produced positron is detected in a scintillator and approximately 200 μs later the neutron is captured via,

$$n + p \rightarrow d + \gamma\ (2.2\ MeV). \tag{2.30}$$

This time delay between the initial scintillating light produced by the positron and the latter photon is a robust signature of electron anti-neutrino detection. The ratio of the observed to the no-oscillation expected energy spectra for the electron anti-neutrino events are shown in figure 2.7. The electron anti-neutrinos for KamLAND come from comercial nuclear reactors in Japan whose typical energy is a few MeV and the average distance from the reactors to the detector was about 180 km [37].

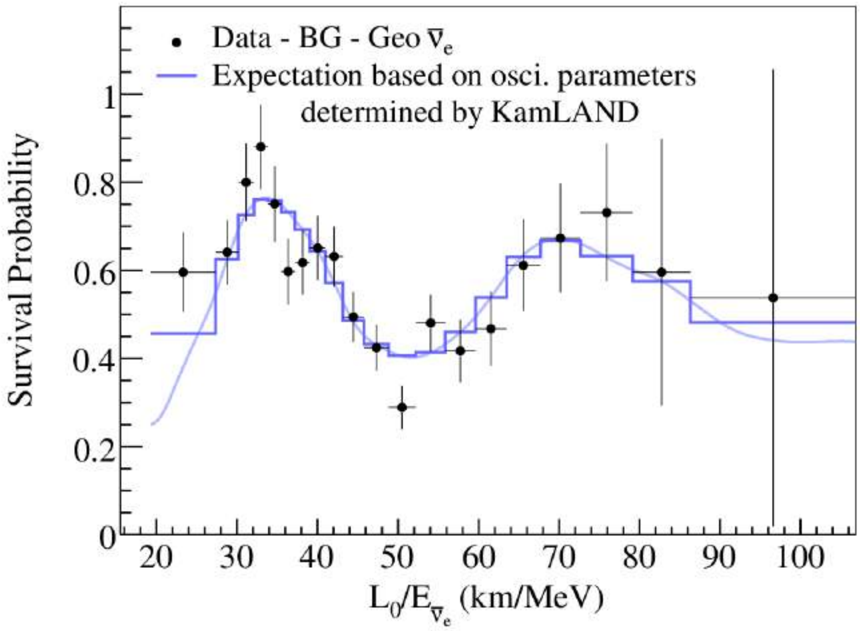

Figure 2.7: KamLAND ratio of the observed to the no-oscillation expected events for the electron anti-neutrino events as a function of $\frac{L_0}{E_{\overline{\nu}_e}}$ where $L_0 = 180km$.

CHOOZ [38] and Palo Verde [39] were two first-generation kilometer-baseline reactor experiments located in France and United States, respectively. The objective of these experiments was to measure the θ_{13} oscillation parameter. CHOOZ could measure an upper limit of $sin^2(2\theta_{13}) < 0.10$ at 90% confidence level. Baseline reactor experiments as Double CHOOZ [40], [41] in France, RENO [42] in Korea and Daya Bay [43], [44] in China that measured a better value of $sin^2(2\theta_{13}) = 0.0841 \pm 0.0033$.

2.4.3 Atmospheric Neutrinos

Atmospheric neutrinos are produced by decays of kaons and pions produced by interactions of cosmic rays with nuclei at Earth's atmosphere. At these high energy interactions, many pions and less abundant Kaons decay via:

$$\pi^{\pm}(K^{\pm}) \rightarrow \mu^{\pm} + \nu_{\mu}(\overline{\nu}_{\mu}) \tag{2.31}$$

$$\mu^{\pm} \rightarrow e^{\pm} + \nu_e(\overline{\nu}_e) + \overline{\nu}_{\mu}(\nu_{\mu}). \tag{2.32}$$

However Kaons are responsible for higher energy neutrinos than those produced by Pion decays [45]. This reaction chain produces approximately two muon neutrinos per one electron neutrino.

The Super-Kamiokande experiment confirmed Muon neutrino disappearance due to neutrino oscillations. But despite a decrease in the events ratio $\frac{\nu_\mu}{\nu_e}$ relative to the predicted events was observed, the strong argument for Muon neutrino oscillations came from the distribution of events as a function of the zenith angle [46], as shown in Figure 2.8. The decrease in the upward-going μ-like events suggested μ neutrinos oscillated when traveling through the earth towards the detector. The electron neutrinos distribution was as predicted. Comparison with Kamiokande data confirmed this decrease was due to the oscillation $\nu_\mu \rightarrow \nu_\tau$. Subsequent data from Super-Kamiokande SK-I, SK-II, SK-III upgrades provided more statistics and confirmed this result.

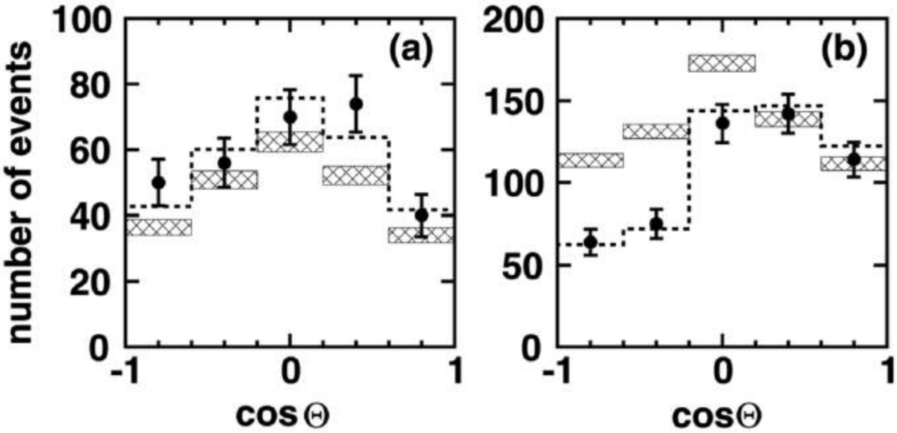

Figure 2.8: Zenith angle distributions for atmospheric neutrinos events. The left and right panel shows the distributions for e-like and μ-like events, respectively. Θ is the zenith angle, and $cos\Theta = 1$ and $cos\Theta = -1$ is vertically downward-going and upward-going, respectively.

At the time the Super-Kamiokande's data confirmed neutrino oscillations, two other experiments that measured atmospheric neutrinos, Soudan-2 [47], [48] and MACRO [49], [50] showed also in their data a ν_μ deficit dependent of the zenith angle.

2.4.4 Neutrinos from Accelerators

Accelerator long-baseline neutrino experiments consist of two detectors separated a long distance one from each other aligned on- or off-axis with the neutrino beam produced in the accelerator. Man-made neutrino beams have the chief advantage on reducing systematics errors of measurements of neutrino oscillation parameters. However, high energy neutrino beams present serious experimental challenges for neutrino oscillation experiments[7].

[7]It must, for instance, be able to produce a sufficient number of interactions a few hundreds kilometers away from the source.

T2K (Tokai to Kamioka) is a neutrino oscillation experiment [51] that uses the muon neutrino beam produced at J-PARC facility and the Super-Kamiokande detector located 295 km away to study mainly oscillations $\nu_\mu \to \nu_e$. T2K is the successor of the K2K (KEK to Kamioka) experiment [52] that was a neutrino experiment that operated from 1999 to 2004 and used the KEK 12 GeV proton synchrotron (average muon neutrino energy ≈1.3 GeV) and the Super-Kamiokande detector located 250 km away. One of the goals of K2K was the verification of the Super-Kamiokande's measurements on atmospheric neutrino oscillations presented in 1998.

The Near Detectors of MINOS (Main Injector Neutrino Oscillation Search) [53] and NOνA (NuMI Off-Axis ν_e Appearance) [54],[55],[56] experiments are located at Fermilab, both exposed to the NuMI beam which is a muon neutrino beam of a few GeV energy (from 2 to 10 GeV) produced at Fermilab (chapter 4). The MINOS experiment has its Far Detector 735 km away at the Soudan Underground Laboratory in Minnesota and uses the NuMI beam to study disappearance of muon neutrinos. The NOνA experiment has its Near and Far detectors both located 14mrd off-axis the NuMI beam 810 km away from each other. NOνA's as main goal is the measurement of electron neutrino appearance applying an "off-axis" technique that provides a narrow peak in the energy spectrum.

The CNGS beam is a muon neutrino beam produced at CERN. At the Gran Sasso Laboratory located in Italy, 730 km away, are located the OPERA (Oscillation Project with EmulsiontRacking Apparatus) and ICARUS (Imaging Cosmic And Rare Underground Signals) experiments. Both OPERA and ICARUS had as main goal the study of ν_τ appearance.

Chapter 3

Shallow Inelastic Scattering (SIS) interactions

In order to define the SIS interaction some important variables must be defined first. Let's consider a charged current muon neutrino interaction as shown in figure 3.1.

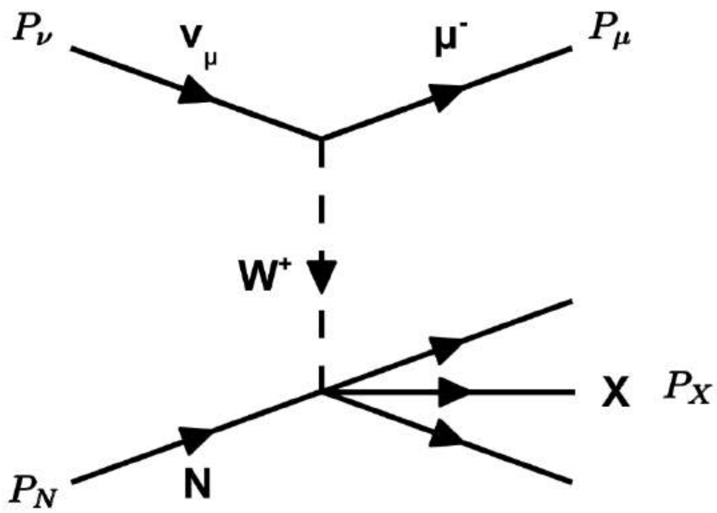

Figure 3.1: Charged current muon neutrino interaction with the four-momenta of the neutrino (P_ν), produced muon (P_μ), nucleon target (P_N) and hadron products (P_X)

Using four-momentum conservation,

$$P_\nu + P_N = P_\mu + P_X \tag{3.1}$$

the four-momentum transfer $-q^2 = -|p_\nu - p_\mu|^2$ is calculated as,

$$Q^2 = -q^2 = 2E_\nu(E_\mu - p_\mu cos\theta_\mu) - m_\mu^2 \tag{3.2}$$

where E_ν is the neutrino energy, E_μ is the muon energy, p_μ is the muon momentum, θ_μ is the muon angle with respect to the incoming neutrino direction and m_μ is the muon mass. Assuming the target nucleon is at rest in the lab frame the hadronic invariant mass is calculated as,

$$W^2 = P_X^2 = (P_\nu + P_N - P_\mu)^2 \tag{3.3}$$

$$W = \sqrt{M_N^2 + 2E_{had}M_N - Q^2} \tag{3.4}$$

where M_N is the mass of the nucleon and E_{had} is the hadronic energy of the system. Also, the Bjorken x and Inelasticiy y are defined in equations 3.5 and 3.6,

$$x = \frac{Q^2}{2M_N E_{had}} \tag{3.5}$$

$$y = \frac{E_{had}}{E_\nu} \tag{3.6}$$

which tells us the ratio of the four-momentum transfer to the hadronic energy and the fraction of neutrino energy transferred to the hadronic energy of the system.

The invariant mass of the final state hadronic system (W) and four-momentum transferred (Q^2) are important to define the SIS and the DIS regions. There are no definite cuts values to define DIS events but the general cuts accepted in the scientific community are $Q^2 > 1\ GeV^2$ and $W > 2\ GeV$ [57]. The high Q^2 assures the interaction has enough four-momentum transferred to resolve quarks and the high W that the interaction occurs well above the resonant region.

The cross section of the DIS interactions depends on structure functions $F(x, Q^2)$, which contain information about the nucleon structure [58]. The structure functions are strongly dependant on Bjorken x and weakly dependant on Q^2 in the DIS region, this behaviour is known as scaling. In the DIS region the Bjorken x variable can be interpreted as the fraction of the nucleon's total momentum carried by the struck quark in the infinite momentum framework [59]. Therefore, the structure functions describe the distribution of quarks inside the nucleon as a function of their fractional momenta and Bjorken x becomes a crucial variable to measure neutrino-quark interactions in the DIS region. The SIS cross section was measured as a function of Bjorken x to eventually be compared to the DIS cross section. The measurement of the DIS cross section as a function of Bjorken x in MINERνA is in progress.

3.1 Shallow Inelastic Scattering (SIS)

Technically, SIS is defined as non-resonant meson production with no quark fragmentation involved [57], and in terms of kinematics, it is defined as non-resonant meson production with small four-momentum transferred in order to avoid interactions with quarks (figure 2.4). Experimentally, non-resonant and resonant meson production cannot be distinguished and both together are separated from DIS quark-fragmented meson production with an arbitrary cut at 2 GeV in W [57] set by the scientific community. Therefore, a practical definition of SIS consists of the interactions with $M_N + M_\pi < W < 2$ GeV which includes non-resonant and resonant pion production. The GENIE [60] generator simulates events in the SIS region basically using the Bodek Yang model [61] and the Rein-Sehgal model [62] and fits to one and two pion production data (Appendix A).

3.2 Experimental SIS

An experimental SIS definition based on what MINERνA can reconstruct can be established. Analyzing an inclusive sample of the MC, figure 3.2, the first peak in our distribution is recognized as the quasielastic contribution and the second peak as composed mostly of delta resonance ($\Delta(1232)$) events that dominates pion production with the non-resonant contribution being much smaller [57]. Therefore we can displace the lower SIS signal boundary from $W = M_N + M_\pi$ to $W = 1.5$ GeV to decrease considerably delta resonance pion production measurements in our sample. The SIS region would be then defined as inclusive meson production with $1.5 < W < 2.0$ GeV (eq. 3.7), while DIS stays defined as $Q^2 > 1\ GeV^2$ and $W > 2\ GeV$.

$$\nu_\mu + N \to \mu^- + X \quad ; \quad 1.5 < W < 2.0\ GeV \tag{3.7}$$

This is the SIS definition that will be used in the rest of the this work and will be used to calculate the cross section in this analysis.

3.3 Motivation to study the SIS region

- The SIS region is a transition region where the resonant meson production decreases and the non-resonant meson production transitions into meson production where quark fragmentation involved. We are aiming to study the transition from a region described by hadron physics into a region described by quark physics. It should be noted that the need to understand this region has generated interest on studying the Quark-Hadron Duality [63], which basically suggests that the high energy inclusive hadronic cross sections, appropriately averaged over an energy range, approximately converges to the cross section calculated using quark-gluon perturbation theory.

- The measurement of the SIS cross section is important for the future Deep Underground

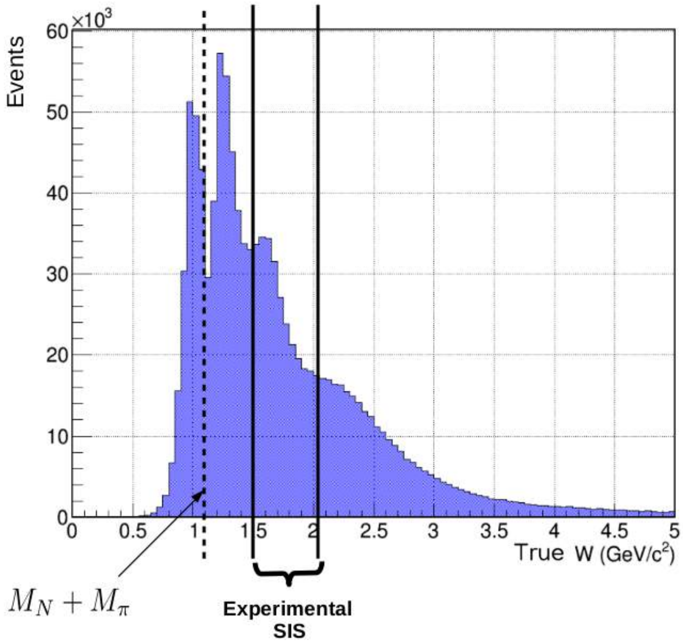

Figure 3.2: Distribution of simulated inclusive events. The dashed line correspond to the beginning of the meson production at $W \approx 1.1$ GeV and the two solid lines highlight the SIS experimental definition in the MINERνA detector.

Neutrino Experiment (DUNE) [64] because it is expected that more than 30 % of events will come from the experimentally defined DIS region and more than 50% of the events from the SIS plus DIS regions [57]. Also the atmospheric ν_l studies proposed at the Hyper-K experiment (Hyper-Kamiokande) [65] which will use Cherenkov detection technology with a water target will also have significant SIS and DIS contributions.

- Different Monte Carlo neutrino event generators such as NEUT [66], NuWro [67] and GENIE [60] predict different neutrino cross sections for the SIS and DIS regions, as shown in Fig 3.3. These differences emphasize the importance of the SIS cross section measurement to constraint and improve the simulation of events in this region.

MINERνA is the only experiment that has concentrated on this kinematic region and this work is the first measurement of the neutrino cross section in the SIS region.

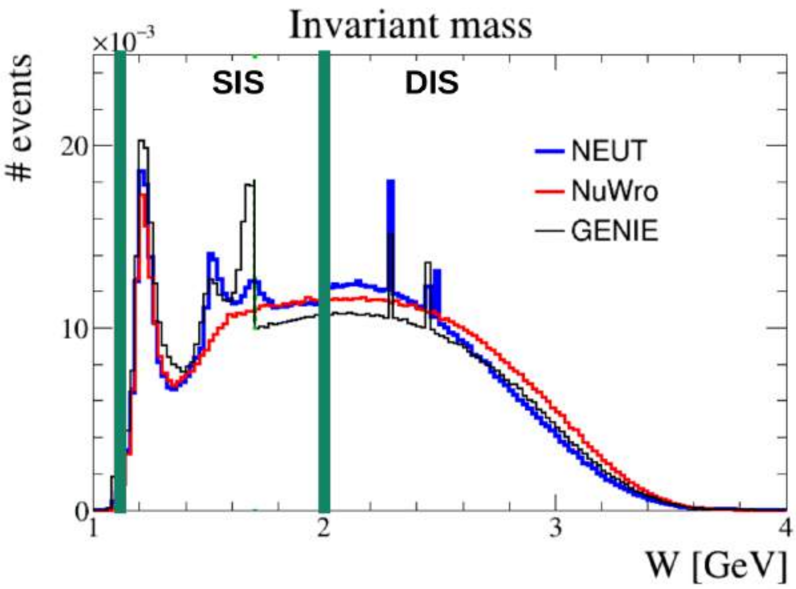

Figure 3.3: Prediction from three different neutrino generators for 6 GeVneutrino in Fe. Figure was extracted and adapated from [68]. NEUT was developped initially for the Kamiokande experiment and later was used for Super-Kamiokande [33], SciBooNE [69] and T2K [51] experiments. GENIE was developped by an international collaboration and aims to be a universal neutrino event generator. NuWro is a generator more theory oriented developed by the Wroclaw University.

Chapter 4

MINERνA Experiment

MINERνA is a dedicated neutrino scattering experiment whose main goal is to understand the nature of neutrino-nucleus interactions. To this end, it identifies the nuclear effects and test models, measures exclusive and inclusive final states and the correlations of those with leptons. In addition, MINERνA also aims to characterize neutrino interactions for oscillation experiments. The MINERνA detector sits on axis the neutrino beam produced at Fermilab, just upstream to the MINOS detector that is used as muon spectrometer of the interactions produced in MINERνA .

4.1 The NuMI Beamline

The Neutrinos at Main Injector facility (NuMI) constructed at Fermilab provides a high intensity on-axis ν_μ or $\overline{\nu}_\mu$ beam of 2-20 GeV variable energy to the MINERνA and MINOS experiments, and off-axis to the NOνA experiment. At the time of this writing the neutrino beam had an energy peak of 6 GeV. The neutrino beam results from the decays of pions and kaons produced by collisions of 120 GeV protons in a graphite target. Two magnetic "horns" focus the positive (negative) mesons that produce a ν_μ ($\overline{\nu}_\mu$) beam [70],[71] upon decaying.

Fermilab uses a series of accelerators to create the energetic protons required to produce the neutrino beam. The creation process begins with the acceleration of hydrogen negative ions in a Linear Accelerator (LINAC) to about 400 MeV. The accelerated hydrogen ions are then send to the Booster where a carbon foil removes electrons from the ions to obtain just protons which are then accelerated to 8 GeV. Then, the protons are sent to the Main Injector where they are accelerated to 120 GeV. At every 1.9 s a 8.4 μs spill with 3.5×10^{13} protons are extracted and sent towards the 0.95 m long segmented water cooled graphite target (figure 4.1), called the NuMI target [72]. Protons are extracted with a 58 $mrad$ (3.323 °) angle towards Sudan [73].

Two horns operate by a pulsed +(-) 185 kA current[1] steer pions and kaons towards the proton beam path, as can be seen in figure 4.1. The relative placement of the two horns and the NuMI target optimizes the momentum spectra of the focused particles resulting in different neutrino energy spectra [73]. The target is assembled on a system of rails that make posible moving the target along the beamline. Figure 4.2 shows the different spectra of neutrino energies produced by different configurations. The intensity of the beam is expressed in terms of the number of protons that collide the graphite target (POT). The intensity of the beam delivered in the medium energy mode used in this analysis is shown in figure 4.3.

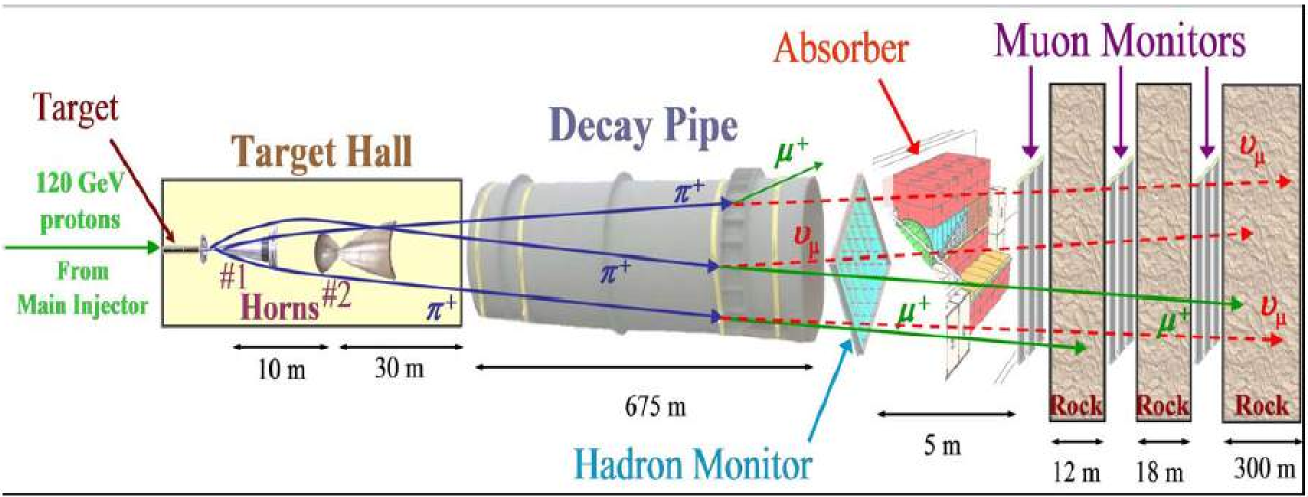

Figure 4.1: Schematic view of the NuMI beamline.

The constituent parts of the NuMI beamline are shown schematically in figure 4.1. The pions and kaons are left to decay in a 657 m long and 2 m base steel pipe kept at a constant vacuum of 1 $Torr$ [73]. The hadron absorber removes all the remaining hadrons coming out the decay volume. The secondary and tertiary particle beams are monitored by an hadron monitor and three muon monitors located next to the absorber. The dolomite rock between the monitors remove most of muons leaving neutrinos in the beam. The resulting neutrino beam consists of 97,8 % ν_μ and few $\bar{\nu}_\mu$ (1.8 %) and ν_e (0.4 %)[2]. The resulting NuMI neutrino beam is delivered to the MINERνA detector that is located 100 m underground, just upstream of the MINOS near detector [74].

[1]This current can be set to different values in order to make special studies and characterization of the beamline

[2]ν_e are the result of decay of muons.

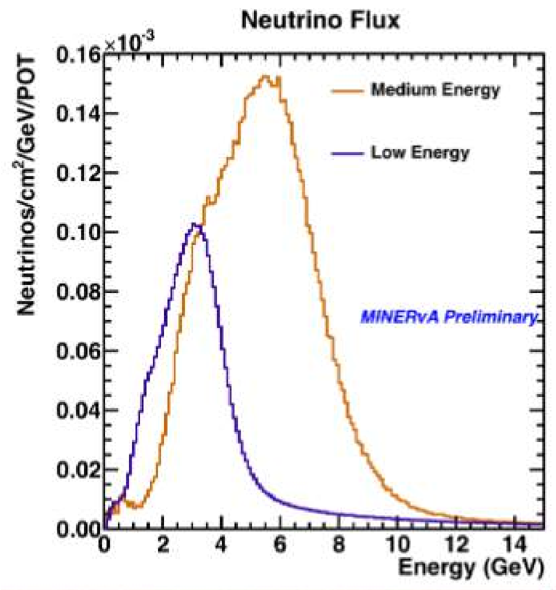

Figure 4.2: NuMI configurations. Low Energy and Medium Energy. (Flux estimation using a GEANT4 based simulation of the NuMI beam line).

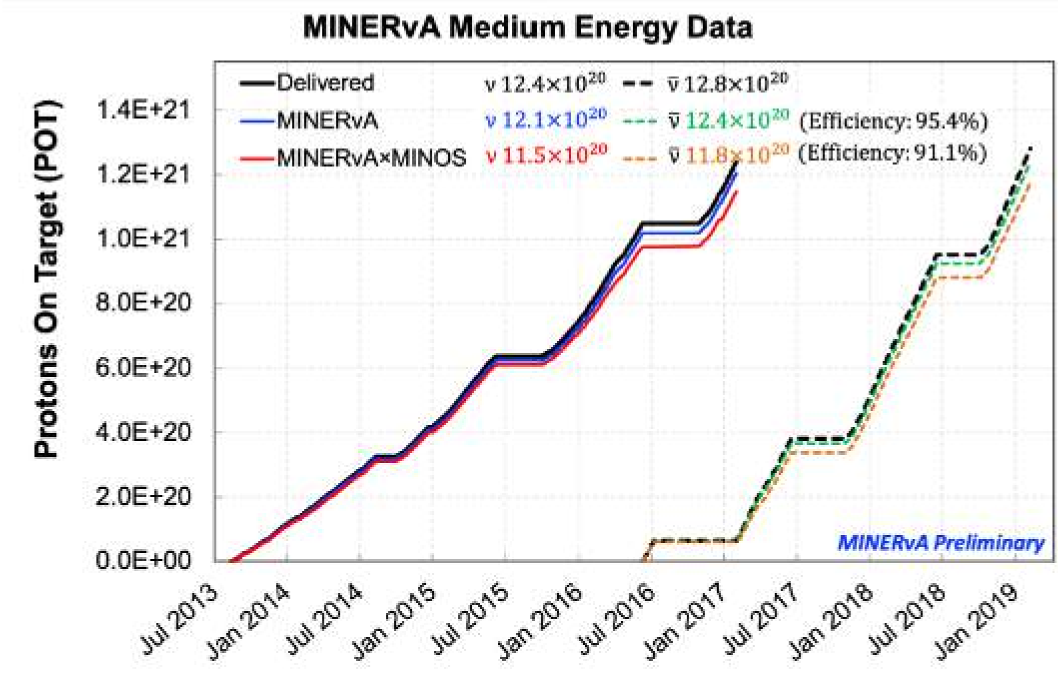

Figure 4.3: NuMI beam intensity delivered for the neutrino and antineutrino medium energy mode. The protons on target (POT) is expressed as a function of time.

4.2 The MINERνA detector

The MINERνA detector employs polystyrene scintillator to track particles and two types of calorimeters to contain showers produced by neutrino interactions. The MINERνA detector is provided of targets of a wide range of nucleon numbers to enable studies of nuclear dependence in neutrino interactions, measure form factors and measure cross-sections in this nuclei number variety to improve the systematic uncertainties in future neutrino oscillation experiments [75].

The MINERνA detector consists of a veto wall, a cryogenic liquid helium target regulated to within 25 mK and a 5 m length hexagonal prism with 4.10 m diagonal length called MINERνA main detector, as is shown schematically in figure 4.4. Figure 4.5 shows a top view of the detector.

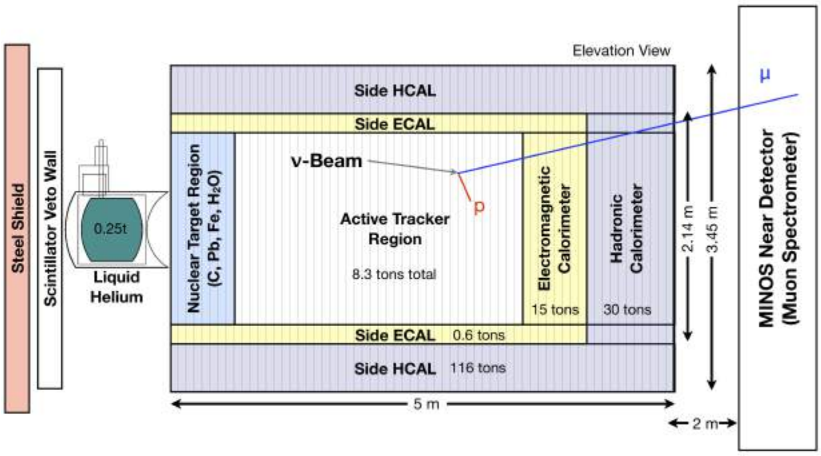

Figure 4.4: Schematic view of the MINERνA detector.

The MINERνA main detector can be thought of as two detectors: a smaller central hexagonal prism with same length but aproximately 2 m width called the Inner Detector (ID), and the surrounding volume called the Outer Detector (OD). The Inner Detector consists of: nuclear layers interleaved with scintillator planes; a region of pure scintillator planes called Active Tracker Region; the side electromagnetic calorimeter; and at the most downstream part the remaining of the electromagnetic calorimeter and part of the hadronic calorimeter. The Outer Detector consists of the side hadronic calorimeter.

The active tracker region is composed exclusively of scintillating material and is the core of the MINERνA detector.For construction convenience and handling, the MINERνA detector is made of four types of modules: tracking, nuclear target, ECAL and HCAL modules. A tracking module consists of two scintillator planes and the respective Outer Detector part, which serves as a supporting structure and is made up of a frame of steel with embedded scintillators. The side electromagnetic calorimeter of the active tracker region is incorporated as a 0.2 cm thick by 15 cm wide lead "collar" between each scintillator plane as shown in figure 4.6. The

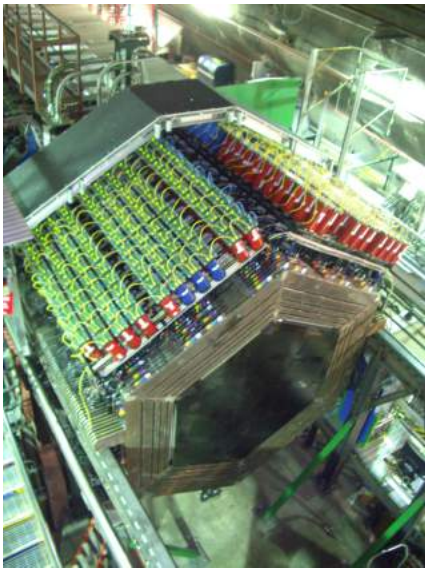

Figure 4.5: Top view of the MINERνA detector.

active tracker region consists of 62 tracking modules and each scintillator plane consists of 127 scintillating strips. A scintillator plane can have one of three different orientations. The X-plane has the scintillating strips vertically positioned in order to get the x coordenate of the hit. The U- and V-planes are rotated 60 degrees clockwise and counter-wise from the X-plane respectively. Each tracking module has a X-plane and either a U- or V-plane, as shown in figure 4.7 for just two consecutive modules. In the most upstream of the detector a "veto wall" made of thick steel plates and scintillator planes shields the detector from low energy hadrons and tags the muons produced by neutrino interactions in the rock called "rock muons". The cryogenic helium target is located between the veto wall and the main detector. The nuclear target region consists of five layers of passive targets separated by eight scintillator planes to make possible the reconstruction of the neutrino interaction vertex in the targets, and finally the downstream electromagnetic and hadronic calorimeters are made up of scintillator planes interleaved respectively with lead planes and steel planes [76].

4.2.1 The Scintillating Strips

The scintillating strips are triangular prisms of solid scintillator (Dow Styron 663 W) doped with 2,5-diphenyloxazole (POP) (1 % per weight) and 1,4-bis (5-phenyloxazol-2-yl) benzene (POPOP) (0.03 % per weight) coated by a reflective layer of TiO_2 and traversed through the center with a green wavelength shifting (WLS) fiber (1.2 diameter, 175 ppm Y-11 doped) produced by the Kuraray corporation. The transversal lengths of the scintillating strips are shown in figure 4.8.

The scintillating strips are assembled making up a plane as is shown in figure 4.9. This

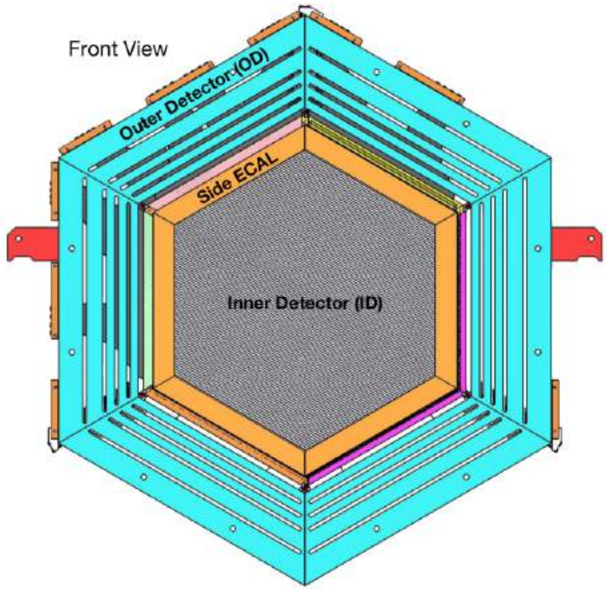

Figure 4.6: Transversal view of a MINERνA tracking module.

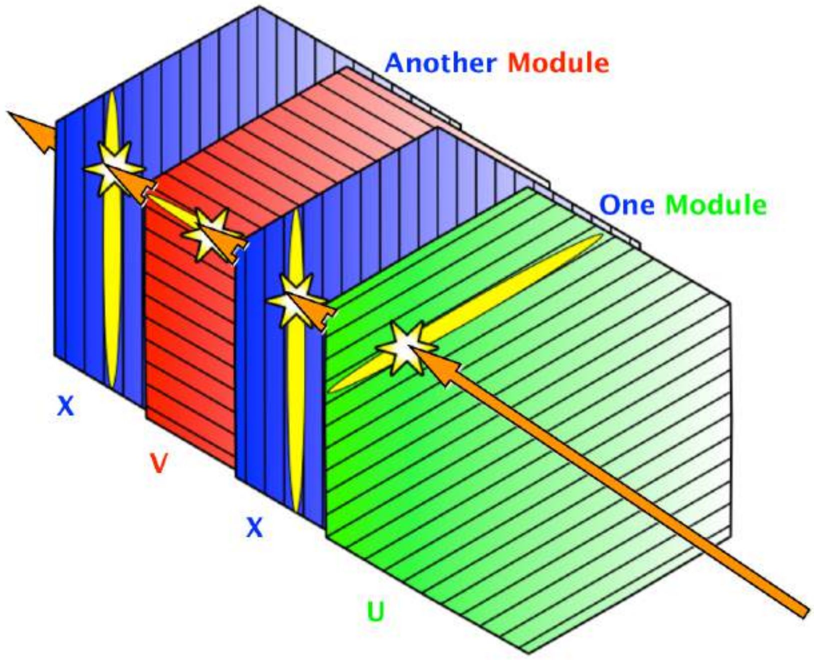

Figure 4.7: Scintillating strip orientations for consecutive modules in the MINERνA tracking region.

configuration provides charge split between neighbor strips and improves the determination of the interaction coordinate. The combination of the three posible plane orientations provides a stereoscopic 3D image of hits (interactions) in the MINERνA detector.

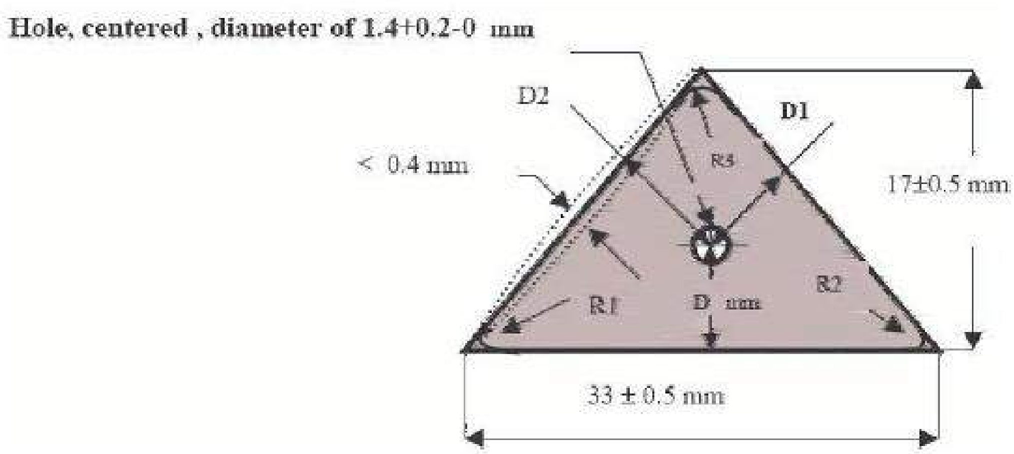

Figure 4.8: Transversal cut of the triangular scintillating prism.

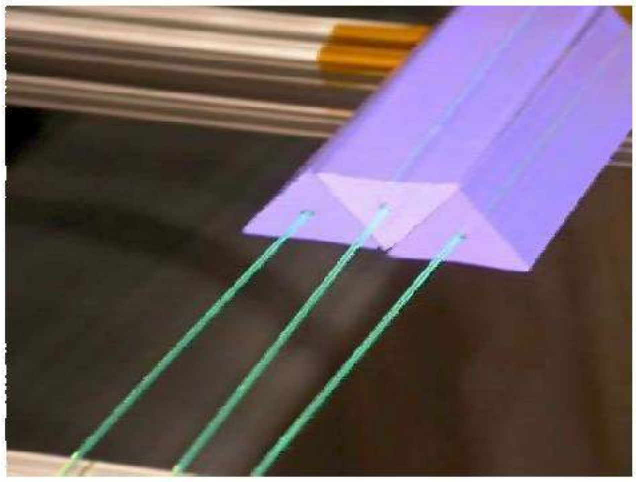

Figure 4.9: Scintillating prisms arranged to form a plane. Each prism holds an optical fiber along its full length to conduct the signal of the interaction.

4.2.2 Photodevices

The MINERνA detector uses 507 Hamamatsu Photonics H8804MOD-2 multi-anode Photomultipliers (PMTs) to amplify the scintillation light collected from the WLS (Wavelength Shifting) fibers in each scintillator strip. The PMTs are required to have a minimum quantum efficiency of 12% at 520 nm and a maximum-to-minimum gain ratio less than three. A base circuit board and the PMT are installed inside a 2.36 mm thick steel cylindrical box, keeping them protected from dust, ambient ligth and magnetic fields produced by MINOS near detector's magnetic coils. Each multi-anode PMT has an 8x8 array of pixels, each pixel having an effective size of 4 mm^2. Each PMT is collects 64 fibers in individual channels carryning the electrical signals from the WLS fibers of the strips as is shown in figure 4.10. These fast analog signals are fed to the Front End Boards (FEBs) attached to the optical box and located outside of it. The main functions of the FEB are to digitize timing and pulse-height signals, and communication to the VME readout controllers modules.

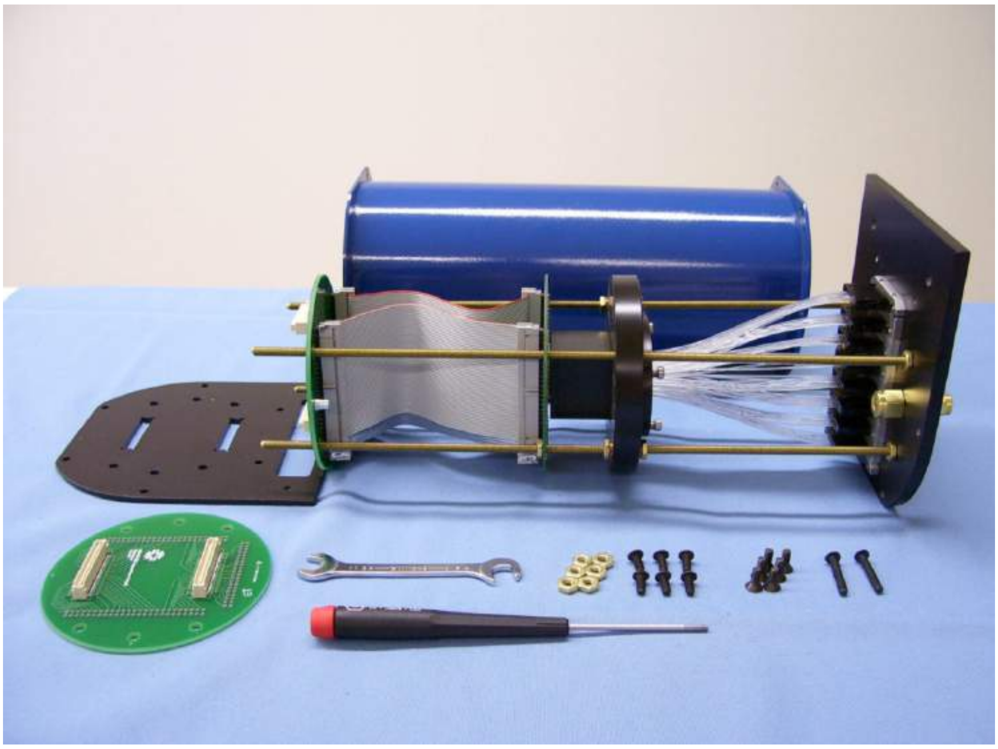

Figure 4.10: Optical box containing the Photomultiplier (small black cube) conected to the 64 clear fibers.

4.2.3 Nuclear Targets and Cryogenic Helium target

The nuclear target region located at the most upstream part of the detector is made up of five layers of passive nuclear targets in total made of Fe (998 kg), Pb (1023 kg), C (120 kg) and water. Except for the fourth and fifth layers each target is separated by four tracking modules. The figure 4.11 shows the cryogenic Helium target and the nuclear targets in the ID. There are targets made of a single material and others made of two or three materials.

The purpose of the different orientations for the materials in the mixed targets is minimization of the effect of acceptance differences for different regions in the detector. The nuclear targets are mounted in the same hexagonal steel frame (Outer Detector) as the scintillator planes. The water target do not use the OD to be mounted as is shown in figure 4.12.

The cryogenic helium target is an aluminum cryostat capable of holding approximately 2,300 L of cryogen. It consists of an inner cylinder with 152 cm inner diameter, 100 cm length, 0.635

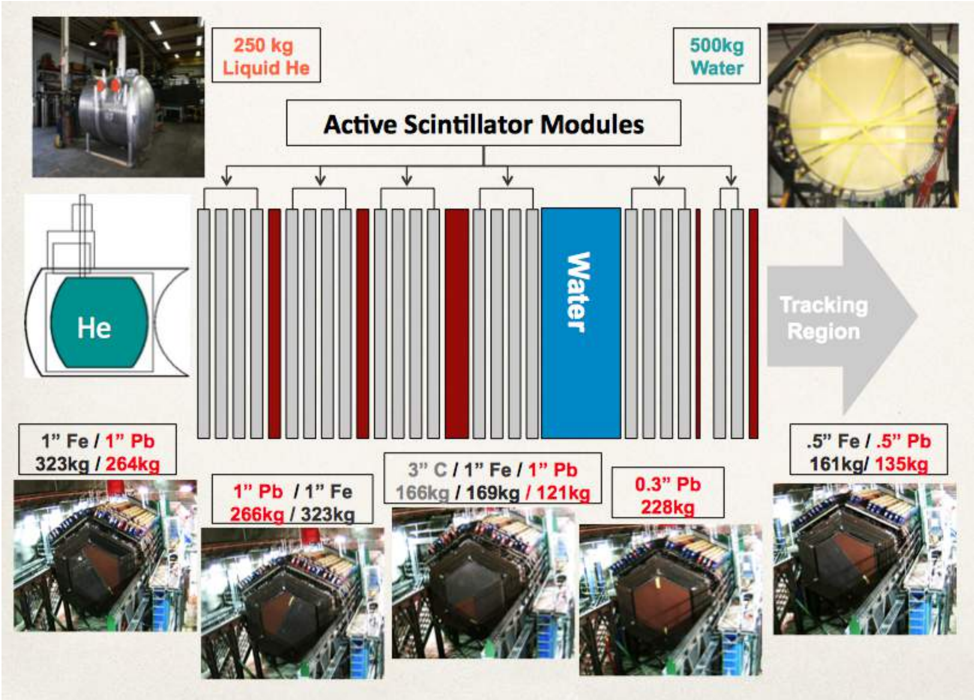

Figure 4.11: Nuclear targets.

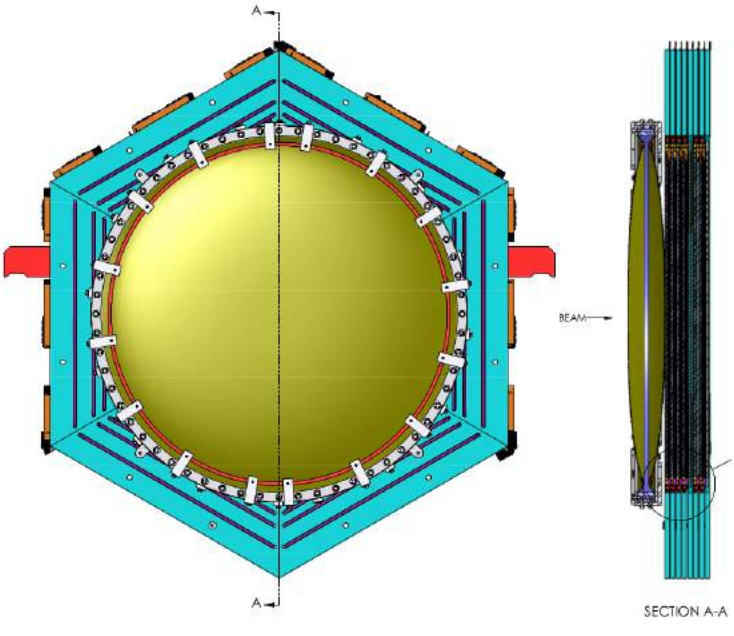

Figure 4.12: Water target

cm wall thickness; and an external vessel cylinder of 183 cm diameter and 0.952 cm wall thick.

4.2.4 Electromagnetic and Hadronic calorimeters

The electromagnetic calorimeter (ECAL) is made up of ten electromagnetic modules. This region consists of 20 layers of Pb (2 mm thick each) interleaved with scintillator planes having orientations as shown in figure 4.13.

The electromagnetic calorimeter is used to decrease the shower lengths produced by charged particles in the detector. Since pair production cross section is proportional to Z^2, photons of few GeV will be detected via pair production.

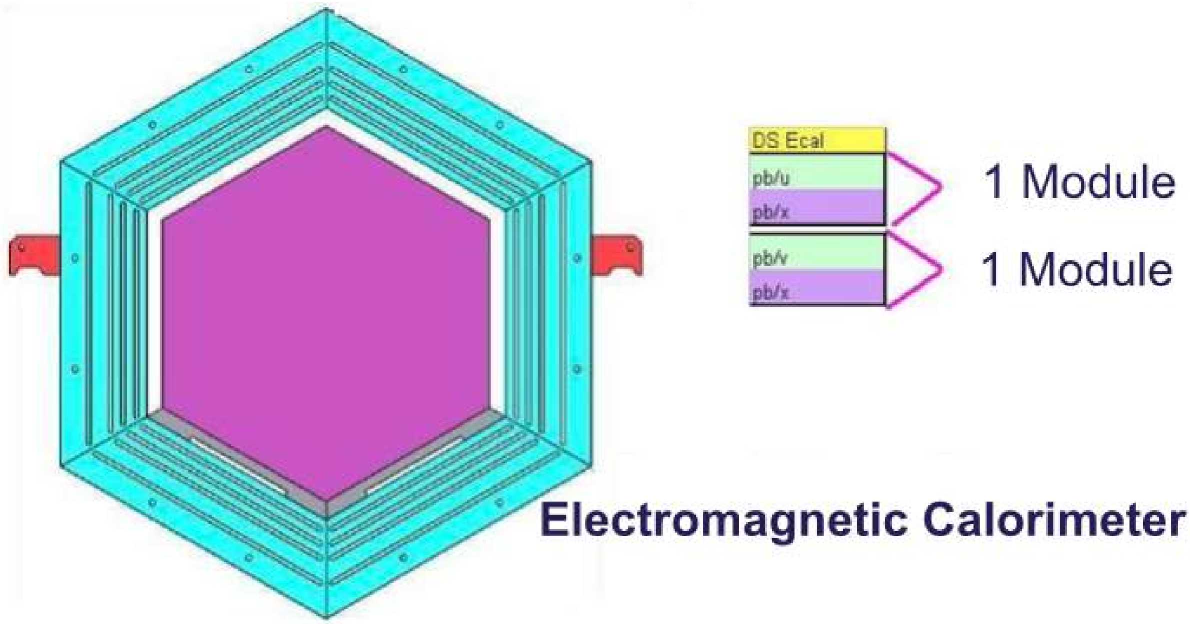

Figure 4.13: ECAL module and the orientation for two consecutive modules.

The hadronic calorimeter placed at the most downstream of the detector is made up of 20 HCAL modules. Each HCAL module is made of a Fe layer (2.54 mm) and just one scintillating plane. Muons with energy up to 600 MeV and protons with energy up to 800 MeV will be stopped by the combined action of all this layers. A HCAL module is shown in figure 4.14.

4.2.5 The Outer Detector (OD)

The Outer detector (OD) is a steel hexagonal shell with inner apothem 1.168 m and outer apothem 1.727 m. All steel frames are 3.49 cm thick except for frames surrounding the thicker downstream HCAL where they are 3.81 cm thick. Each frame has four slots each holding a pair of 2.54 × 2.54 cm^2 rectangular scintillator strips for calorimetry and tracking. The total iron thickness is 43.4 cm, or 340 g/cm^2, which can stop, from ionization losses alone, up to 750 MeV protons at 90° and nearly 1 GeV protons entering at an angle of 30°.

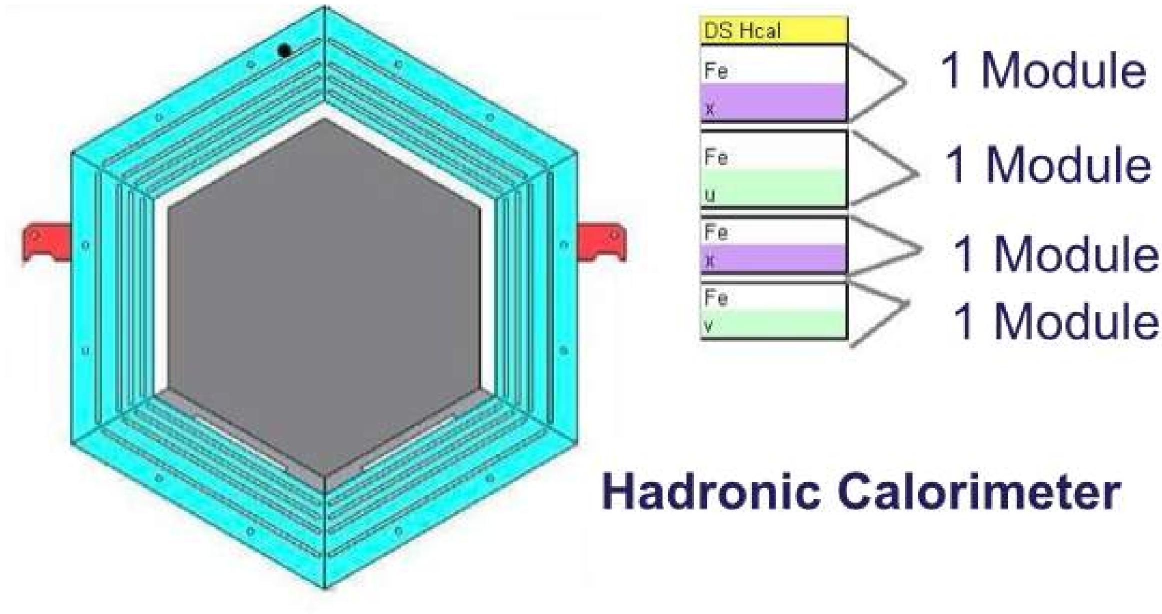

Figure 4.14: HCAL module and plane orientations for consecutive modules.

4.2.6 MINOS (Main Injector Neutrino Oscillation Search) Near Detector

MINOS is a long-baseline oscillation experiment. As an usual long-baseline type experiment it consists of two detectors separated by a long distance. The Near detector is located at Fermilab just downstream MINERνA and the Far detector is located 450 miles away in northern Minnesota. The MINOS Near and Far detectors are made of steel and plastic scintillator like the MINERνA hadronic calorimeter [74]. One of the advantages of MINOS near detector is that it is magnetized, which makes it possible the reconstruction of the charge and momentum of the (anti)muons produced by charged current (anti)neutrino interactions. The magnetic field is produced by an electric current flowing through a coil on the axis of the MINOS near detector. The figure 4.16 shows two views of the MINOS near detector (ND) which is used to measure the muons produced in charged current interactions in the MINERνA detector as shown in figure 4.15.

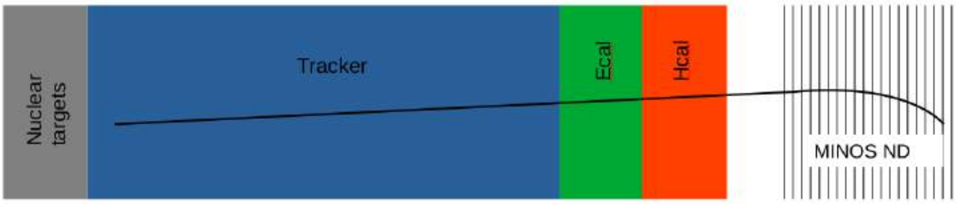

Figure 4.15: The muon produced in the charged current interaction goes through MINERνA and reachs the MINOS detector where its momentum is measured.

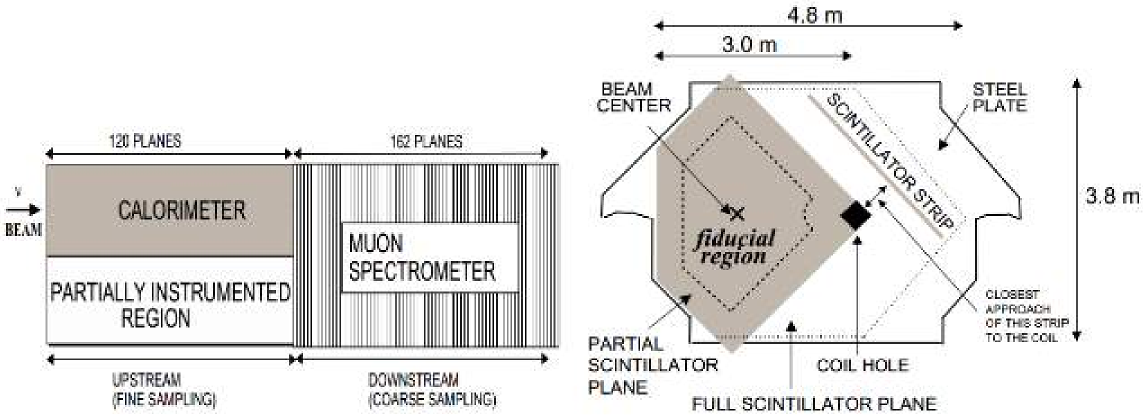

Figure 4.16: Two views of the MINOS near detector. Left: View from above. Right:View in the beam direction.[76].

Chapter 5

Reconstruction

The goal of the reconstruction is to transform information the detector records, such as electronic signals, location and time of the hits, into physical quantities. This general reconstruction is run on all of MINERνA 's data and simulation, which allows us to classify and quantify event interactions. Basically, the reconstruction have three stages: grouping hits by time (time slicing), grouping hits by location (cluster formation), tracking, and matching tracks into the MINOS detector.

5.1 Time Slicing

Each readout gate is opened for 16 μs which is enough time to detect multiple neutrino interactions. The pile-up of interactions is initially mitigated by grouping the hits without considering any location information. This first step of the reconstruction is called Time-slicing. A time slice is created each time the hits sum in total 10 photoelectrons or more within a 80 ns time window. Hits in the readout gate that occur no later than 50 ns after the last hit and not earlier than 30 ns before the first hit are also added. The time slices of a sample time profile of a MINERνA 's readout gate are shown in figure 5.1.

5.2 Cluster Formation

The special arrangement of the scintillator strips (Figure 4.9) allows charged particles traveling through the detector deposit energy at least in two strips.A group of hits (or even a single hit) can be considered a cluster. Clusters are divided into different types depending on their size and total energy deposit.

- Low activity clusters: Total energy deposit is less than 1 MeV.

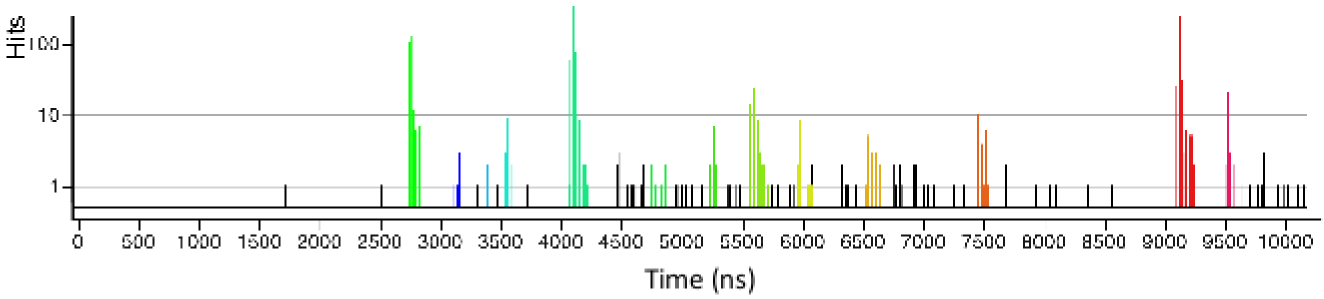

Figure 5.1: Time slices (denoted by different colors) in a typical readout gate (a 8.4μs spill of the NuMI beam) [76]

- Trackable clusters: The energy deposited in each bin is between 1 and 8 MeV and the clusters consist of at least 4 hits and have a total energy between 1 and 12 MeV.
- Heavy ionizing clusters: Total energy deposited by the hits must be greater than 1 MeV and one to three adjacent hits must have energy greater than 0.5 MeV. This type of cluster is essential in forming high angle tracks.
- Superclusters: Any group of more than 4 hits is classified as a supercluster. These clusters are consistent with an hadronic or electromagnetic shower.
- Cross-talk clusters: Low energy hits that usually induced by the optical cross talk in a PMT.

5.3 Tracking

Clusters are used to create a reconstructed object called "track" which approximates a charged particle's trajectory through the detector. Tracking consists in determining one anchor track which will then serve as a start point to determine the rest of tracks. Trackable and heavy ionizing clusters are used to define track seeds that are defined as a group of three clusters in one view (X,U or V) meeting two requirements:

- clusters of the seed must be on consecutive planes
- clusters of the seed must fit a straight line
- seeds do not contain clusters in the same scintillator plane

Two-dimensional trajectories for one view (X,U or V) are created stitching together track seeds by comparing their projected slopes and by ensuring they have a common cluster. These proto-track objects are called candidates. After all candidates are built, they are merged using the same criteria used for merging the seeds. The candidates from different three views are then merged into three dimensional objects if they overlap longitudinally and are mutually consistent with the same three-dimensional line. These candidates are evalulated in two views and if they overlap longitudinally a 3D track is created. In the remaining view a search for the unused clusters that have a position consistent with the candidate pair is performed, and if there are enough clusters a 3D track is created. The 3D tracks found are fitted using a custom Kalman filter routine that includes multiple scattering [77] [78].

5.4 Matching tracks into the MINOS Near Detector

Reconstruction information from MINERνA and MINOS detectors are used to completely reconstruct the muon energy and trajectory. The muon track produced in MINERνA is matched to a muon track in MINOS. The track in MINERνA must stop in the last five modules of the detector and the track in MINOS must begin in the first four modules, and also they must be within 200 ns of each other in time. To match the muon the start point of the MINOS track is extrapolated into MINERνA , and the end point of the MINERνA track is extrapolated into MINOS. The distance of the extrapolated MINOS track to the end point of the MINERνA track and the distance of the extrapolated MINERνA track to the start point of MINOS track are both called residuals. A MINERνA track is considered MINOS matched if both residuals are smaller than 40 cm. If none of the residuals are smaller than 40 cm the closest approach method is performed which consists in finding the point of closest approach of the two tracks via Euclidean distance minimization for the two points in the x and y plane. The MINOS matched tracks are usually muon tracks and MINOS measures the muon momentum using two different methods:

- Range method: based on the total energy lost by the muon in MINOS. It is applied only to muons contained in the calorimeter of the MINOS detectors.

- Curvature method: based on measuring the curvature of the muon track caused by the magnetic field of the MINOS detector. Equation 5.1 is used,

$$k = \frac{1}{R} = \frac{0.3B}{P}, \tag{5.1}$$

  where k is the curvature, R is the radio of the curvature, B is the magnetic field and P is the momentum component perpendicular to the field.

5.5 Hadronic Energy Reconstruction

In an interaction event the neutrino energy is transferred to the muon and to the nucleus resulting in a number of final particles. By energy conservation the neutrino energy must equal the sum of the muon energy(E_μ) and the hadronic energy (E_{had}),

$$E_\nu = E_\mu + E_{had}. \tag{5.2}$$

The estimation of the hadronic energy (also known as recoil energy) is essential for the accurate measurement of the neutrino energy since most of the energy transferred is hadronic energy.

We have to sum all the energy deposits to determine the total recoil energy (or E_{had}) of an event. Energy deposits in all the subdetectors, electromagnetic calorimeter (ECAL), hadronic calorimeter (HCAL), side electromagnetic calorimeter (sideECAL), outer hadronic calorimeter (OD) and tracker, are considered.

The HCAL, ECAL, sideECAL and OD subdetectors have passive material, lead and iron, in which particles deposit energy that is not detected. The recoil energy must be weighted to account for this lost energy. The total recoil energy[1] of an event is defined as,

$$E_{recoil,reco} = \alpha * \sum_i c_i E_i \tag{5.3}$$

$$i = \{tracker, ECAL, HCAL, SideECAL, OD\}. \tag{5.4}$$

The calorimetric constants c_i, were calculated by minimum ionizing particles with normal incidence angle traveling through prototypes of the subdetectors. The calorimeter constants calculated are 1.0 for the tracker, 2.01 for the ECAL and sideECAL and 10.31 for the HCAL and OD [79]. The calorimetric constants c_i for each sub-detector i were calculated respect to the tracker scintillator material. α is a global scale factor that compensates for the loss of visible energy due to final state interactions, neutral particles, binding energy of struck nucleon and energy leakage. The global scale factor is calculated by varying α via Minuit [80] to match the recoil energy to the true recoil energy (recoil energy generated by GENIE) by minimizing the error,

$$error = \sum \frac{[arctan(E_{recoil,reco}/E_{recoil,true}) - \pi/4]^2}{N} \tag{5.5}$$

where N is the number of events in the inclusive sample.

The final step is a per-bin correction using the reconstructed and true recoil energy corrected by the global scale factor α. The final correction basically consist on mapping $\eta = \Delta E/E_{true}$

[1]subscript reco and true are used to distinguish the reconstructed and the true value of any quantity. The true value is obtained from the Monte Carlo and the reconstructed value is the one we obtain from the event reconstruction.

with $\Delta E = E_{reco} - E_{true}$ to the mean $< E_{true} >$ in each true bin (Appendix B). After all the corrections are made, the standard deviation (σ) of the gaussian fit of the $\Delta E/E_{true}$ distributions in each bin is plotted in figure 5.2.

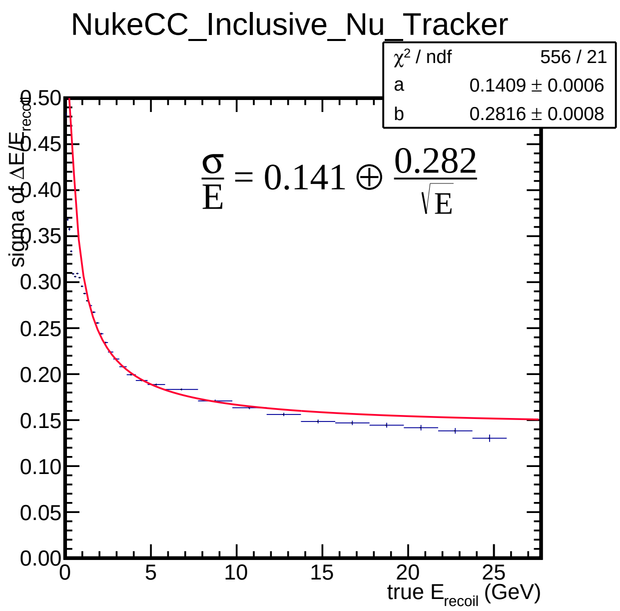

Figure 5.2: Calorimetric hadronic energy resolution for Charged Current inclusive events in the tracker region of the MINERνA detector

The fit, aldo shown in equation 5.6, represents the hadronic energy resolution of the tracker region where the $\oplus$ symbol indicates a quadratic sum. The first term on the right-hand side of the equation is called the 'constant term' and it is due to contributions which do not depend on the energy of the particle such as instrumental effects, detector geometry and temperature gradients. The second term of the equation is called the 'stochastic term' which it is due to fluctuations related to the physical development of the shower. In general the hadronic resolution improves as the hadronic energy increases.

$$\frac{\sigma}{E} = 0.141 \oplus \frac{0.282}{\sqrt{E}}, \tag{5.6}$$

5.6 Event Selection

The calculation of a differential cross section requires the selection of SIS events. The differential cross section is defined as follows,

$$\frac{d\sigma_i}{dx} = \frac{U_{ij}(d_j - b_j)}{\Delta x_i \epsilon_i \Phi N}, \tag{5.7}$$

where the indices j and i refer to a reconstructed and true bin respectively. The Δx_i is the bin width, ϵ_i is the event selection efficiency, Φ is the integrated neutrino flux, N is the number of nucleons in the tracker region, d_j is the SIS events selected, b_j is the SIS background and U_{ij} is an unfolding matrix which map events from reconstructed bins to true bins. The SIS event selection d_j is done by applying some requirements:

- Charged Current events are considered for this analysis therefore only muons that matched into the MINOS near detector are analyzed.
- To select negative muons the curvature k of the muon traveling through the MINOS detector must be negative (equation 5.1).
- The vertex of the events must be inside a fiducial volume in the tracker region: a transveral hexagon with 85 cm apothem and vertex z component between modules number 27 and 80. This volume ensures events not occuring in the electromagnetic calorimetry that surrounds the tracker region and also events not occuring in the passive targets upstream the tracker region.
- The reduction of rock muons mis-reconstructed in the fiducial volume is done by applying a cut on the maximum allowed deadtime upstream of the vertex [76].
- The muon energy is restricted to $2 < E_\mu < 50$ GeV and the muon angle is restricted to $\theta < 20°$. A 2 GeV muon energy will be able to travel all along the MINERνA detector and travel 100 mm in the MINOS fiducial region. The higher boundary of 50 GeV muon energy ensures high DIS events statistics which is one sideband of the SIS region. The $\theta < 20°$ cut is set based on MINOS muon acceptance.
- The maximum energy of the accelerated proton colliding the graphite target is 120 GeV. Therefore the neutrino energy is restricted to $E_\nu < 120$ GeV.
- The curvature of the muons reconstructed in MINOS must have at least 5σ significance [53] .
- The endpoints of the muon tracks must be at distance R from the MINOS coil, such that $210 < R < 2500\ mm$ [53] .
- The SIS events are selected by applying the kinematic cut $1.5 < W < 2.0\ GeV$ as was defined in section 3.2.

In the Monte Carlo simulation the number of events remaining after each selection cuts where studied and the results are shown in table 5.1.

	RECONSTRUCTION CUTS	Events	Survival rate (%)
NO CUT	Generated SIS events	146213	100
CUT1	Events in Material	83885	57
CUT2	CUT1 and Fiducial	76489	52
CUT3	CUT2 and Angle $\theta_\mu < 20$ degrees	75173	51
CUT4	CUT3 and Curvature Cuts < -5.0	69352	47
CUT5	CUT3 and Coil Cuts r < 2500mm r >210mm	67177	46
CUT6	CUT4 and CUT5 and Helicity	63593	43
CUT7	CUT6 and Good Tracking cuts	59261	41
CUT8	CUT7 and Dead Time cut	56705	39
CUT9	CUT8 and $E_\nu < 120$ GeV	56704	39
CUT10	CUT9 and $\theta < 20$ & $2 < E_\mu < 20\ GeV$	55893	38
CUT11	CUT10 and SIS cut	35021	24

Table 5.1: Survival rate of the number of events for the selection cuts.

Chapter 6

SIS Background

The SIS background are events reconstructed as SIS events that are not truly SIS events. These events have reconstructed hadronic invariant mass $1.5 < W_{reco} < 2.0$ GeV but true hadronic invariant mass $W_{true} < 1.5$ GeV or $W_{true} > 2.0$ GeV. It will be referred just as background in the rest of the text unless specified otherwise. The background has to be subtracted from SIS data because it is a source of contamination and it is represented by b_j in the numerator of the cross Section formula 5.7. The background is estimated from Monte Carlo simulation and in consequence it brings model dependency to the cross section measurement. In order to minimize this dependency the Monte Carlo prediction is constrained to the Data in the neighbors regions of the SIS region and later these constraints are used to tune the background in the SIS region.

6.1 Templates

The templates are regions in the W_{true} space that represent not true SIS events, that is, events with $W_{true} < 1.5$ or $W_{true} > 2.0$. The templates are used to estimate the background in the SIS region ($1.5 < W_{reco} < 2.0\ GeV$) coming from three regions mostly populated by quasi-elastic events, resonant meson production and DIS events. Therefore, the templates are the Quasi-Elastic template, Resonance template and DIS template as shown in Figure 6.1

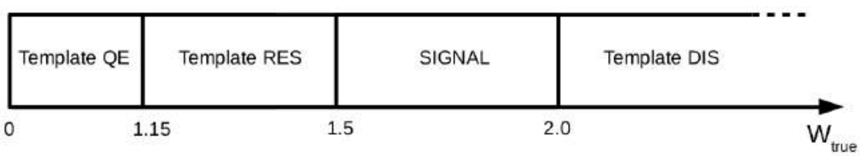

Figure 6.1: Template boundaries

6.2 Sidebands

Sidebands are regions in the W_{reco} space that represent well the SIS background events. In the sidebands the Monte Carlo prediction is constrained to the data and a scale factor is extracted for each sideband. The sidebands must represent well the SIS background and therefore gaps between the sidebands and the SIS region are constructed to minimize the inclusion of events misreconstructed as background or events misreconstructed as SIS events as shown in Figure 6.4. The sidebands boundaries were calculated by evaluating the signal contamination and efficiency of events coming from different templates as shown in figures 6.2 and 6.3.

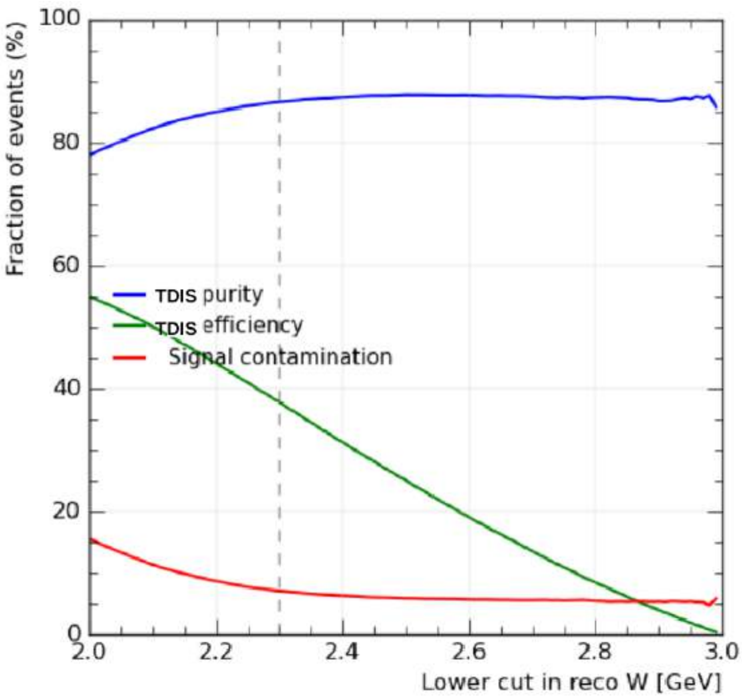

Figure 6.2: Template DIS events purity, Template DIS efficiency and Signal contamination in a DIS sideband are plotted. As the "lower cut in reco W" of the DIS sideband shifts to higher values the signal contamination decreases, the efficiency decreases linearly and the purity increases. $W_{reco} = 2.3\ GeV$ was chosen as the best value for the lower boundary of the SIS sideband and $W_{reco} = 3.0\ GeV$ was chosen as the higher DIS sideband boundary

6.2.1 SIS Sidebands Fitting prescription

In the Sidebands the Monte Carlo prediction is fitted to the Data by using a χ^2 minimization per bin method as per equation 6.1,

$$\chi^2 = \sum_{bini}^{n} \frac{(N^i_{data} - N^i_{MC})^2}{N^i_{data}} \tag{6.1}$$

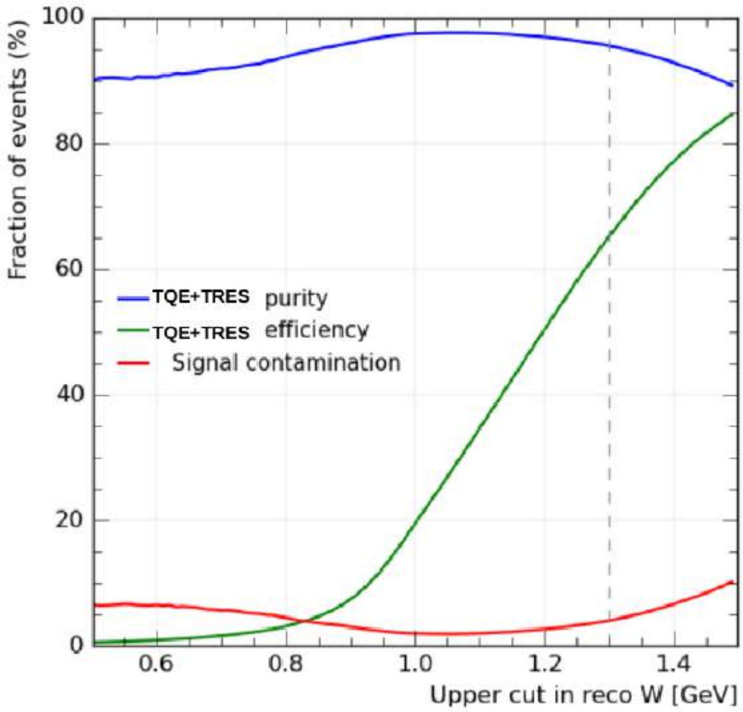

Figure 6.3: Template QE + Template RES events purity, Template QE + Template RES efficiency and Signal contamination in a QE + RES combined sidebands are plotted. As the "higher cut in reco W" of the QE + RES combined sidebands shifts to higher values the signal contamination increase slowly, the efficiency increases almost linearly and the purity decreases slowly. $W_{reco} = 1.3\ GeV$ was chosen as the best value for the higher boundary of the combindes QE+RES sidebands.

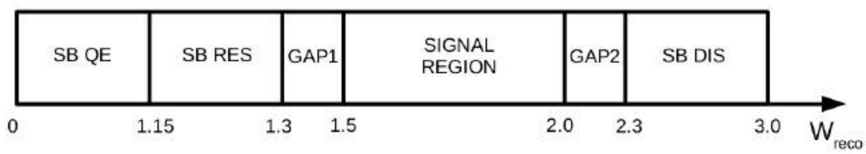

Figure 6.4: Sidebands boundaries

where N^i_{data} and N^i_{MC} refer to the number of events in the bin i of the Data and Monte Carlo simulation distributions respectively. The last MINERνA's Inclusive Charged Current Cross Section measurement [81] shows that the muon momentum components are good at discriminating events of different kinematic regions. Therefore the scale factors using the transverse muon momentum p_t and the longitudinal muon momentum p_l were extracted and are shown in table 6.1. The scale factors are practically the same for each of the momentum components and the transverse muon momentum scale factor was chosen for the analysis because of a slightly better agreement when used. The unscaled (untuned) and scaled (tuned) distributions in the sidebands for p_l and p_t distributions are shown in figures 6.5, 6.6 and 6.7, and the calculated

MC background tuned and untuned in the SIS region are shown in figure 6.9. Tuning results for other kinematic variables are shown in Appendix C.

	p_l factor	Statistical error		p_t factor	Statistical error
SB QE	1.229	±0.008	SB QE	1.237	±0.007
SB RES	1.063	±0.010	SB RES	1.045	±0.010
SB DIS	1.148	±0.007	SB DIS	1.134	±0.007

Table 6.1: The scale factors extracted for longitudinal muon momentum p_l and transversal muon momentum p_t distributions in the sidebands. These scale factors were extracted using a χ^2 minimization per bin 6.1 simultaneosly in all the three sidebands.

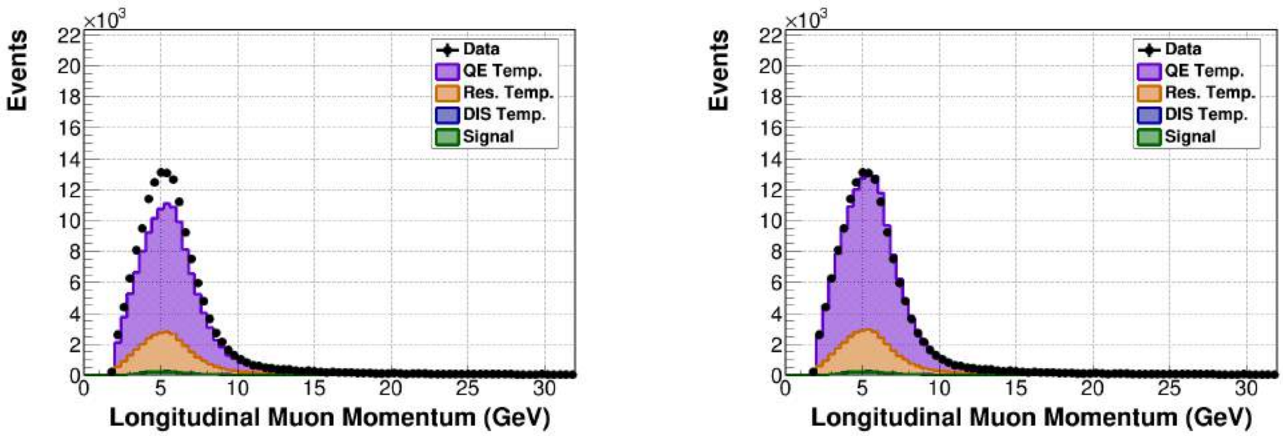

Figure 6.5: p_l distribution in Sideband QE showing the contributions from the templates. Left: Untuned. Right: Tuned with the p_l scale factors in table 6.1

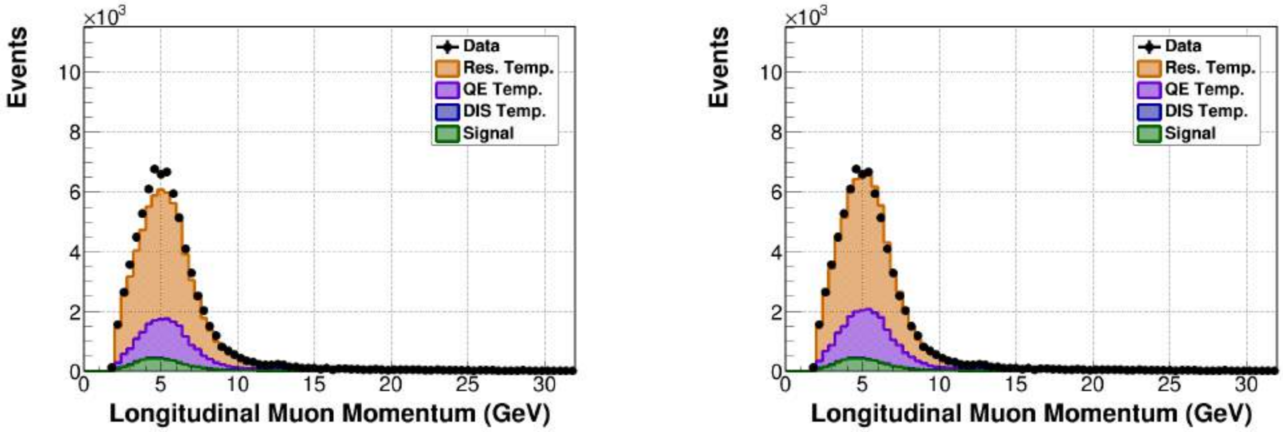

Figure 6.6: p_l distribution in Sideband RES showing the contributions from the templates. Left: Untuned. Right: Tuned with the p_l scale factors in table 6.1

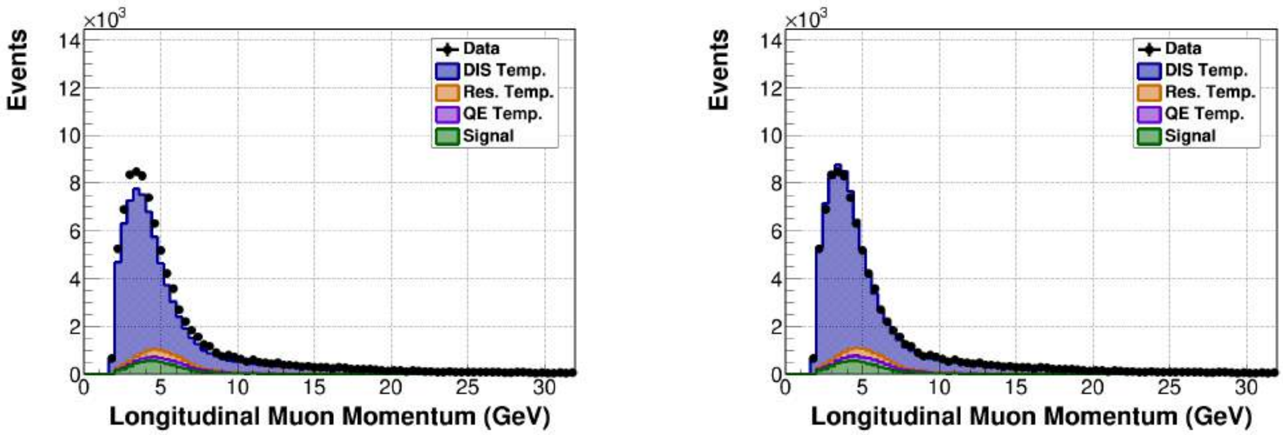

Figure 6.7: p_l distribution in Sideband DIS showing the contributions from the templates. Left: Untuned. Right: Tuned with the p_l scale factors in table 6.1

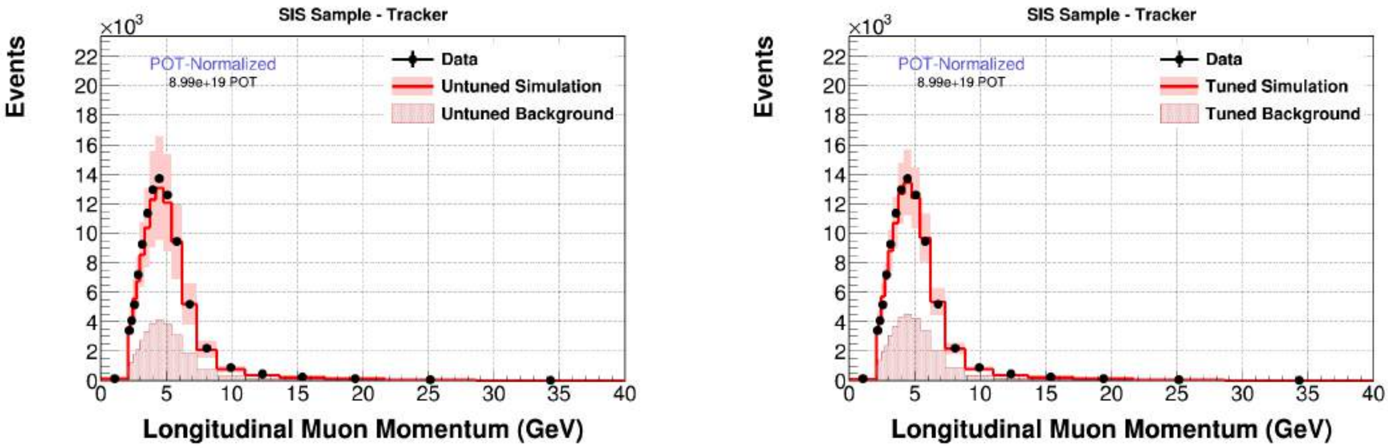

Figure 6.8: Data and MC for p_l in the SIS region. The pink area sorrounding the MC distribution represents the systematic plus statistical error. Also the MC background calculated is shown. Left: Untuned. Right: Tuned with the p_l scale factors in table 6.1

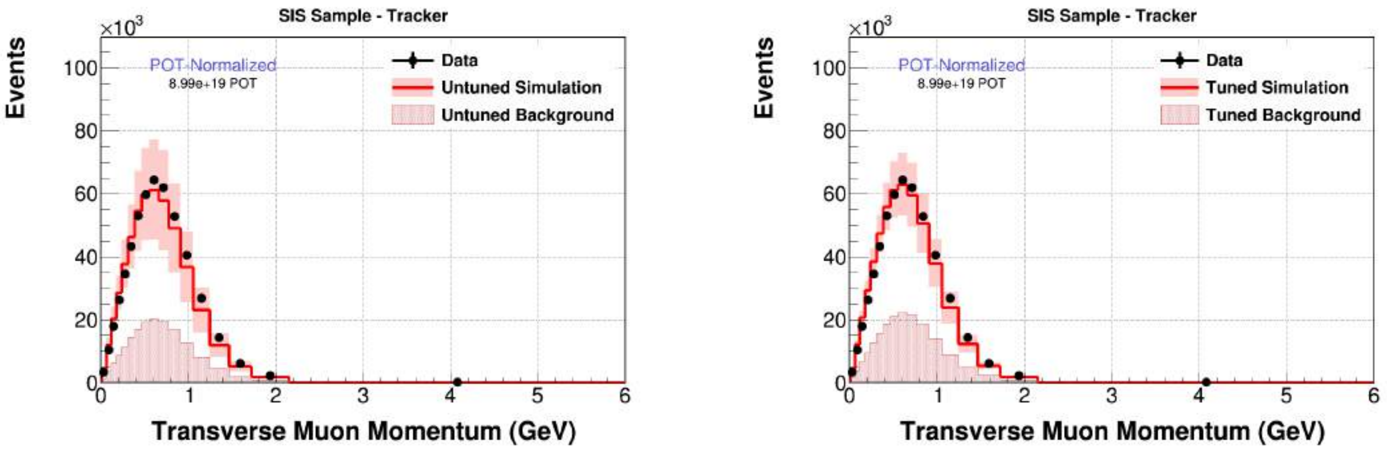

Figure 6.9: Data and MC for p_t in the SIS region. The pink area sorrounding the MC distribution represents the systematic plus statistical error. Also the MC background calculated is shown. Left: Untuned. Right: Tuned with the p_l scale factors in table 6.1

Chapter 7

Systematics

The simulation models and events reconstruction insert systematic uncertainties in the cross section measurement. These uncertainties arise from imperfect knowledge of parameters to which the cross section is sensitive. The main sources of systematic errors in MINERνA are the detector resolution, the flux, the detector mass, the interaction models and and the final state interactions (FSI) models. In this analysis the systematic uncertainties are assigned to the predicted MC and then extended to the data.

7.1 Calculation of the Systematic Uncertainties

The systematic uncertainty of a distribution of any parameter x is evaluated by the multi-universe method. This method consists of producing different distributions (universes) by shifting underlying parameters on which the x parameter depends on. These underlying parameters vary from 1 to 100 times accordingly to the 1σ variation of all these parameters. The systematic uncertainty is the average difference between each universe and the nominal value of the parameter x.

7.2 GENIE Uncertainties

The GENIE systematic uncertainties are constituted by the uncertatinty in the models used to calculate the cross section, the final state interaction model used to propagate the particles inside the nucleus and the hadronization model. The uncertainty in the cross section models are calculated using two different universes constructed from two pre-calculated GENIE weights [82] correspoding to the negative and positive σ variations in question, in this case the spread of the two universes is the uncertainty. The uncertainty in the FSI models are also calculated using re-weighting which depends on the probability of a particle for each step going through the nucleus [82]. The hadronization model introduces an uncertainty that cannot be calculated by re-weighting but from separate generations of GENIE instead, which were produced by: changing the effective radius of the interactive nucleus, altering the formation length of the hadrons and alternating tuning of the hadronization model GENIE uses [83].

7.3 Flux

There are three sources of uncertainties inherent to the flux production. The production rate of kaons and pions from the accelerated protons interacting with the graphite target are estimated using data from the CERN's NA49 experiments [84] which is extrapolated to MINERνA 's range of energy. This extrapolation inserts an uncertainty in the flux simulation. The possibility of the particles created in the target to re-interact as they travel through the long graphite target, also known as tertiary particle production, is also a source of uncertainty. The third source of uncertainty comes from the beam focusing which is done by the magnetic horns [85]. The total flux uncertainty takes into account the three sources and is extracted from 100 universes.

7.4 Absolute Normalization

The absolute normalization of the cross section inserts uncertainties coming from the detector target mass and POT counting. As the study in [86] has found, the target mass modeled actually overestimates actual mass existent in the detector. The POT counting uncertainty comes from the precision to estimate the primary protons colliding with the graphite target which is about 1% as showed in the study [83].

7.5 Matching Efficiency

The muons produced in the charged current interactions in the tracker region travel through the electromagnetic and hadronic calorimeters to reach MINOS. An uncertainty that reflects the muon deviation from straight path caused by multiple scattering in the Electromagnetic and Hadronic Calorimeter is considered [87] .

7.6 Detector Resolution

The detector resolution uncertainty is associated with the tracking and energy estimation for muon energy, muon theta angle and hadronic energy. The reconstruction of these three quantities influence directly on the derived quantities, such as W which is used to select SIS events.

The E_μ, θ_μ and E_{had} are shifted individually according to a random number from a Gaussian distribution with 1σ width of the variable in question. The detector resolution is calculated using 60 universes.

7.7 SIS background

The systematic uncertainty of the SIS background tuning was evaluated by applying the fitting procedure in the sidebands (chapter 6) to each universe of each uncertainty source. A scale factor for each universe was extracted, which later was used to tune the respective universe in the signal. Therefore the tuned universes in the signal are pinned in some way and the procedure reduce considerably the systematic uncertainty. The systematic uncertainties for the background in the sidebands for p_t and p_l are shown in figures 7.1 - 7.6. The background systematic uncertainties for other kinematic variable are shown in Appendix D.

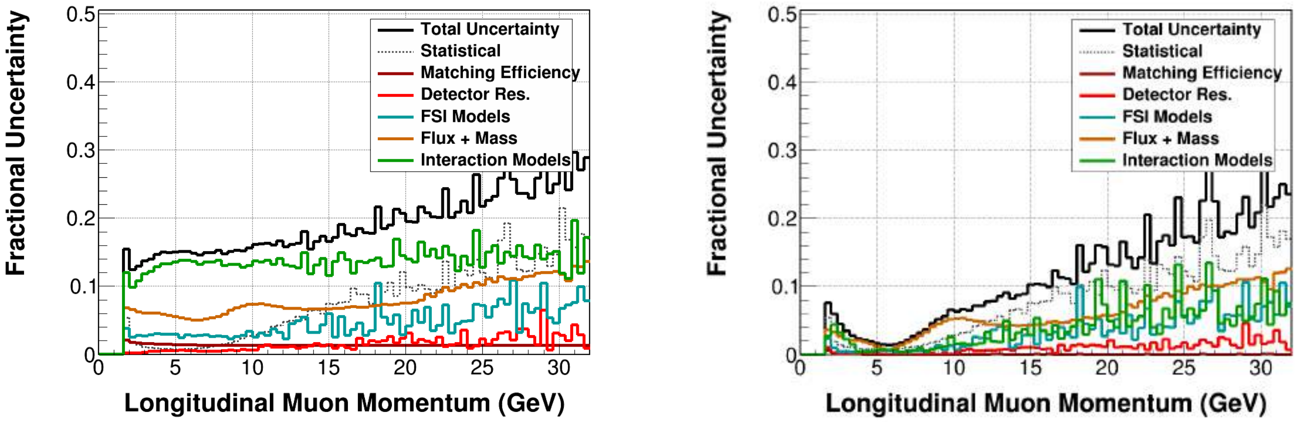

Figure 7.1: p_z distributions in Sideband QE of the statistical and systematic errors. Left: Untuned. Right: Tuned

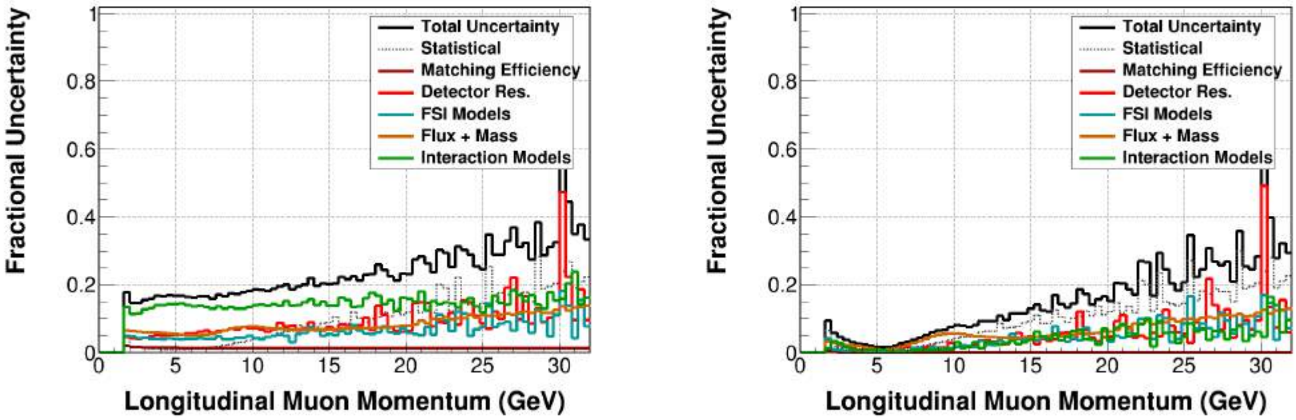

Figure 7.2: p_z distributions in Sideband RES of the statistical and systematic errors. Left: Untuned. Right: Tuned

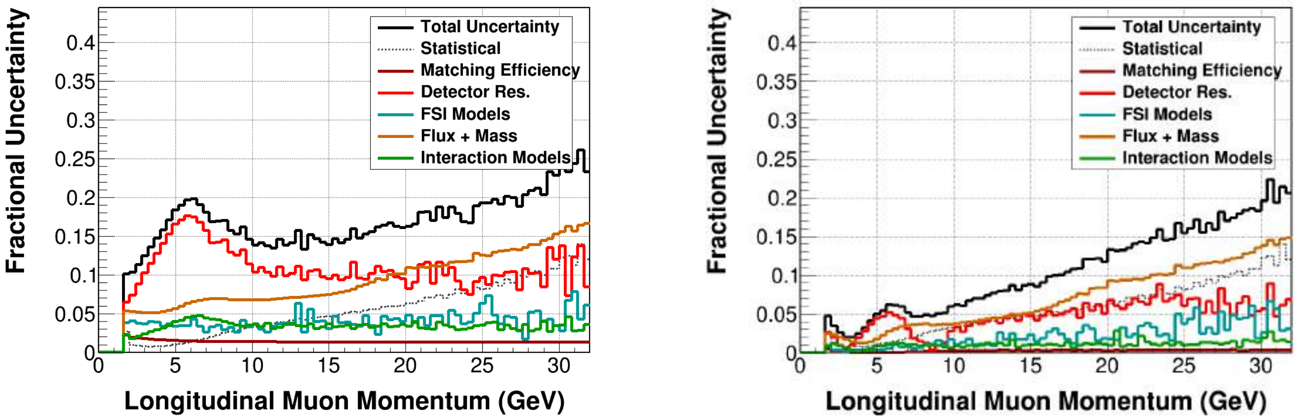

Figure 7.3: p_z distributions in Sideband DIS of the statistical and systematic errors. Left: Untuned. Right: Tuned

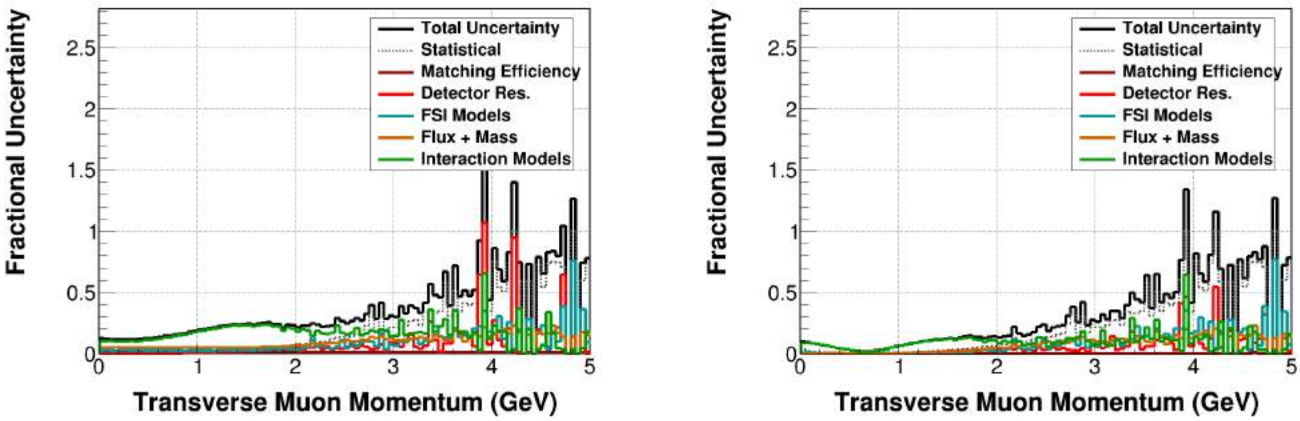

Figure 7.4: p_t distributions in Sideband QE of the statistical and systematic errors. Left: Untuned. Right: Tuned

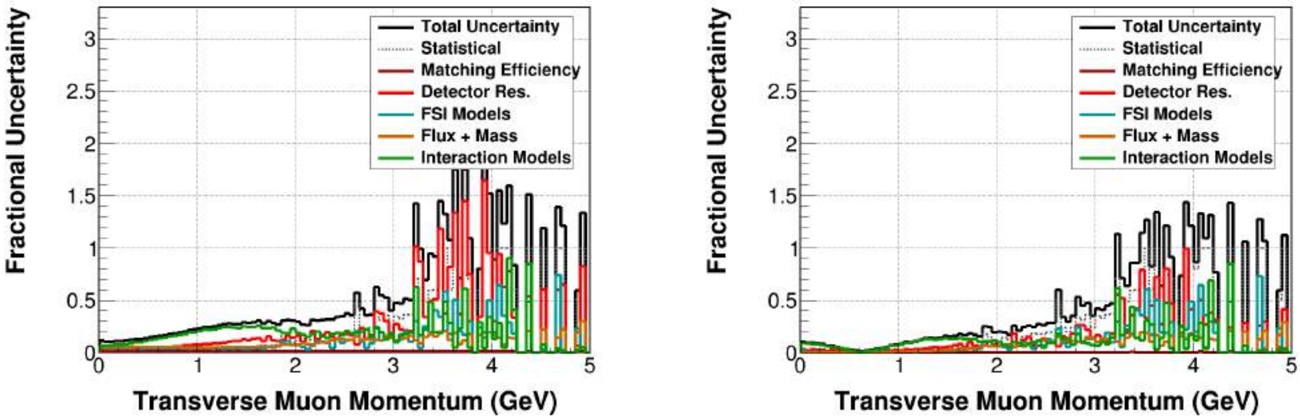

Figure 7.5: p_t distributions in Sideband RES of the statistical and systematic errors. Left: Untuned. Right: Tuned

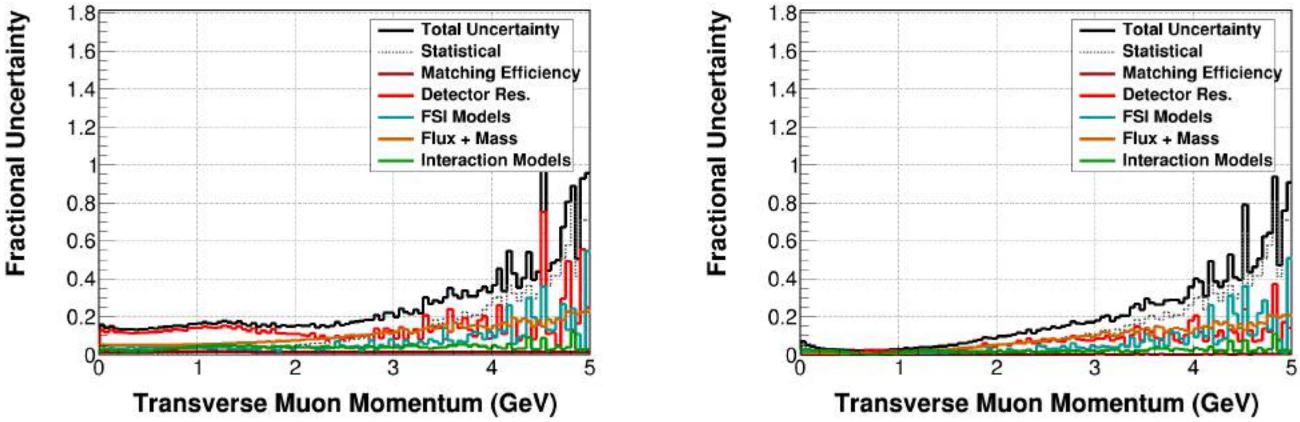

Figure 7.6: p_t distributions in Sideband DIS of the statistical and systematic errors. Left: Untuned. Right: Tuned

Chapter 8

Unfolding

The procedure of correcting for the distortions and smearing caused by the limited resolution of the detector is known as unfolding. In all experiments the act of measuring a quantity introduces deviations that the unfolding is aimed to correct. Unfolding facilitates the comparison of results between different experiments.

8.1 Migration Matrix

The migration matrix or smearing matrix shows the probability of a measured quantity x to have a true value y. This matrix also contains information of the correlations and migrations between adjacent bins. The measured quantities are represented by:

$$x_i = A_{ij} x_j \tag{8.1}$$

where A_{ij} is the migration matrix or smearing matrix, and the index j and i correspond to the reconstructed and true bins respectively. The unfolding aims to extract the true distribution x_i, however the direct inversion of A_{ij} presents problems if the matrix is singular. Even if the matrix can be inverted the method is not able to handle large statistical fluctuations caused by the negative terms of the inverse of the matrix. We can overcome these problems in the inversion of the matrix by using a regularization method. In this analysis the D'Agostini regularization method [88] based on the Bayes theorem was used to extract the unfolding matrix.

In order to choose the bins the purity and the statistical uncertainty must be considered. More then 50% of the generated events must be reconstructed well and a minimum of 100 events is required in each bin. Therefore the bin widths were selected following two requirements:

- At least 58% of true SIS events should be reconstructed in the correct bin.
- At most a 10% of fractional error in each bin is required.

If the bin size is too large, the unfolding will not consider the high-frecuency components of the true distribution, and if it is too narrow compared to the resolution the migration matrix will have large off-diagonal elements. The migration matrices for p_t, p_l and x_{bj} are shown in figures 8.1, 8.2 and 8.3. Migration matrices for other kinematic variables are shown in the Appendix E.

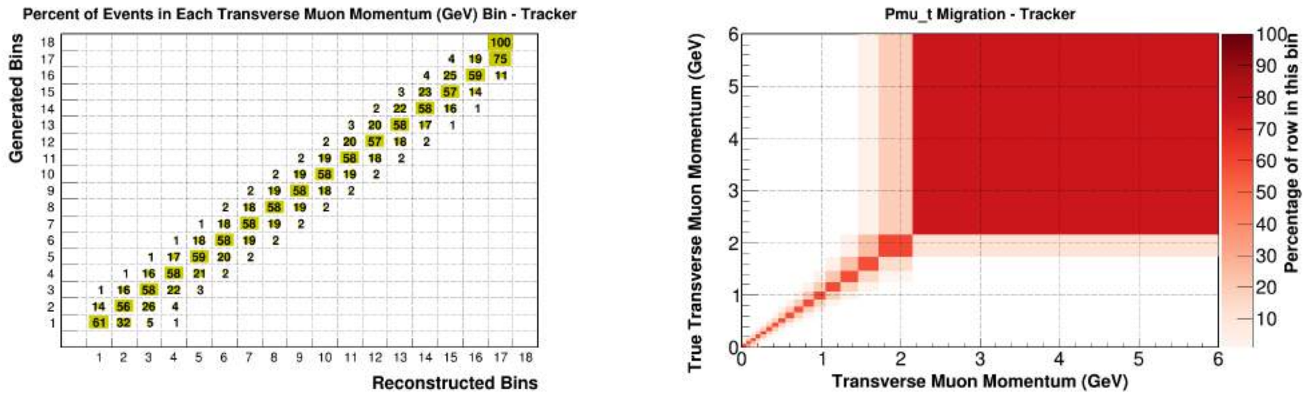

Figure 8.1: Migration matrix for p_t: purity percentages (left) and bin widths (right)

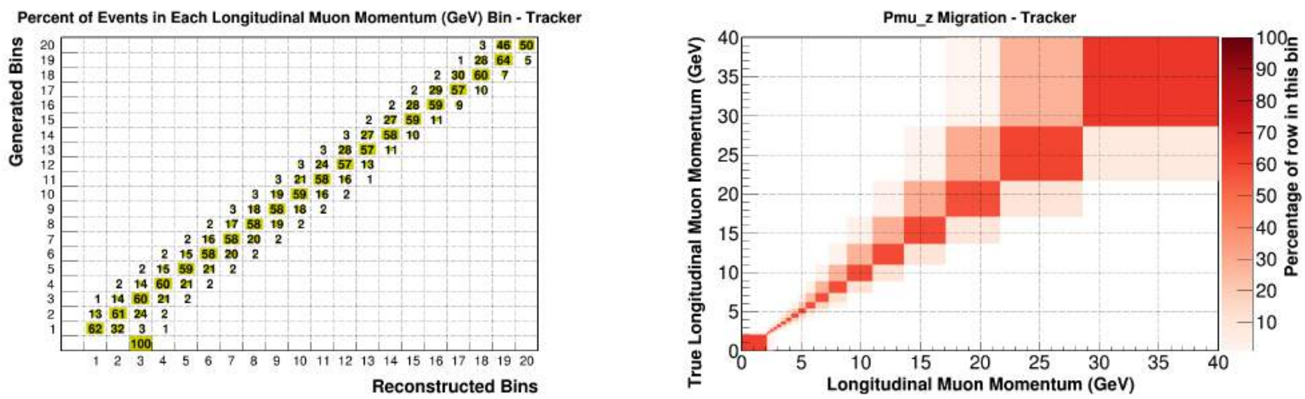

Figure 8.2: Migration matrix for p_l: purity percentages (left) and bin widths (right)

8.2 Unfolding procedure

In the context of measured and true distributions the Bayes theorem represented in equation 8.2 can be understood as stated in terms of the true bins C_i (causes), the measured bins E_j (effects) and assumed initial probability distribution of the true events as $P_0(C_i)$.

$$P(C_i|E_j) = \frac{P(E_j|C_i)P_0(C_i)}{\sum_{l=1}^{n_c} P(E|C_l)P_0(C_l)} \tag{8.2}$$

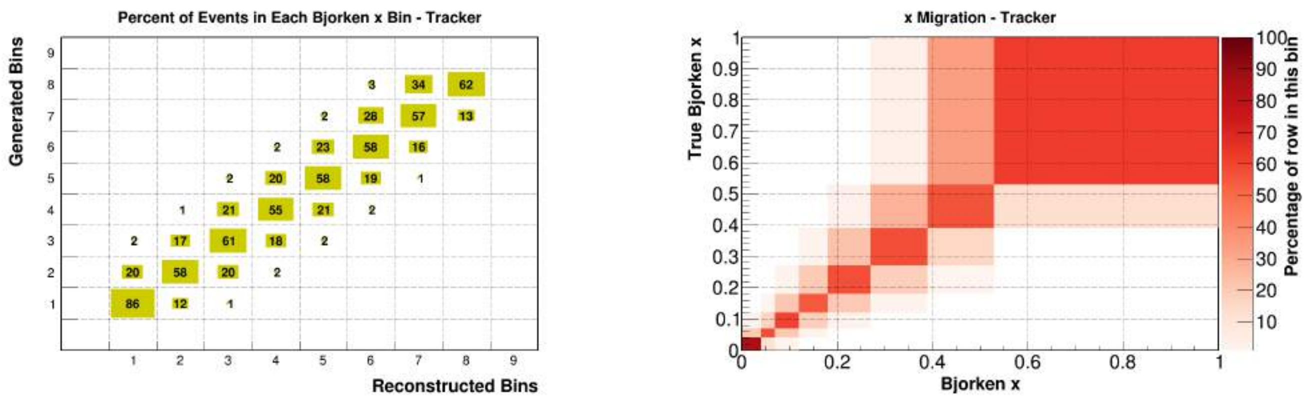

Figure 8.3: Migration matrix for x_{bj}: purity percentages (left) and bin widths (right)

The probability that an event in a measured bin j is coming from a true bin i is proportional to the assumed initial true probability distribution times the probability that an event in the true i bin is measured in j bin. The conditional probabilities $P(C_i|E_j)$ and $P(E_j|C_i)$ are recognizes as the unfolding matrix and the migration (or smearing) matrix respectively.

The conditions to note here are:

- $\sum\limits_{i=1}^{n_c} P_0(C_i) = 1$: If a event does not exist it cannot be measured.
- $\sum\limits_{i=1}^{n_c} P(C_i|E_j) = 1$: If an event is measured it must come from some true bins. This comes from the definition of the Bayes theorem.
- $0 \leq \sum\limits_{j=1}^{n_E} P(E_j|C_i) \leq 1$: A true event do not necessarily is always measured.

We can then extract the number of events in a true bin (eq. 8.3), the total number of events (eq. 8.4) and calculate the the initial true probability distribution (eq. 8.5) as follows:

$$n(C_i) = \frac{1}{\epsilon_i} \sum_{j=1}^{n_E} n(E_j) P(C_i|E_j) \tag{8.3}$$

$$N_{true} = \sum_{i=1}^{n_c} n(C_i) \tag{8.4}$$

$$P(C_i) = P(C_i|n(E)) = \frac{n(C_i)}{N_{true}} \tag{8.5}$$

If the initial distribution $P_0(C)$ is not consistent with the data, it will not agree with the final distribution extracted $P(C)$. The final distribution $P(C)$ lies between the intial and true ditribution. This suggests that a whole iterative procedure should be as follows:

2. calculate $n(C_i)$ and $P(C)$.

3. calculate the χ^2 between $n(C)$ and $n_0(C)$.

4. if the χ^2 divided by the number of degrees of freedom is not ≈ 1 so replace $P_0(C)$ by $P(C)$ and $n_0(C)$ by $n(C)$ and go to step 2.

The χ^2 stabilizes after a number of iterations and stops varying for additional iterations. The efficiencies ϵ_i in 8.3 are 1 because we correct for efficiencies after the unfolding procedure. The background subtracted distribution and the respective unfolded distribution for p_t, p_l and x_{bj} are shown in figures 8.4, 8.5 and 8.6. The background subtracted distributions for MC and data both have the systematic and statistical errors, represented as a pink bar for MC and black bars for data. The unfolding affects more Bjorken x than p_l and p_t, and it is shifting the data to higher values of Bjorken x. At the time of writing this document the implementation of the uncertainty in the unfolding was in progress. Distributions for other kinematic variables are shown in Appendix F.

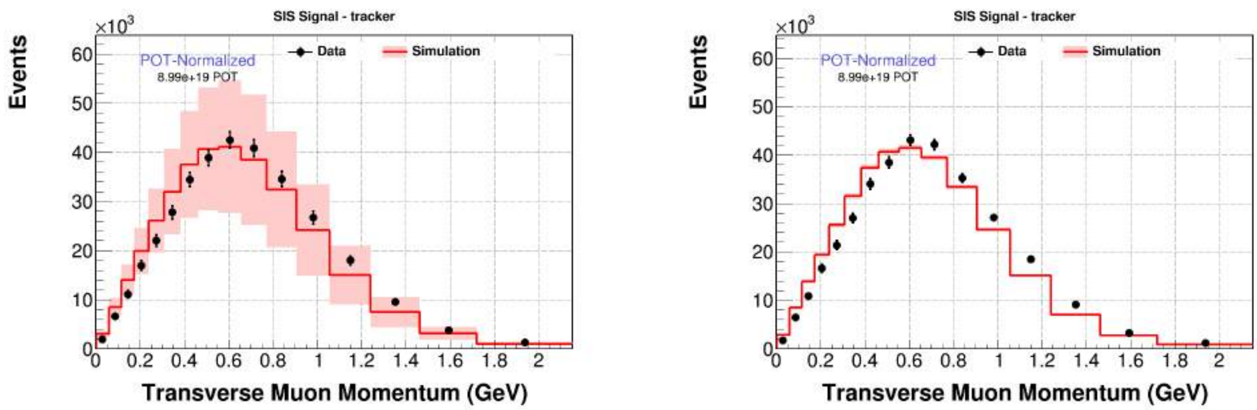

Figure 8.4: SIS events in CH per reconstructed p_t (left) and unfolded (right)

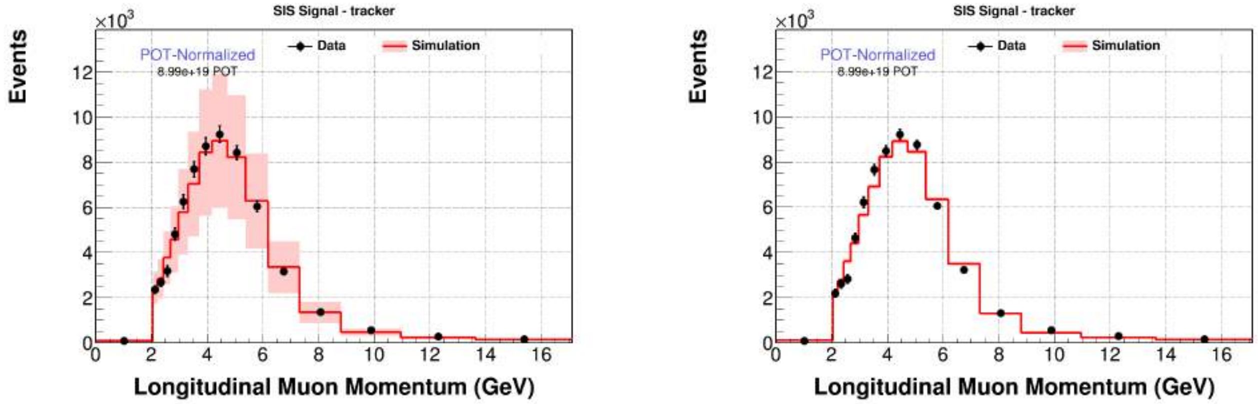

Figure 8.5: SIS events in CH per reconstructed p_l (left) and unfolded (right)

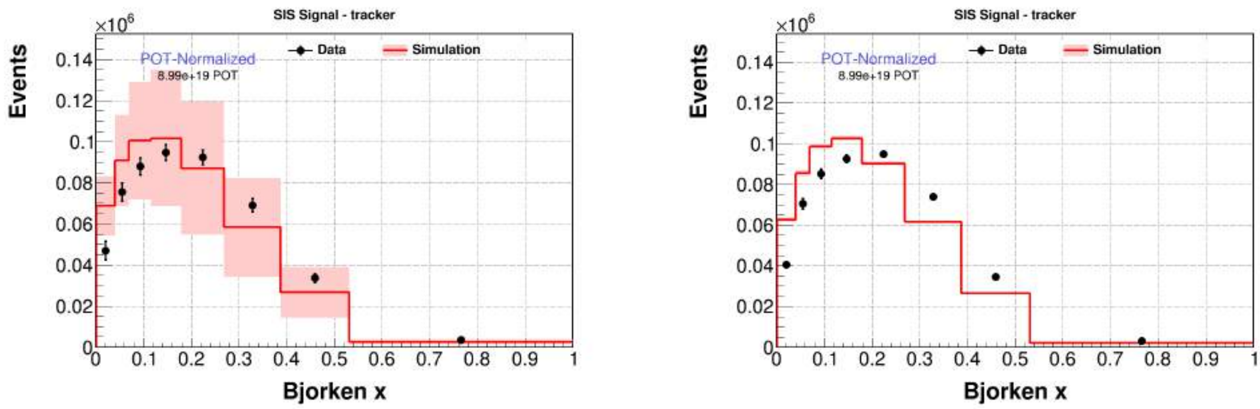

Figure 8.6: SIS events in CH per reconstructed x_{bj} (left) and unfolded (right)

Chapter 9

Differential Cross Section Calculation

The Differential Cross Section is calculated by correcting the unfolded selection sample by the efficiency, integrated flux and number of targets in the tracker region. The differential cross section formula is as follows,

$$\frac{d\sigma}{dx_i} = \frac{U_{ij}(d_j - b_j)}{\Delta x_i \epsilon_i \Phi_i N} \tag{9.1}$$

Where $(d_j - b_j)$ is the background subtracted data, U_{ij} is the unfolding matrix, Φ_i is the integrated flux, N is the number of nucleons, Δx_i is the bin width and ϵ_i is the reconstruction efficiency.

9.1 Efficiency

The reconstruction cuts (chapter 5) do not reconstruct all of our signal events. To recover the true distribution the unfolded sample is corrected by the efficiency. The efficiency is defined as the ratio of the SIS reconstructed events that are truly SIS to the total true SIS events generated. The efficiency is entirely calculated from the Monte Carlo simulation. The efficiencies for x_{bj}, p, p_μ, and p_t are shown in figures 9.1 and 9.2. Efficiency for other kinematic variables are shown in Appendix G.

$$\text{Efficiency} = \frac{\text{True SIS events that pass all reconstructed SIS cuts}}{\text{True SIS events generated}} \tag{9.2}$$

9.2 Normalization factors

The final step to extract the differential cross section is to normalize the effiency corrected sample. The normalization is composed of the integrated flux normalization, the target num-

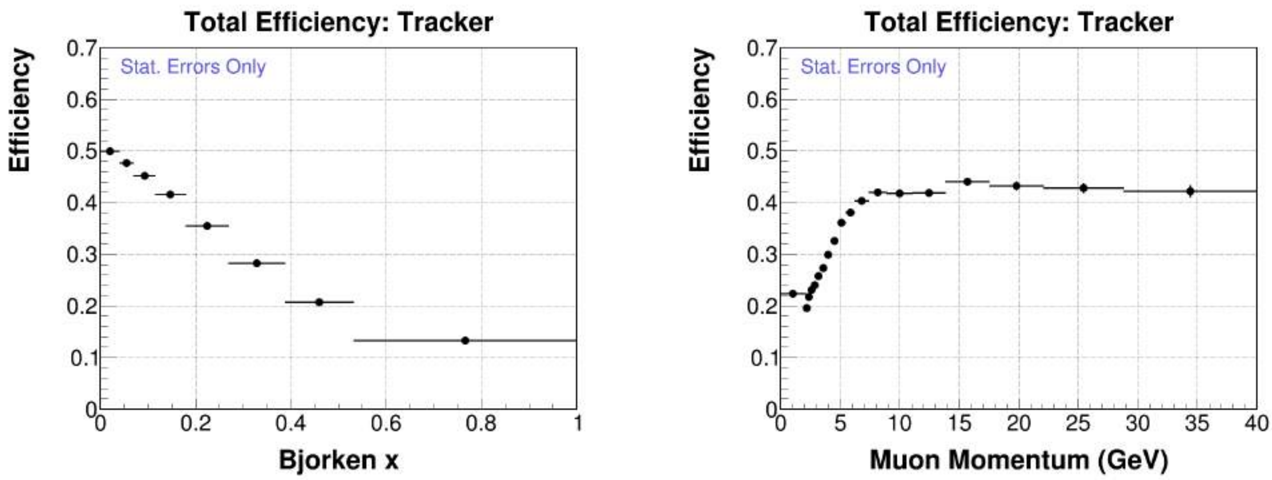

Figure 9.1: Efficiency of events in the tracker region (CH) as a function of Bjorken-x (left) and muon momentum (right).

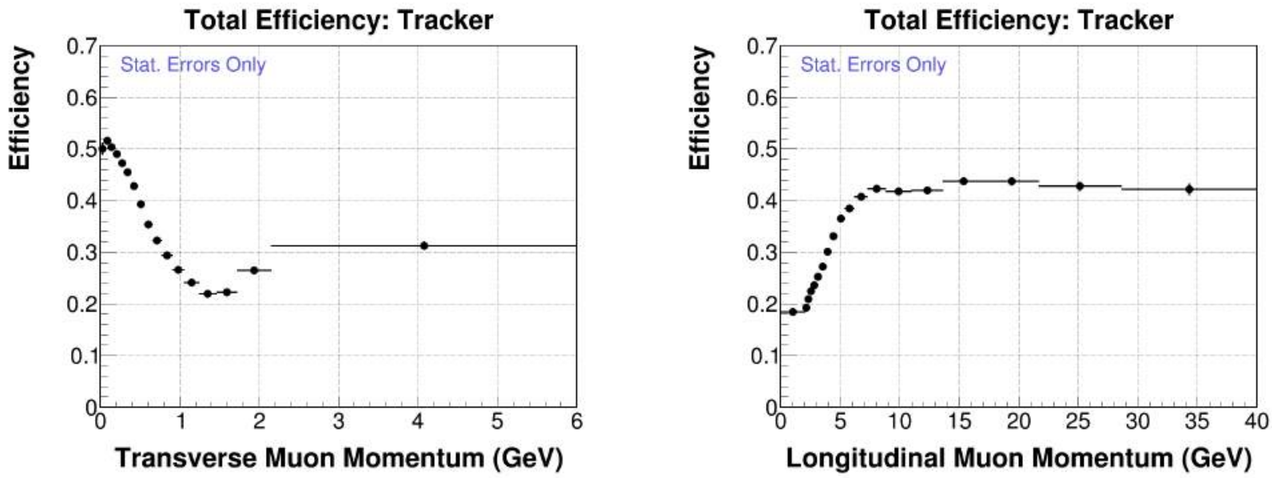

Figure 9.2: Efficiency of events in the tracker region (CH) as a function of transverse muon momentum (left) and longitudinal muon momentum (right).

ber normalization and the bin width normalization. These factors are Φ, N and Δ_i in the denominator of the differential cross section formula 9.1.

The flux is integrated in the whole neutrino energy range, the number of nucleons are calculated for the hydrocarbon scintillator (CH) contained in the tracker region fiducial volume, and the bin width is set in the migration matrix bin optimization (chapter 8.1).

9.3 Differential Cross Section Results

The Differential Cross Section per nucleon as a function of x_{bj} is presented in figure 9.3. The discrepancy at low x_{bj} is also observed in the background subtracted sample for x_{bj} (figure

8.6). The neutrino Deep Inelastic Scattering differential cross section as a function of x_{bj} in Hydrocarbon at $< E_\nu \approx 6\ GeV >$ in the MINERνA detector has been measured by other collaborators [89] and the preliminary results are shown in figure 9.4.

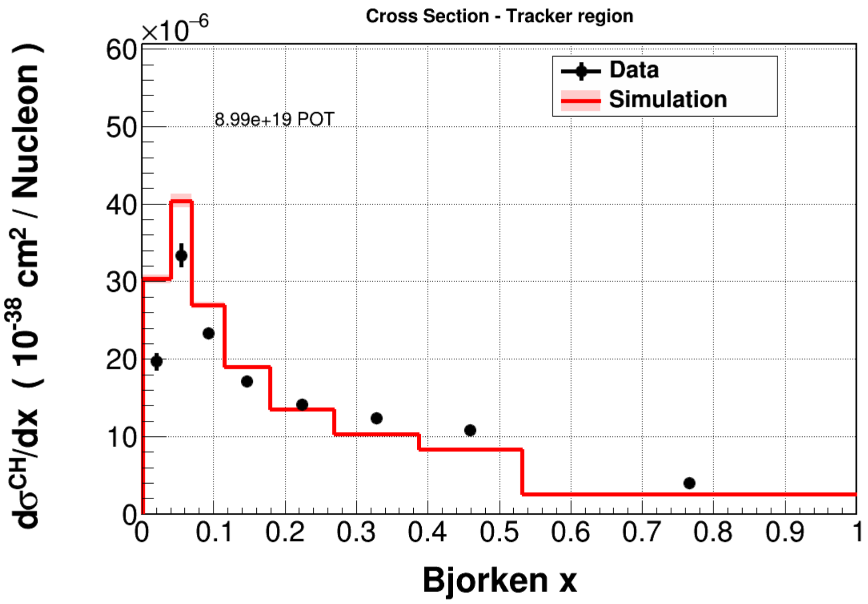

Figure 9.3: SIS Differential cross section in hydrocarbon (CH) as a function of Bjorken-x.

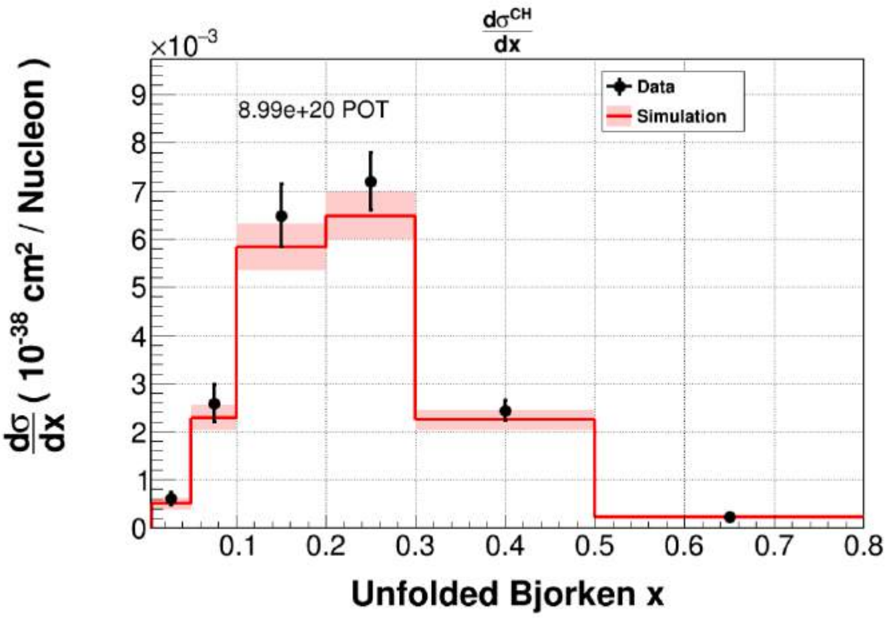

Figure 9.4: DIS Differential cross section in hydrocarbon (CH) as a function of Bjorken-x (work in progress). Figure taken from [89]

Chapter 10

Conclusions

A Shallow Inelastic Scattering sample was selected by requiring a kinematic cut in the hadronic invariant mass $1.5 < W < 2.0$ GeV. A sideband method was used to calculate the background of the signal. After the background subtraction the D'Agostini method was used to unfold the Bjorken-x distribution. The unfolded distribution is corrected by the efficiency and normalized by the integrated flux, number of nucleons and per bin width.

The errors implementation for the cross section calculation are in progress. A preliminary result for the differential cross section of SIS as a function of Bjorken-x for the central values is presented. There is an overestimation of Monte Carlo at low x_{bj}. The SIS neutrino cross section peaks between Bjorken-x values of 0.04-0.06 which is lower than the DIS's cross section which peaks between Bjorken-x values of 0.2-0.3 (figure 9.4). Finally it is worth to mention the antineutrino SIS analysis in Hydrocarbon is in progress and the neutrino SIS cross section is expected to be published in the next year.

Chapter 11

Appendix

Appendix A

Event Simulation

A.1 GENIE Event Generator

MINERνA uses GENIE 2.12.6 [60] to generate events of neutrino interactions with matter. The generation of events uses the Monte Carlo technique and starts by calculating the total cross section for an especific process as a function of Neutrino Energy E_ν by integrating the differential cross section of that process over the E_ν spectrum.

A.2 GENIE Models for SIS

GENIE uses underlying models to calculate the differential cross section for an specific process. To calculate the differential cross section a model requires a initial state which is calculated using a set of random values generated by GENIE. These values must respect the phase space of the $\nu_\mu + N$ interaction otherwise it would be considered an unphysical event. The SIS differential cross section is modeled by two models: The Bodek Yang model [61] and the Rein-Sehgal model [62].

The Bodek Yang model simulates events of $W > 1.3$ GeV and calculates nucleon parton distribution functions (PDFs) using the scaling variable ϵ to account for nuclear mass modification and higher twist effects [90]. PDFs describe the makeup of the nucleon in terms of valence and sea quarks and the ϵ (equation A.1) dependance on Q^2 is tuned to account for the twist effects which appears outside the experimental DIS region ($W > 2$ GeV and $Q^2 > 1$ GeV).

$$\epsilon = F(x_{bj}, Q^2) \tag{A.1}$$

The Baryon resonances production in the charged current channel is implemented in the Rein-Sehgal model. Only 16 resonances (figure A.1) were included for this implementation and the interferences between neighboring resonances were not been considered [60]. Feyman-Kislinger-Ravndal model of baryon resonances is used in this model, which provides wavefunctions for the resonances as excited states of a 3-quark system in a relativistic harmonic oscillator potential with spin-flavor symmetry [91].

Resonance	GENIE ID	Mass (GeV)	Width (GeV)
$P_{33}(1232)$		1.232	0.120
$S_{11}(1535)$		1.535	0.150
$D_{13}(1520)$		1.520	0.120
$S_{11}(1650)$		1.650	0.150
$D_{13}(1700)$		1.700	0.100
$D_{15}(1675)$		1.675	0.150
$S_{31}(1620)$		1.620	0.150
$D_{33}(1700)$		1.700	0.300
$P_{11}(1440)$		1.440	0.350
$P_{13}(1720)$		1.720	0.150
$F_{15}(1680)$		1.680	0.130
$P_{31}(1910)$		1.910	0.250
$P_{33}(1920)$		1.920	0.200
$F_{35}(1905)$		1.905	0.350
$F_{37}(1950)$		1.950	0.300
$P_{11}(1710)$		1.710	0.100

Table A.1: Resonances included in the implementation of the Rein-Seghal model

A.3 Shallow Inelastic Scattering Modeling

Assuming that all exclusive low multiplicity inelastic reactions are proceeding mainly through neutrino resonance production. The $CC\ \nu N$ scattering cross section of the transition region can be expressed as:

$$\sigma^{tot} = \sigma^{QEL} \oplus \sigma^{RES} \oplus \sigma^{DIS} \tag{A.2}$$

Small contributions such as, the coherent and elastic νe^- scattering that contribute to the total cross section in the few GeV energy range were omitted from the expression above. Following these lines we can express the inelastic differential cross section as:

$$\frac{d^2\sigma^{RES}}{dQ^2 dW} = \sum_k \left(\frac{d^2\sigma^{R/S}}{dQ^2 dW}\right)_k . \Theta(Wcut - W) \tag{A.3}$$

The first term represents the contribution from all low multiplicity inelastic channels proceeding via resonance production and the second term represents the contribution from the DIS interactions. The resonant term and the DIS are computed as follows:

$$\frac{d^2\sigma^{inel}}{dQ^2dW} = \frac{d^2\sigma^{RES}}{dQ^2dW} + \frac{d^2\sigma^{DIS}}{dQ^2dW} \tag{A.4}$$

$$\frac{d^2\sigma^{DIS}}{dQ^2dW} = \frac{d^2\sigma^{DIS,BY}}{dQ^2dW} \ . \ \Theta(W - Wcut) + \frac{d^2\sigma^{DIS,BY}}{dQ^2dW} \ . \ \Theta(Wcut - W) \ . \ \sum_m f_m \tag{A.5}$$

The k index in the resonance term runs over all 16 (figure A.1) baryon resonances and the W_{cut} is a configurable parameter. The DIS has a term of the Bodek-Yang model differential cross section modulated in the region were resonances dominate $W < W_{cut}$, in order to reach a RES/DIS mixture that agrees with the inclusive cross section data [60]. In the expresion A.5 the f_m factors are computed as $f_m = R_m.P_m^{had}$ where R_m is a tunable parameter and P_m^{had} is the probability that the final state hadronic system multiplicty is m. Fitting the model to inclusive and exclusive (one and two-pion) production neutrino interaction channels allows us to extract the default values for the transition region parameteres, $W_{cut} = 1.7 \ GeV/c^2$, $R_2(\nu p) = R_2(\bar{\nu} n) = 0.1, R_2(\nu n) = R_2(\bar{\nu} p) = 0.3$, and $R_m = 1.0$ for all $m > 2$ reactions. It must be hightlighted thatthe DIS definition used here is not the experimental definition of DIS ($Q^2 > 1 \ GeV^2$ and $W > 2 \ GeV$) indicated before in the text. For simplicity the DIS expressed in this chapter will be referred as GENIE DIS in the rest of the text.

Appendix B

Hadronic energy per bin correction

A per-bin correction is made using the reconstructed and true recoil energy corrected by α, $E_{reconstructed}$ and E_{true}. The mean of $\eta = \Delta E/E_{true}$ with $\Delta E = E_{reconstructed} - E_{true}$ and the mean $< E_{true} >$ in each true bin were used to construct a polyline $(x(E_{recoil}), y(E'_{recoil}))$:

$$x(E_{recoil}) =< E_{recoil,true} > (1 + \eta) \tag{B.1}$$

$$y(E'_{recoil}) =< E_{recoil,true} > \tag{B.2}$$

The polyline is used correct the recoil energy by mapping recoil energy values from the E_{recoil} to E'_{recoil}. The global scale factor $\alpha = 1.51298$, the calorimetric energy resolution and the polyline calculated are shown in figures 5.2 and B.1. The distributions $\eta = \Delta E/E_{true}$ in each true bin are shown in figure B.2

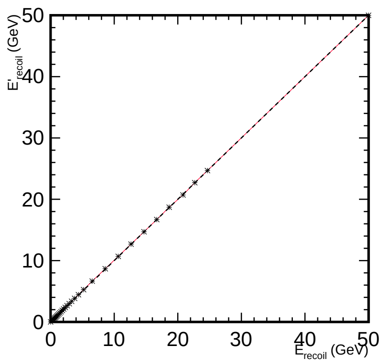

Figure B.1: Polyline correction for Charged Current inclusive events in the MINERνA detector

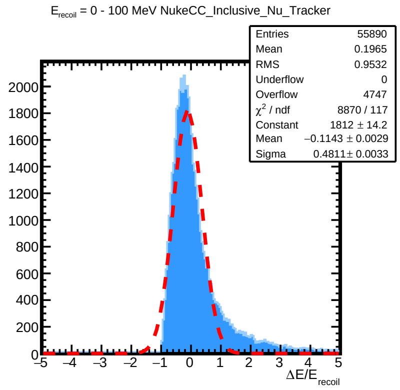
E_recoil = 0 - 100 MeV NukeCC_Inclusive_Nu_Tracker
Entries 55890
Mean 0.1965
RMS 0.9532
Underflow 0
Overflow 4747
χ² / ndf 8870 / 117
Constant 1812 ± 14.2
Mean −0.1143 ± 0.0029
Sigma 0.4811± 0.0033
ΔE/E_recoil

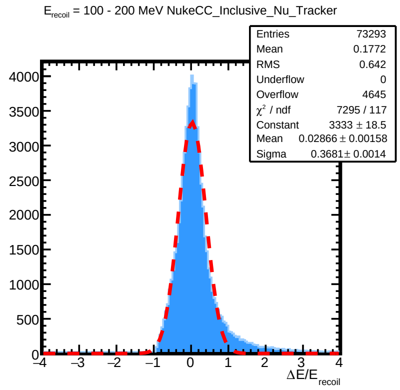
E_recoil = 100 - 200 MeV NukeCC_Inclusive_Nu_Tracker
Entries 73293
Mean 0.1772
RMS 0.642
Underflow 0
Overflow 4645
χ² / ndf 7295 / 117
Constant 3333 ± 18.5
Mean 0.02866 ± 0.00158
Sigma 0.3681± 0.0014
ΔE/E_recoil

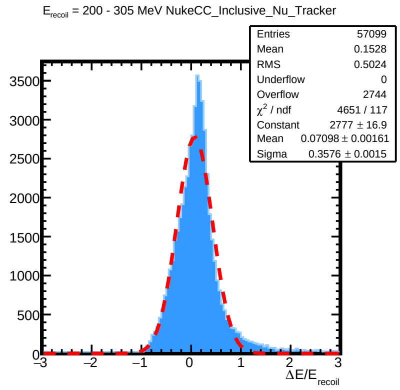
E_recoil = 200 - 305 MeV NukeCC_Inclusive_Nu_Tracker
Entries 57099
Mean 0.1528
RMS 0.5024
Underflow 0
Overflow 2744
χ² / ndf 4651 / 117
Constant 2777 ± 16.9
Mean 0.07098 ± 0.00161
Sigma 0.3576 ± 0.0015
ΔE/E_recoil

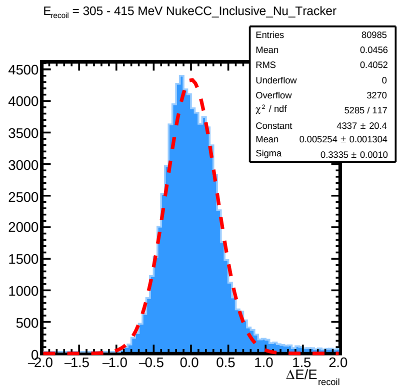
E_recoil = 305 - 415 MeV NukeCC_Inclusive_Nu_Tracker
Entries 80985
Mean 0.0456
RMS 0.4052
Underflow 0
Overflow 3270
χ² / ndf 5285 / 117
Constant 4337 ± 20.4
Mean 0.005254 ± 0.001304
Sigma 0.3335 ± 0.0010
ΔE/E_recoil

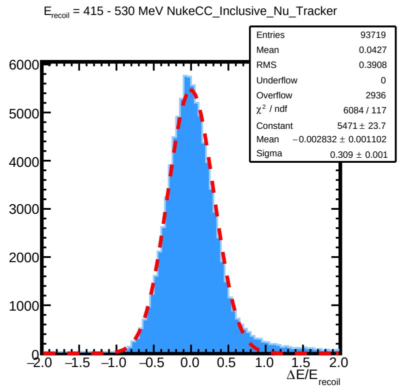
E_recoil = 415 - 530 MeV NukeCC_Inclusive_Nu_Tracker
Entries 93719
Mean 0.0427
RMS 0.3908
Underflow 0
Overflow 2936
χ² / ndf 6084 / 117
Constant 5471 ± 23.7
Mean −0.002832 ± 0.001102
Sigma 0.309 ± 0.001
ΔE/E_recoil

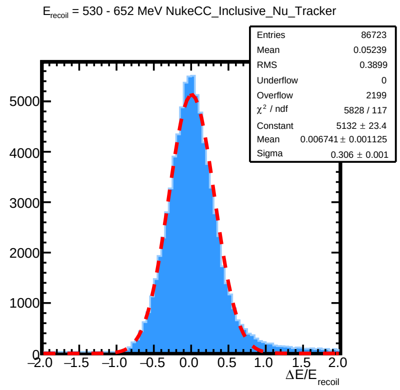
E_recoil = 530 - 652 MeV NukeCC_Inclusive_Nu_Tracker
Entries 86723
Mean 0.05239
RMS 0.3899
Underflow 0
Overflow 2199
χ² / ndf 5828 / 117
Constant 5132 ± 23.4
Mean 0.006741 ± 0.001125
Sigma 0.306 ± 0.001
ΔE/E_recoil

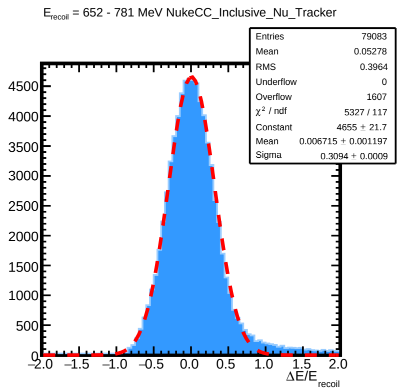
E_recoil = 652 - 781 MeV NukeCC_Inclusive_Nu_Tracker
Entries 79083
Mean 0.05278
RMS 0.3964
Underflow 0
Overflow 1607
χ² / ndf 5327 / 117
Constant 4655 ± 21.7
Mean 0.006715 ± 0.001197
Sigma 0.3094 ± 0.0009
ΔE/E_recoil

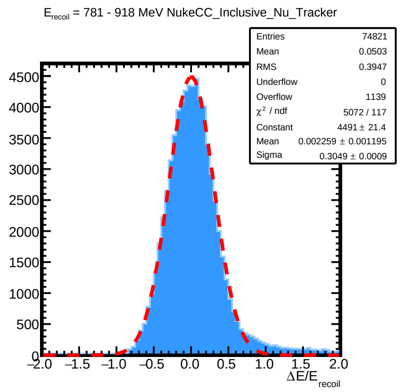
E_recoil = 781 - 918 MeV NukeCC_Inclusive_Nu_Tracker
Entries 74821
Mean 0.0503
RMS 0.3947
Underflow 0
Overflow 1139
χ² / ndf 5072 / 117
Constant 4491 ± 21.4
Mean 0.002259 ± 0.001195
Sigma 0.3049 ± 0.0009
ΔE/E_recoil

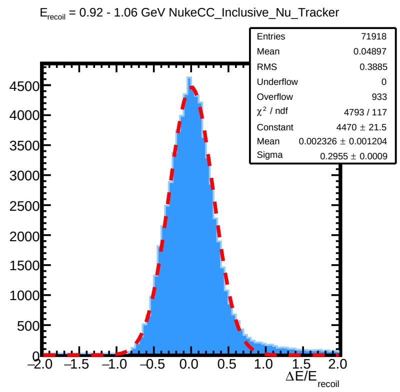
E_recoil = 0.92 - 1.06 GeV NukeCC_Inclusive_Nu_Tracker
Entries 71918
Mean 0.04897
RMS 0.3885
Underflow 0
Overflow 933
χ² / ndf 4793 / 117
Constant 4470 ± 21.5
Mean 0.002326 ± 0.001204
Sigma 0.2955 ± 0.0009
ΔE/E_recoil

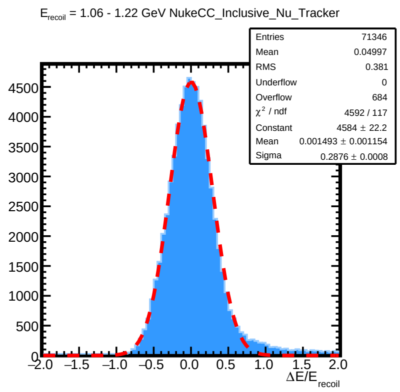
E_recoil = 1.06 - 1.22 GeV NukeCC_Inclusive_Nu_Tracker
Entries 71346
Mean 0.04997
RMS 0.381
Underflow 0
Overflow 684
χ² / ndf 4592 / 117
Constant 4584 ± 22.2
Mean 0.001493 ± 0.001154
Sigma 0.2876 ± 0.0008
ΔE/E_recoil

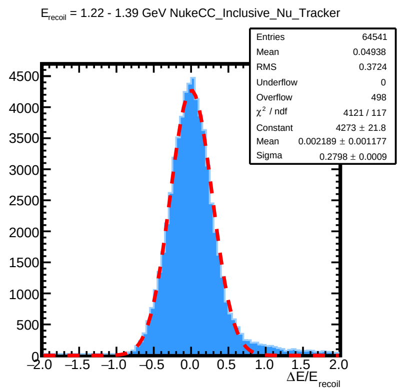
E_recoil = 1.22 - 1.39 GeV NukeCC_Inclusive_Nu_Tracker
Entries 64541
Mean 0.04938
RMS 0.3724
Underflow 0
Overflow 498
χ² / ndf 4121 / 117
Constant 4273 ± 21.8
Mean 0.002189 ± 0.001177
Sigma 0.2798 ± 0.0009
ΔE/E_recoil

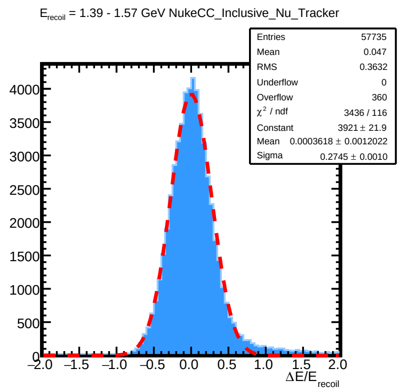
E_recoil = 1.39 - 1.57 GeV NukeCC_Inclusive_Nu_Tracker
Entries 57735
Mean 0.047
RMS 0.3632
Underflow 0
Overflow 360
χ² / ndf 3436 / 116
Constant 3921 ± 21.9
Mean 0.0003618 ± 0.0012022
Sigma 0.2745 ± 0.0010
ΔE/E_recoil

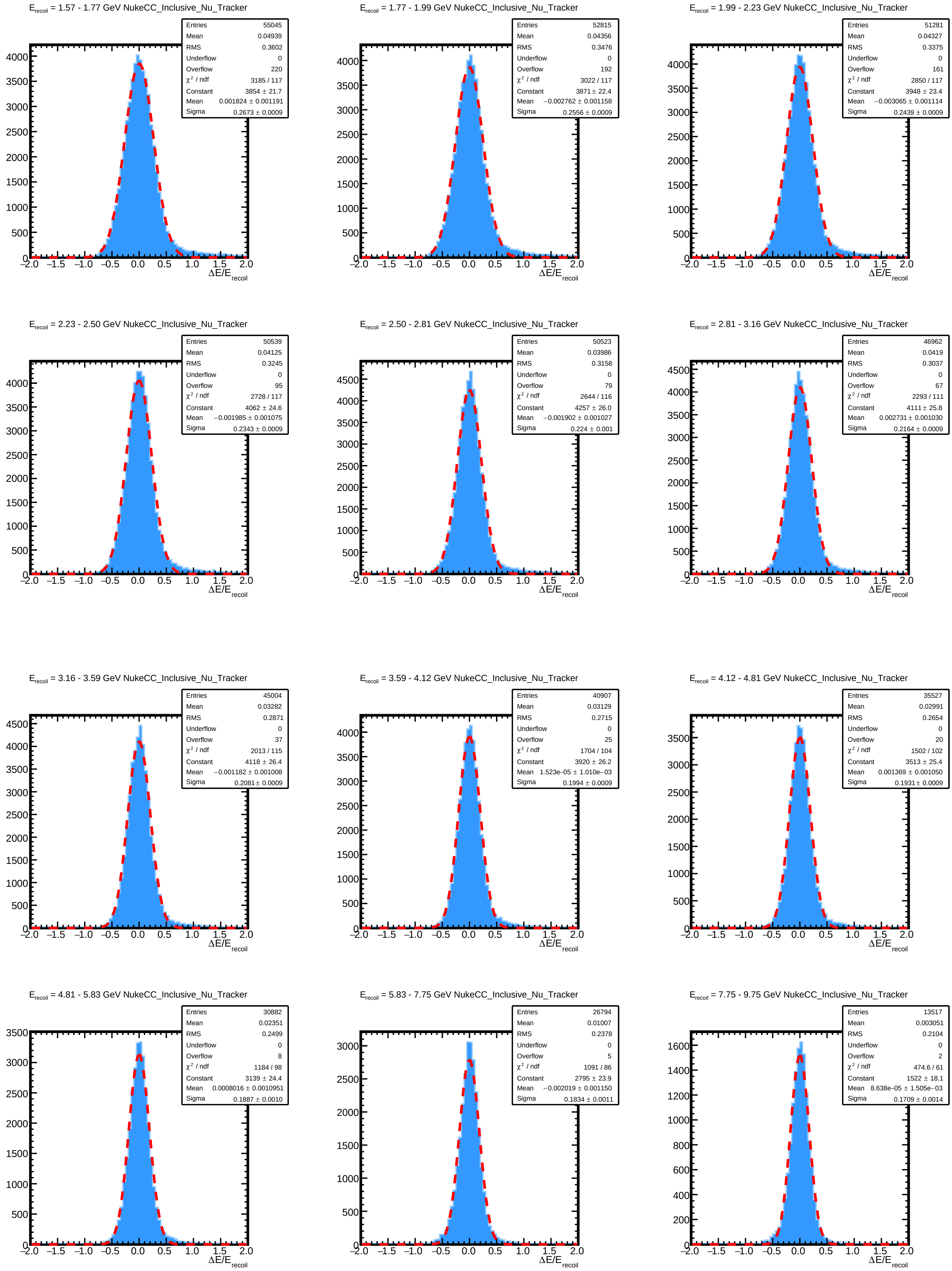

E_{recoil} = 1.57 - 1.77 GeV NukeCC_Inclusive_Nu_Tracker
Entries 55045
Mean 0.04939
RMS 0.3602
Underflow 0
Overflow 220
χ^2 / ndf 3185 / 117
Constant 3854 ± 21.7
Mean 0.001824 ± 0.001191
Sigma 0.2673 ± 0.0009
E_{recoil} = 1.77 - 1.99 GeV NukeCC_Inclusive_Nu_Tracker
Entries 52815
Mean 0.04356
RMS 0.3476
Underflow 0
Overflow 192
χ^2 / ndf 3022 / 117
Constant 3871 ± 22.4
Mean −0.002762 ± 0.001158
Sigma 0.2556 ± 0.0009
E_{recoil} = 1.99 - 2.23 GeV NukeCC_Inclusive_Nu_Tracker
Entries 51281
Mean 0.04327
RMS 0.3375
Underflow 0
Overflow 161
χ^2 / ndf 2850 / 117
Constant 3948 ± 23.4
Mean −0.003065 ± 0.001114
Sigma 0.2439 ± 0.0009
E_{recoil} = 2.23 - 2.50 GeV NukeCC_Inclusive_Nu_Tracker
Entries 50539
Mean 0.04125
RMS 0.3245
Underflow 0
Overflow 95
χ^2 / ndf 2728 / 117
Constant 4062 ± 24.6
Mean −0.001985 ± 0.001075
Sigma 0.2343 ± 0.0009
E_{recoil} = 2.50 - 2.81 GeV NukeCC_Inclusive_Nu_Tracker
Entries 50523
Mean 0.03986
RMS 0.3158
Underflow 0
Overflow 79
χ^2 / ndf 2644 / 116
Constant 4257 ± 26.0
Mean −0.001902 ± 0.001027
Sigma 0.224 ± 0.001
E_{recoil} = 2.81 - 3.16 GeV NukeCC_Inclusive_Nu_Tracker
Entries 46962
Mean 0.0419
RMS 0.3037
Underflow 0
Overflow 67
χ^2 / ndf 2293 / 111
Constant 4111 ± 25.8
Mean 0.002731 ± 0.001030
Sigma 0.2164 ± 0.0009
E_{recoil} = 3.16 - 3.59 GeV NukeCC_Inclusive_Nu_Tracker
Entries 45004
Mean 0.03282
RMS 0.2871
Underflow 0
Overflow 37
χ^2 / ndf 2013 / 115
Constant 4118 ± 26.4
Mean −0.001182 ± 0.001008
Sigma 0.2081 ± 0.0009
E_{recoil} = 3.59 - 4.12 GeV NukeCC_Inclusive_Nu_Tracker
Entries 40907
Mean 0.03129
RMS 0.2715
Underflow 0
Overflow 25
χ^2 / ndf 1704 / 104
Constant 3920 ± 26.2
Mean 1.523e−05 ± 1.010e−03
Sigma 0.1994 ± 0.0009
E_{recoil} = 4.12 - 4.81 GeV NukeCC_Inclusive_Nu_Tracker
Entries 35527
Mean 0.02991
RMS 0.2654
Underflow 0
Overflow 20
χ^2 / ndf 1502 / 102
Constant 3513 ± 25.4
Mean 0.001369 ± 0.001050
Sigma 0.1931 ± 0.0009
E_{recoil} = 4.81 - 5.83 GeV NukeCC_Inclusive_Nu_Tracker
Entries 30882
Mean 0.02351
RMS 0.2499
Underflow 0
Overflow 8
χ^2 / ndf 1184 / 98
Constant 3139 ± 24.4
Mean 0.0008016 ± 0.0010951
Sigma 0.1887 ± 0.0010
E_{recoil} = 5.83 - 7.75 GeV NukeCC_Inclusive_Nu_Tracker
Entries 26794
Mean 0.01007
RMS 0.2378
Underflow 0
Overflow 5
χ^2 / ndf 1091 / 86
Constant 2795 ± 23.9
Mean −0.002019 ± 0.001150
Sigma 0.1834 ± 0.0011
E_{recoil} = 7.75 - 9.75 GeV NukeCC_Inclusive_Nu_Tracker
Entries 13517
Mean 0.003051
RMS 0.2104
Underflow 0
Overflow 2
χ^2 / ndf 474.6 / 61
Constant 1522 ± 18.1
Mean 8.638e−05 ± 1.505e−03
Sigma 0.1709 ± 0.0014
$\Delta E/E_{recoil}$

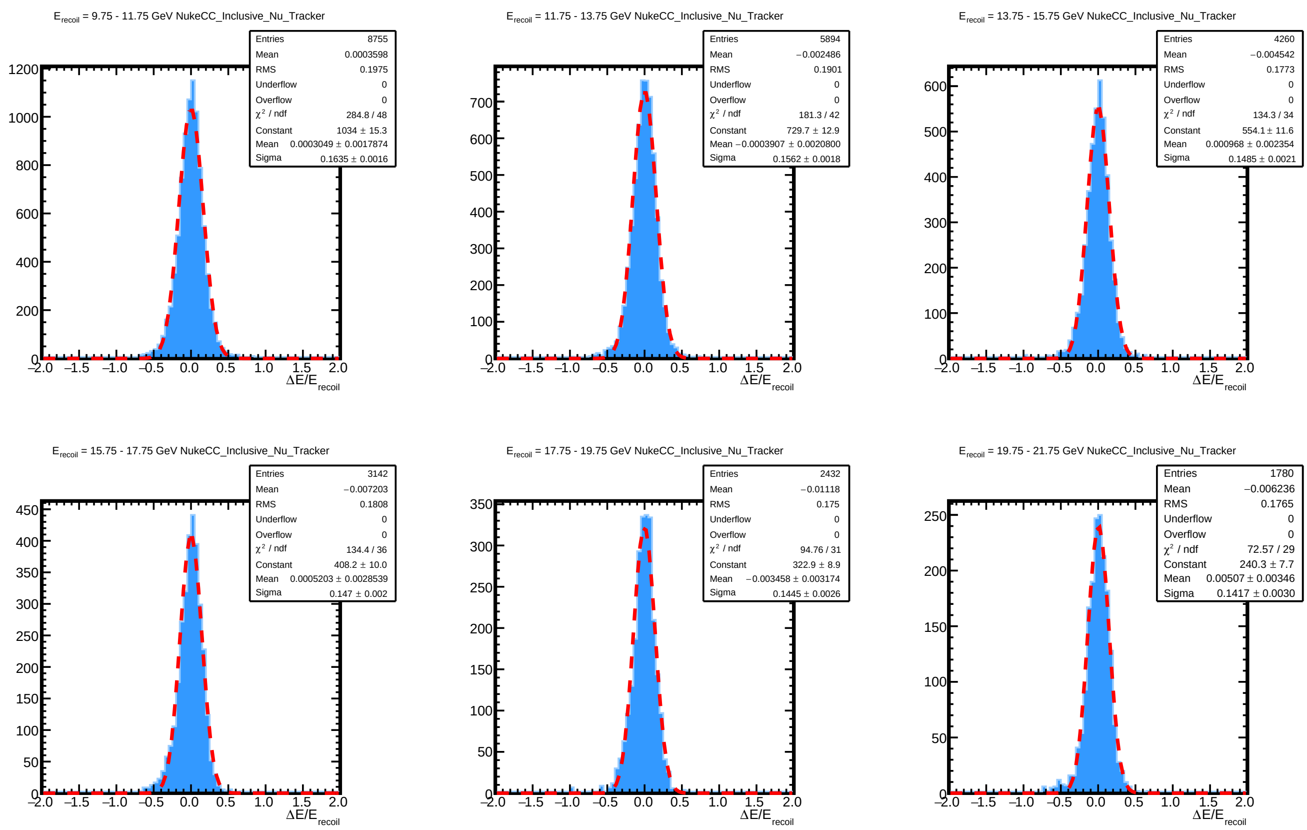

E_recoil = 9.75 - 11.75 GeV NukeCC_Inclusive_Nu_Tracker
Entries 8755
Mean 0.0003598
RMS 0.1975
Underflow 0
Overflow 0
χ² / ndf 284.8 / 48
Constant 1034 ± 15.3
Mean 0.0003049 ± 0.0017874
Sigma 0.1635 ± 0.0016
ΔE/E_recoil
E_recoil = 11.75 - 13.75 GeV NukeCC_Inclusive_Nu_Tracker
Entries 5894
Mean −0.002486
RMS 0.1901
Underflow 0
Overflow 0
χ² / ndf 181.3 / 42
Constant 729.7 ± 12.9
Mean −0.0003907 ± 0.0020800
Sigma 0.1562 ± 0.0018
ΔE/E_recoil
E_recoil = 13.75 - 15.75 GeV NukeCC_Inclusive_Nu_Tracker
Entries 4260
Mean −0.004542
RMS 0.1773
Underflow 0
Overflow 0
χ² / ndf 134.3 / 34
Constant 554.1 ± 11.6
Mean 0.000968 ± 0.002354
Sigma 0.1485 ± 0.0021
ΔE/E_recoil
E_recoil = 15.75 - 17.75 GeV NukeCC_Inclusive_Nu_Tracker
Entries 3142
Mean −0.007203
RMS 0.1808
Underflow 0
Overflow 0
χ² / ndf 134.4 / 36
Constant 408.2 ± 10.0
Mean 0.0005203 ± 0.0028539
Sigma 0.147 ± 0.002
ΔE/E_recoil
E_recoil = 17.75 - 19.75 GeV NukeCC_Inclusive_Nu_Tracker
Entries 2432
Mean −0.01118
RMS 0.175
Underflow 0
Overflow 0
χ² / ndf 94.76 / 31
Constant 322.9 ± 8.9
Mean −0.003458 ± 0.003174
Sigma 0.1445 ± 0.0026
ΔE/E_recoil
E_recoil = 19.75 - 21.75 GeV NukeCC_Inclusive_Nu_Tracker
Entries 1780
Mean −0.006236
RMS 0.1765
Underflow 0
Overflow 0
χ² / ndf 72.57 / 29
Constant 240.3 ± 7.7
Mean 0.00507 ± 0.00346
Sigma 0.1417 ± 0.0030
ΔE/E_recoil

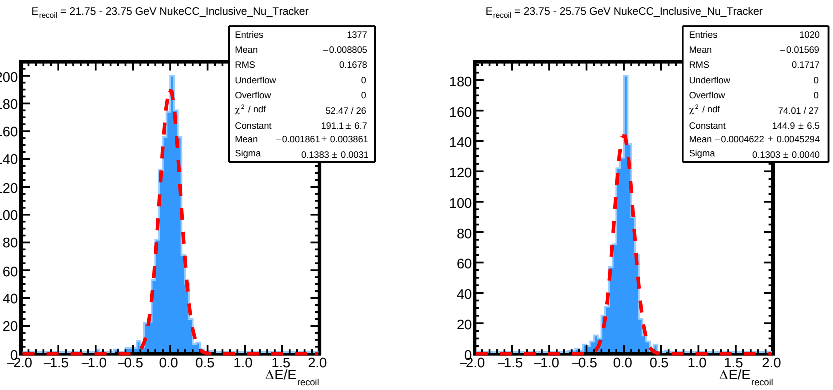

Figure B.2: Distributions of $\eta = \Delta E/E_{true}$ in each true energy bin used to create the polyline.

Appendix C

Sidebands tuning

Tuned and untuned distributions for kinematic variables in the Sidebands are presented.

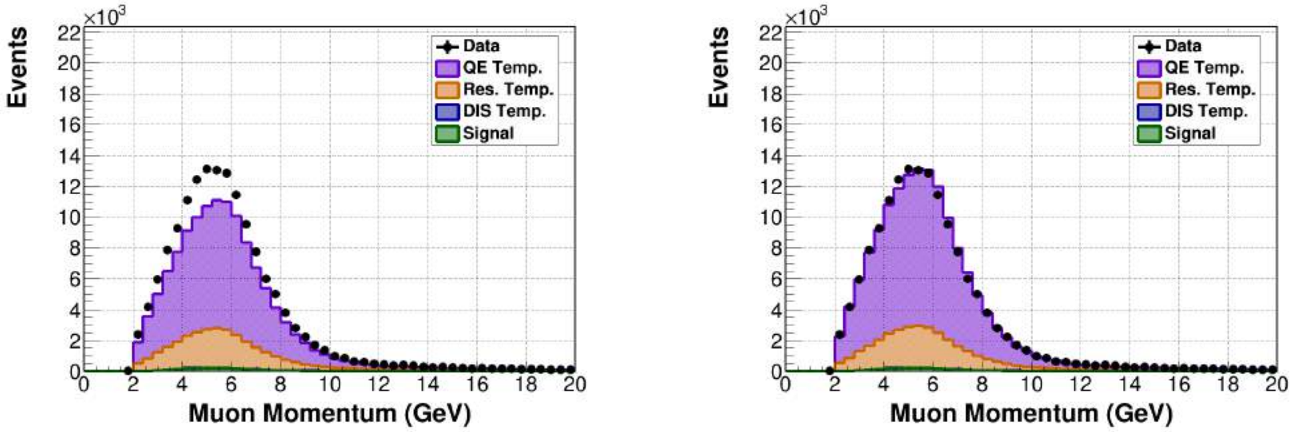

Figure C.1: p distribution in Sideband QE showing the contributions from the templates. Left: Untuned. Right: Tuned with the p_l scale factors in table 6.1

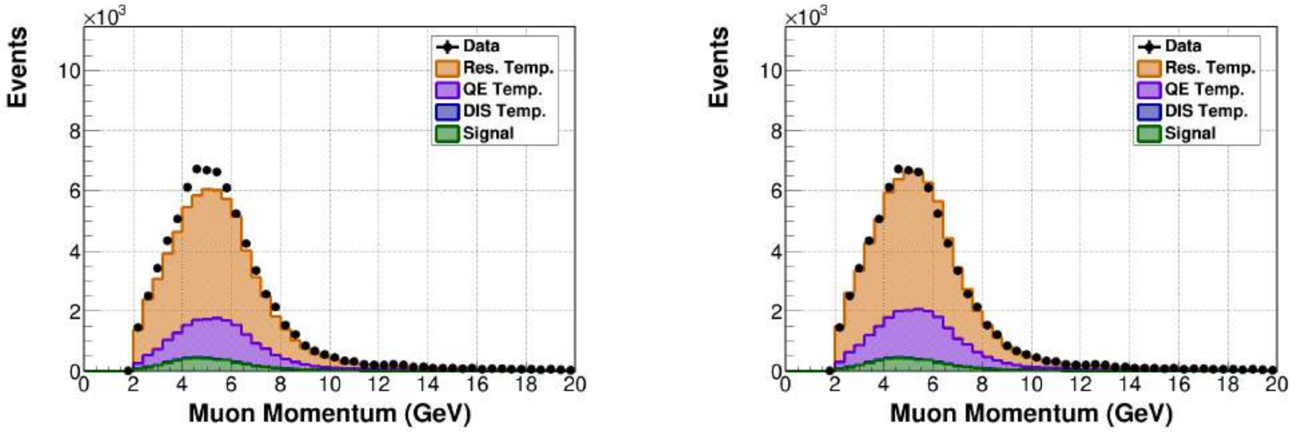

Figure C.2: p distribution in Sideband RES showing the contributions from the templates. Left: Untuned. Right: Tuned with the p_l scale factors in table 6.1

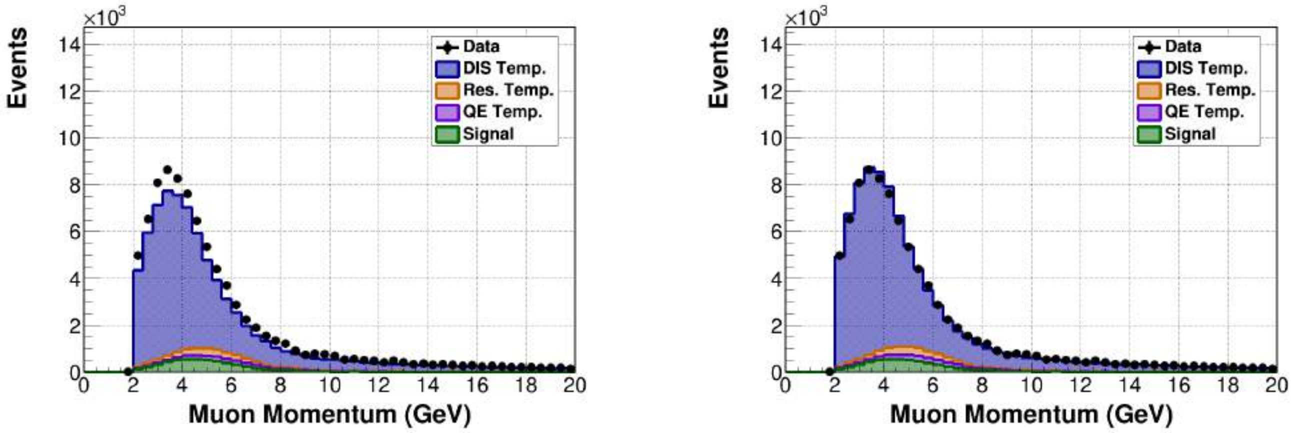

Figure C.3: p distribution in Sideband DIS showing the contributions from the templates. Left: Untuned. Right: Tuned with the p_l scale factors in table 6.1

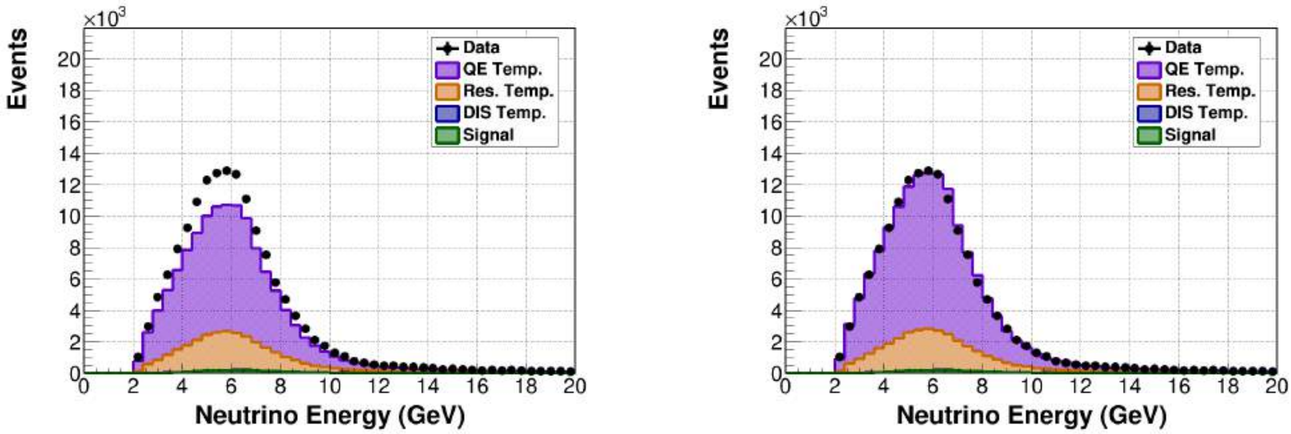

Figure C.4: E_ν distribution in Sideband QE showing the contributions from the templates. Left: Untuned. Right: Tuned with the p_l scale factors in table 6.1

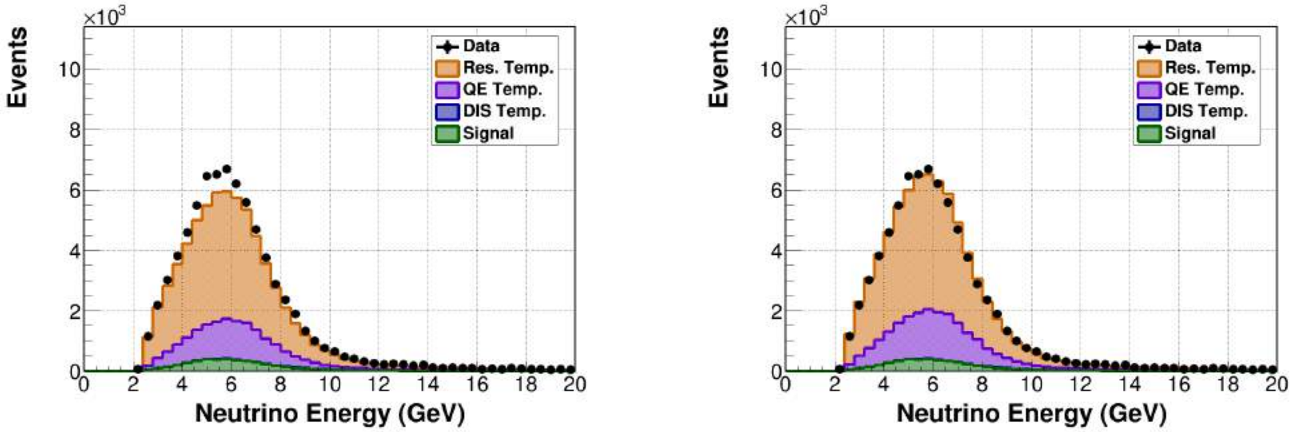

Figure C.5: E_ν distribution in Sideband RES showing the contributions from the templates. Left: Untuned. Right: Tuned with the p_l scale factors in table 6.1

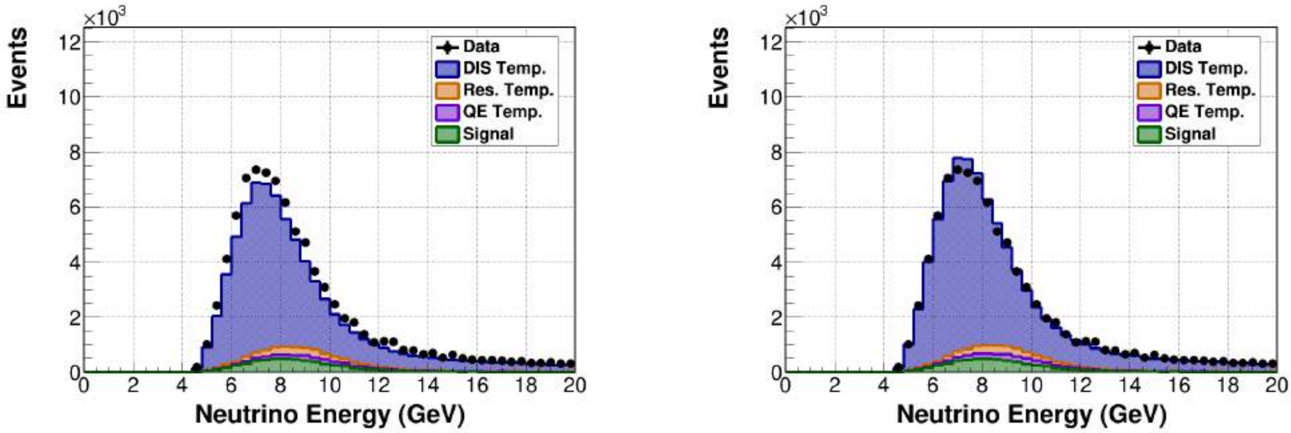

Figure C.6: E_ν distribution in Sideband DIS showing the contributions from the templates. Left: Untuned. Right: Tuned with the p_l scale factors in table 6.1

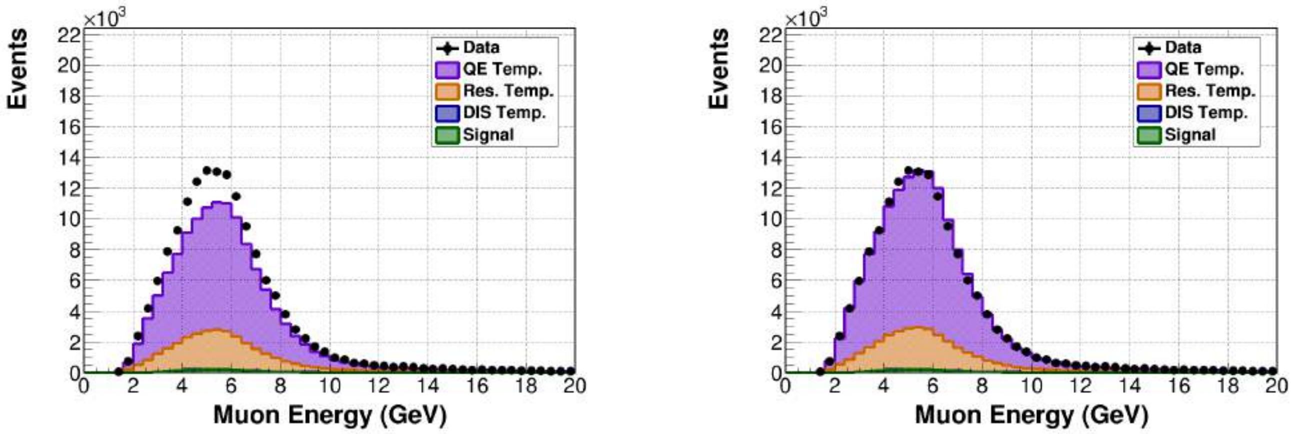

Figure C.7: E_μ distribution in Sideband QE showing the contributions from the templates. Left: Untuned. Right: Tuned with the p_l scale factors in table 6.1

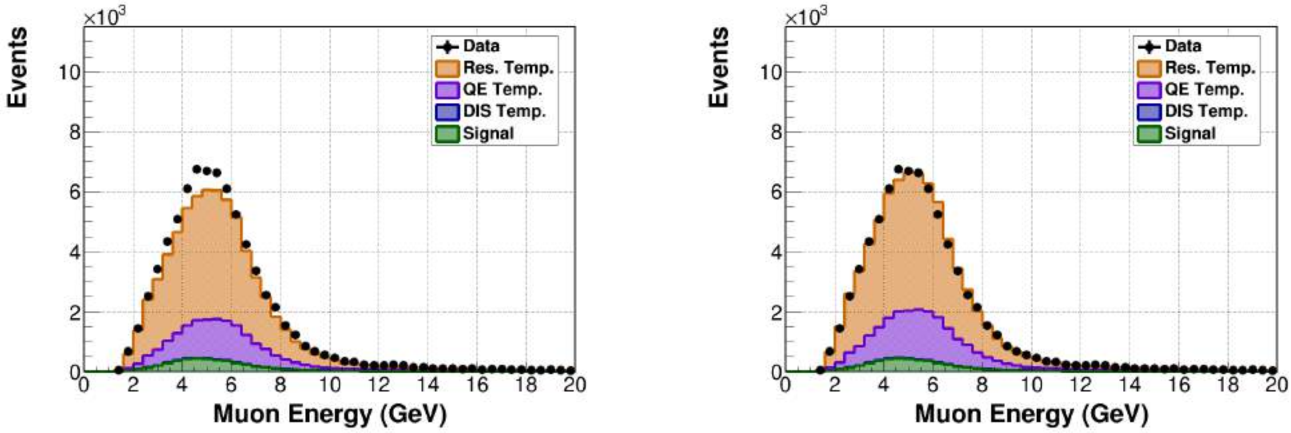

Figure C.8: E_μ distribution in Sideband RES showing the contributions from the templates. Left: Untuned. Right: Tuned with the p_l scale factors in table 6.1

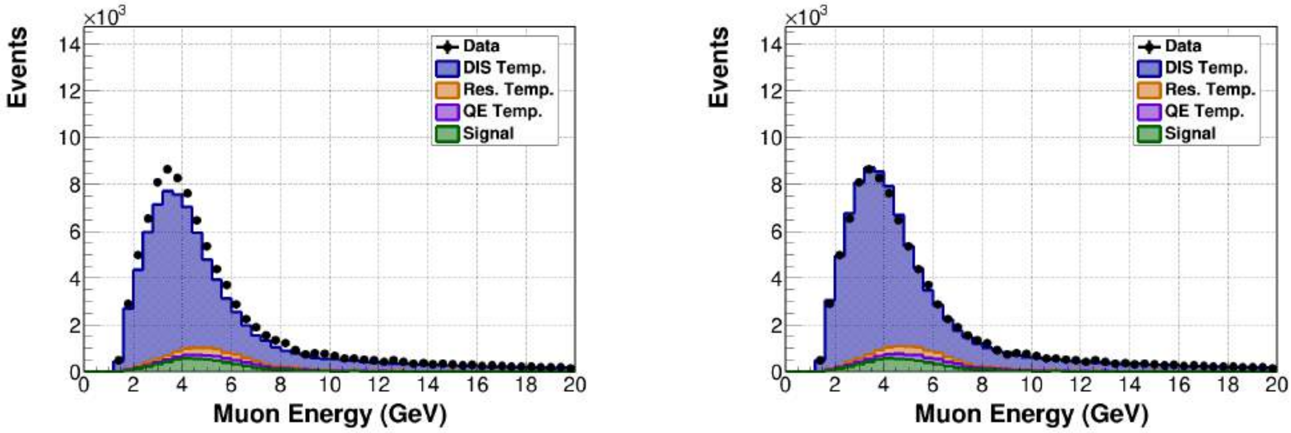

Figure C.9: E_μ distribution in Sideband DIS showing the contributions from the templates. Left: Untuned. Right: Tuned with the p_l scale factors in table 6.1

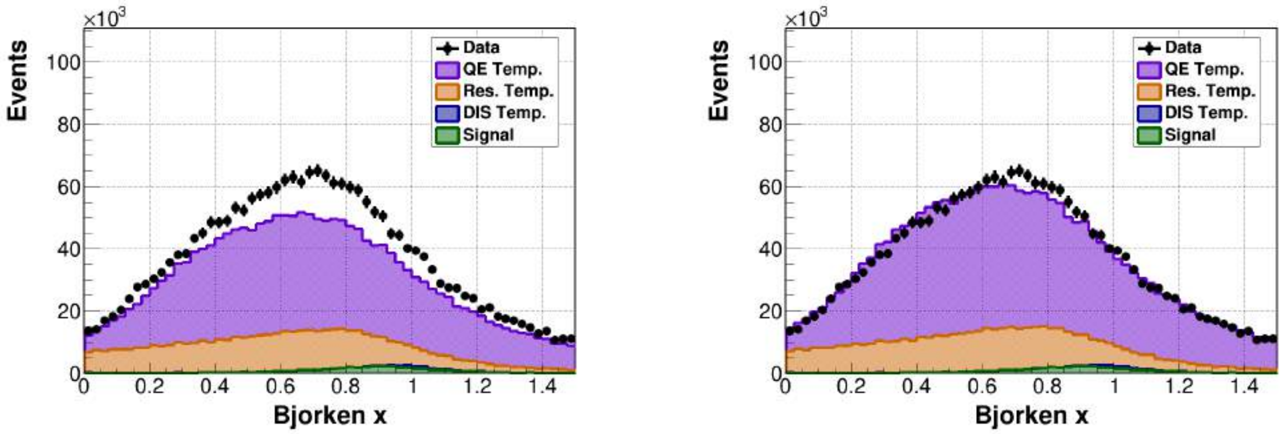

Figure C.10: x_{bj} distribution in Sideband QE showing the contributions from the templates. Left: Untuned. Right: Tuned with the p_l scale factors in table 6.1

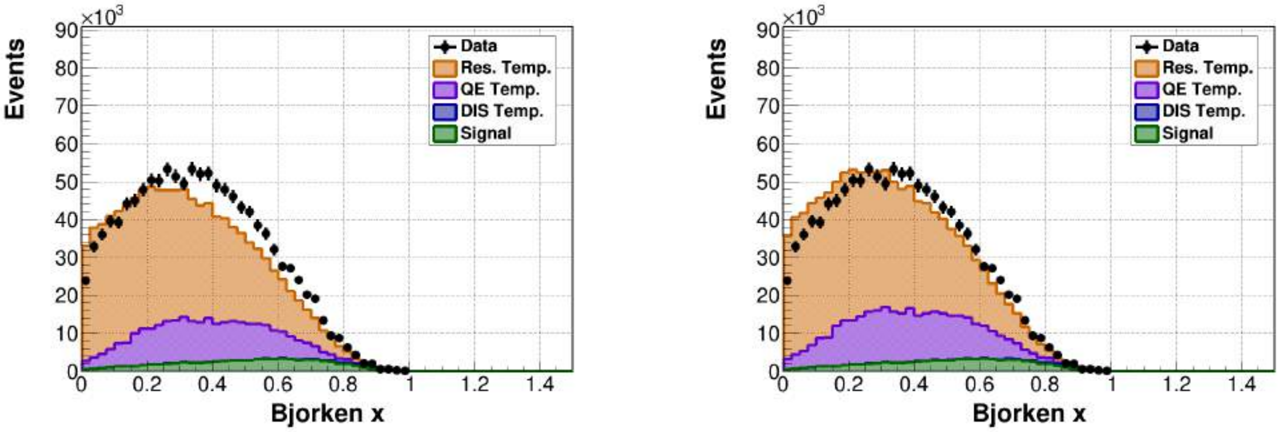

Figure C.11: x_{bj} distribution in Sideband RES showing the contributions from the templates. Left: Untuned. Right: Tuned with the p_l scale factors in table 6.1

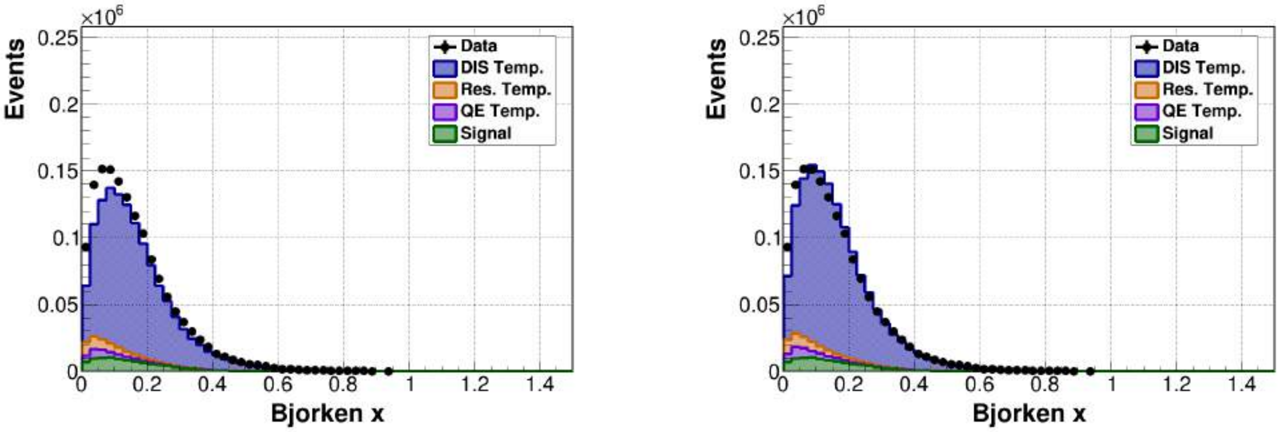

Figure C.12: x_{bj} distribution in Sideband DIS showing the contributions from the templates. Left: Untuned. Right: Tuned with the p_l scale factors in table 6.1

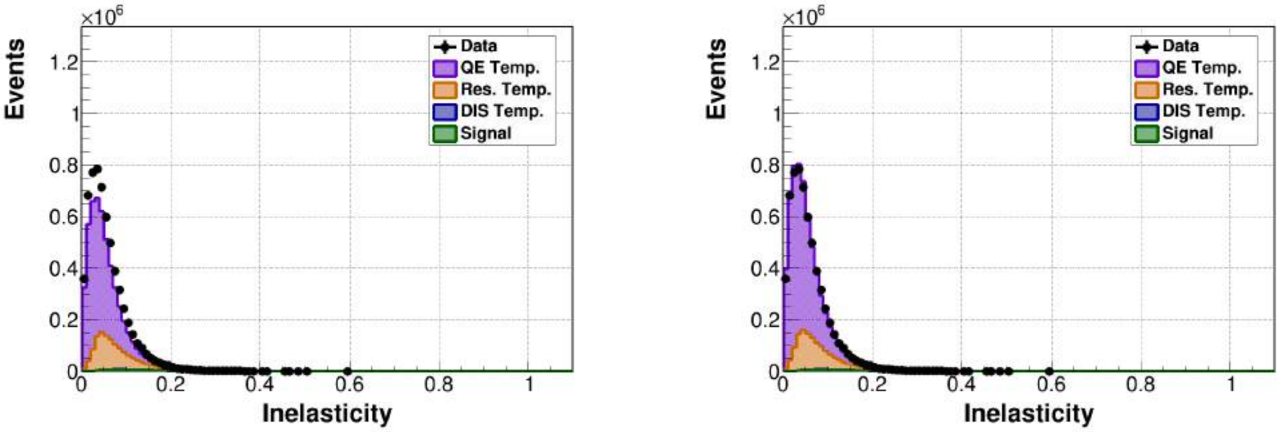

Figure C.13: y distribution in Sideband QE showing the contributions from the templates. Left: Untuned. Right: Tuned with the p_l scale factors in table 6.1

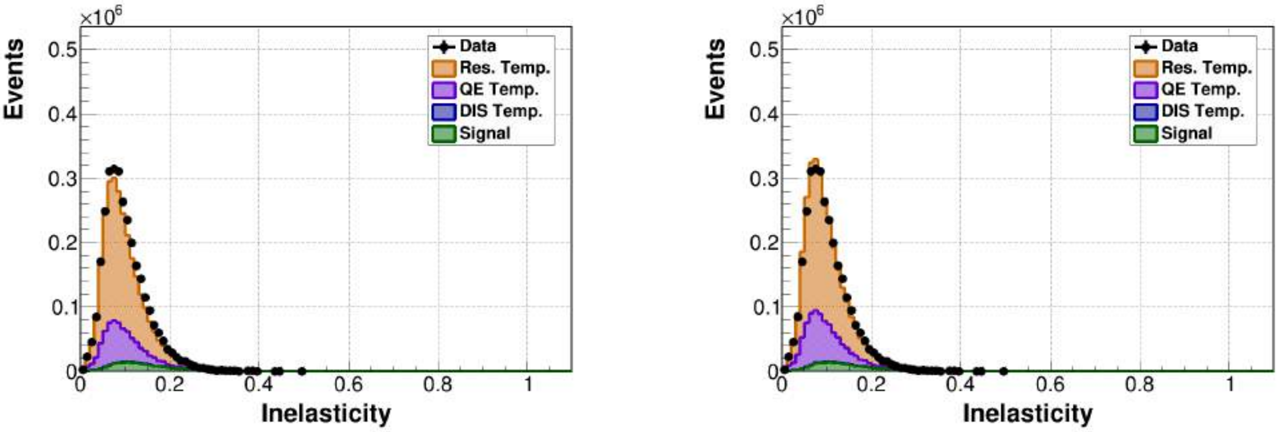

Figure C.14: y distribution in Sideband RES showing the contributions from the templates. Left: Untuned. Right: Tuned with the p_l scale factors in table 6.1

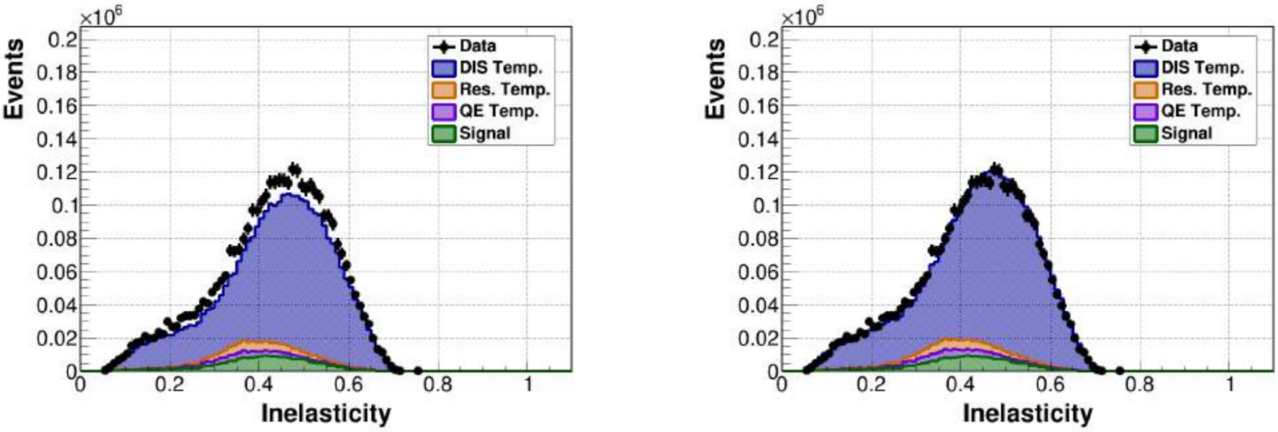

Figure C.15: y distribution in Sideband DIS showing the contributions from the templates. Left: Untuned. Right: Tuned with the p_l scale factors in table 6.1

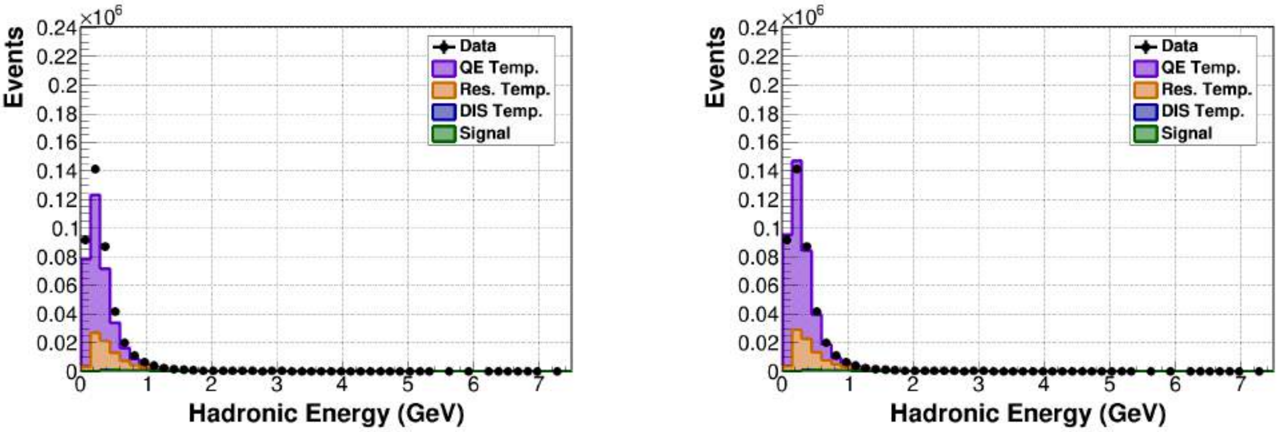

Figure C.16: E_{had} distribution in Sideband QE showing the contributions from the templates. Left: Untuned. Right: Tuned with the p_l scale factors in table 6.1

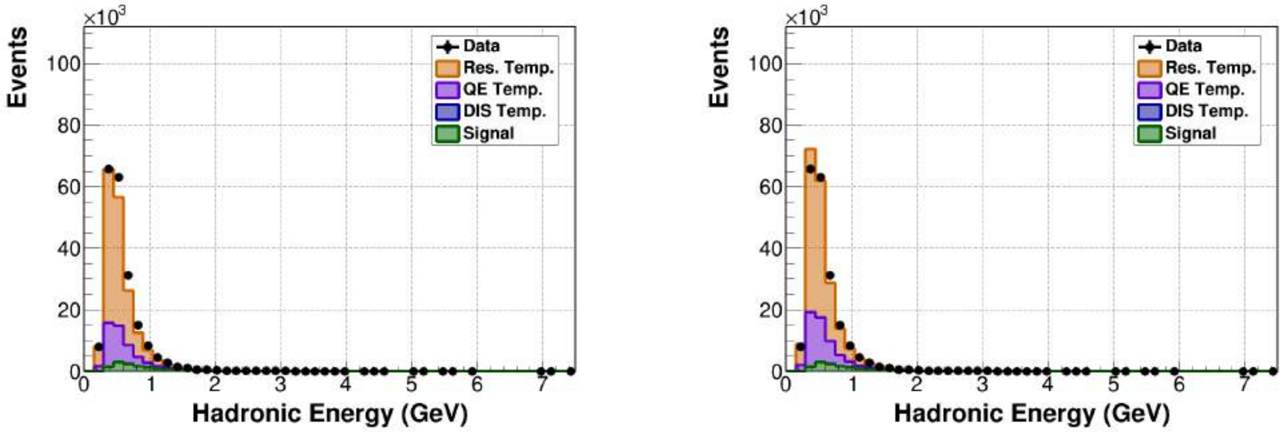

Figure C.17: E_{had} distribution in Sideband RES showing the contributions from the templates. Left: Untuned. Right: Tuned with the p_l scale factors in table 6.1

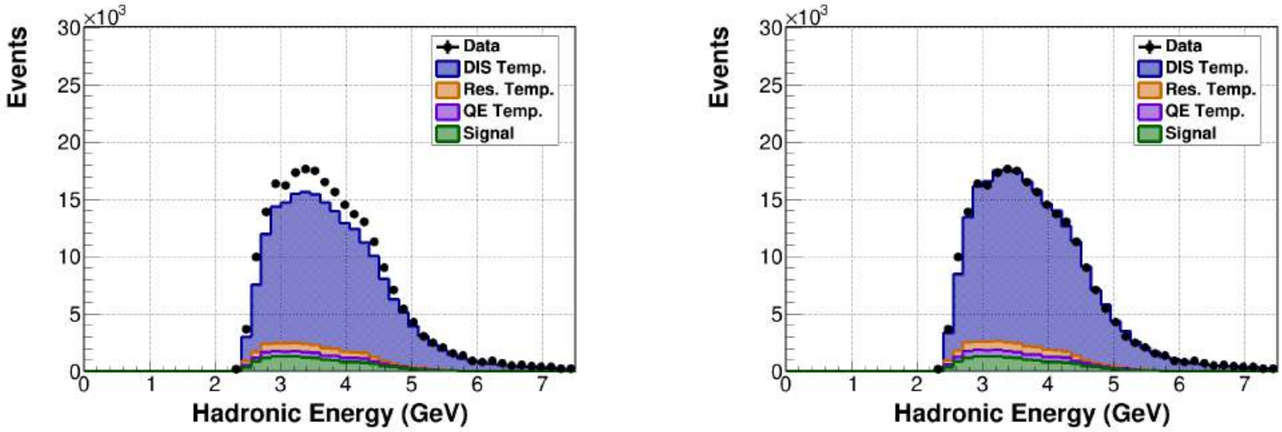

Figure C.18: E_{had} distribution in Sideband DIS showing the contributions from the templates. Left: Untuned. Right: Tuned with the p_l scale factors in table 6.1

Appendix D

Statistical and Systematic Errors in the Sidebands

Statistical and systematic errors of untuned and tuned distributions in the Sidebands are presented.

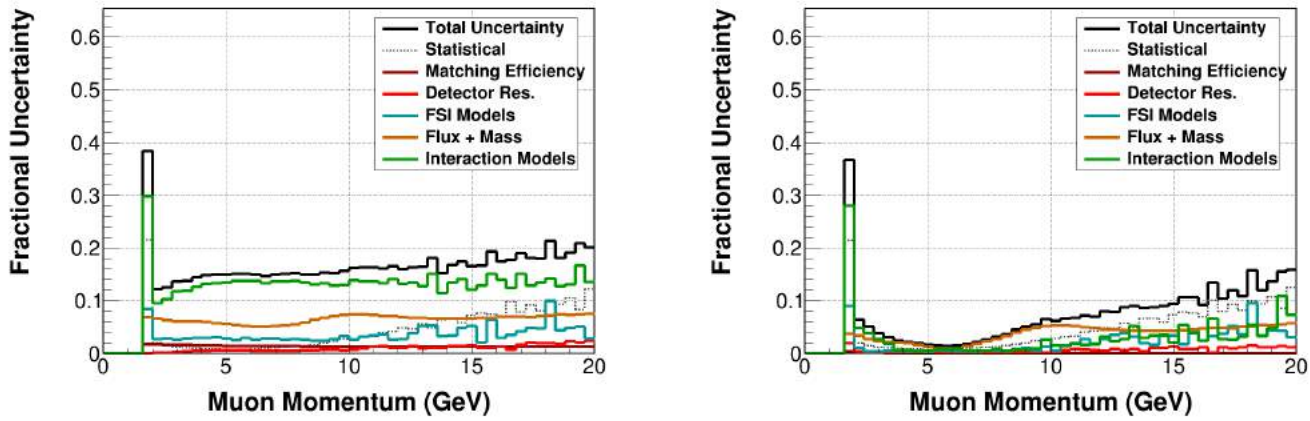

Figure D.1: p distributions in Sideband QE of the statistical and systematic errors. Left: Untuned. Right: Tuned.

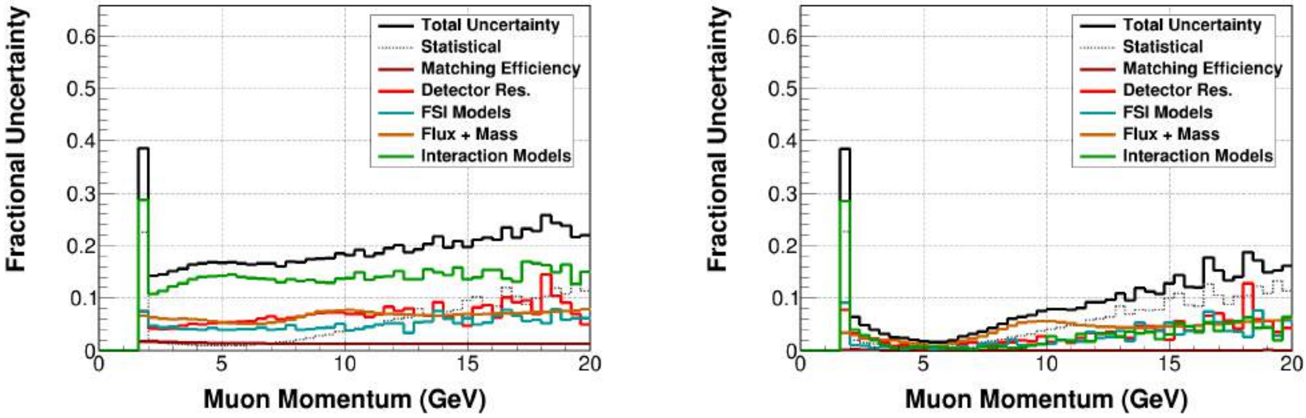

Figure D.2: p distributions in Sideband RES of the statistical and systematic errors. Left: Untuned. Right: Tuned.

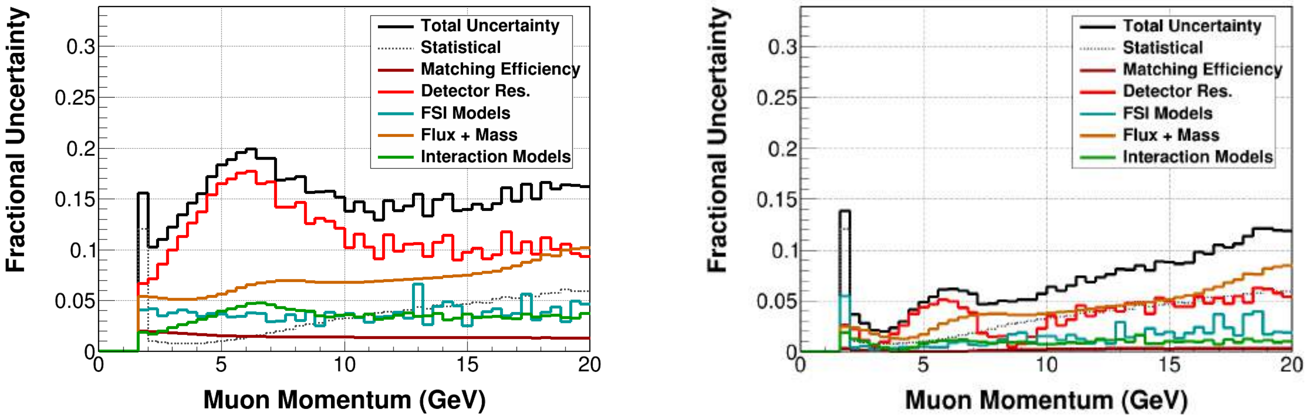

Figure D.3: p distributions in Sideband DIS of the statistical and systematic errors. Left: Untuned. Right: Tuned.

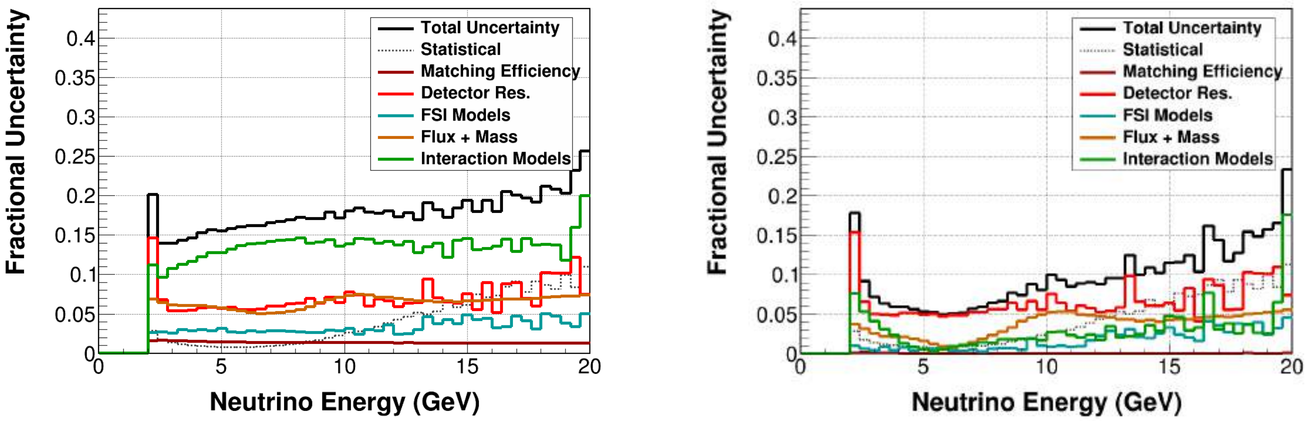

Figure D.4: E_ν distributions in Sideband QE of the statistical and systematic errors. Left: Untuned. Right: Tuned.

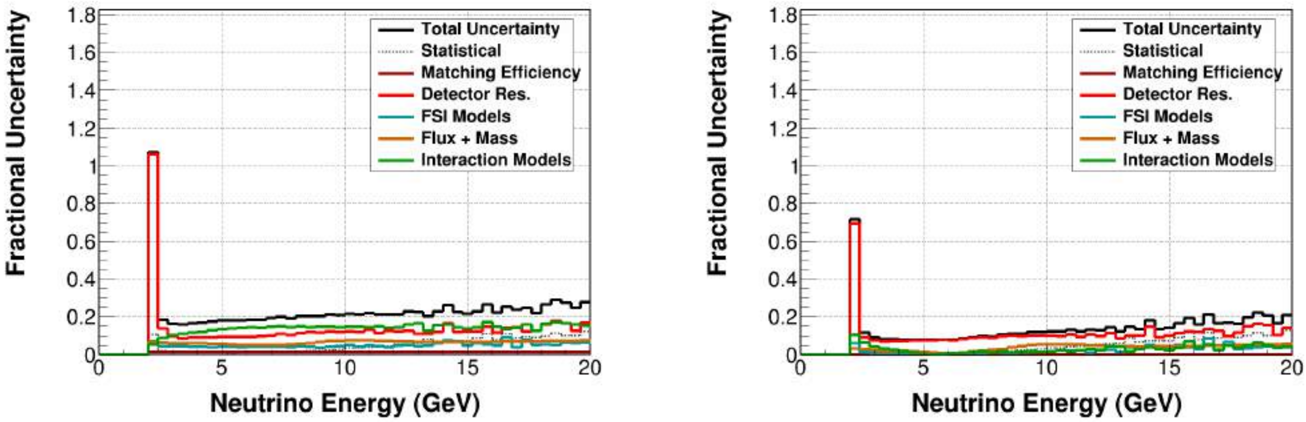

Figure D.5: E_ν distributions in Sideband RES of the statistical and systematic errors. Left: Untuned. Right: Tuned.

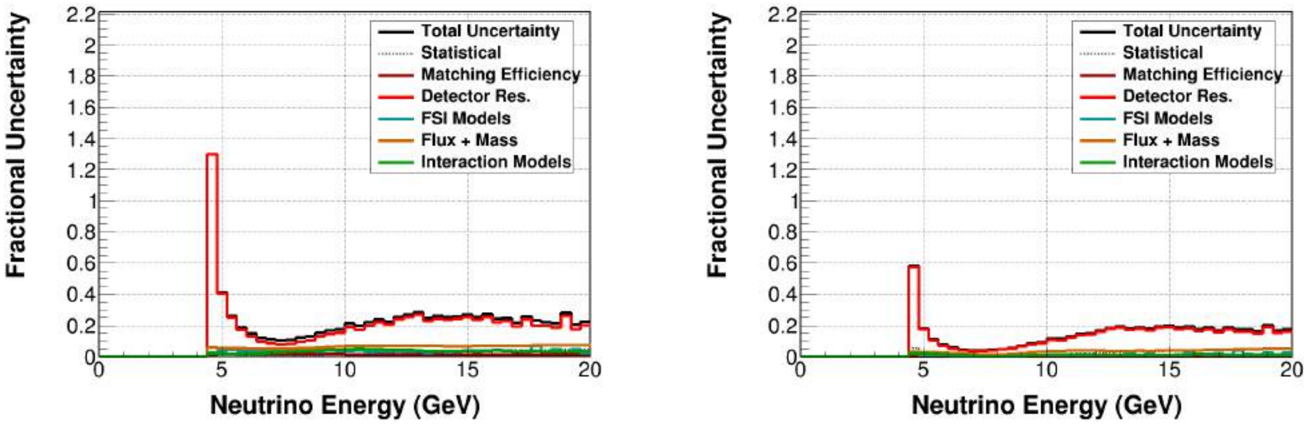

Figure D.6: E_ν distributions in Sideband DIS of the statistical and systematic errors. Left: Untuned. Right: Tuned.

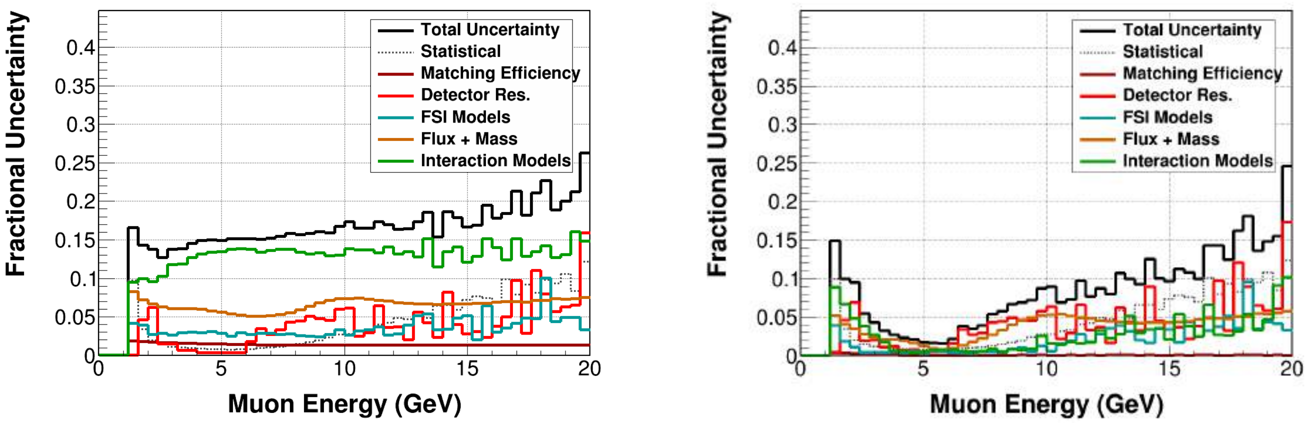

Figure D.7: E_μ distributions in Sideband QE of the statistical and systematic errors. Left: Untuned. Right: Tuned.

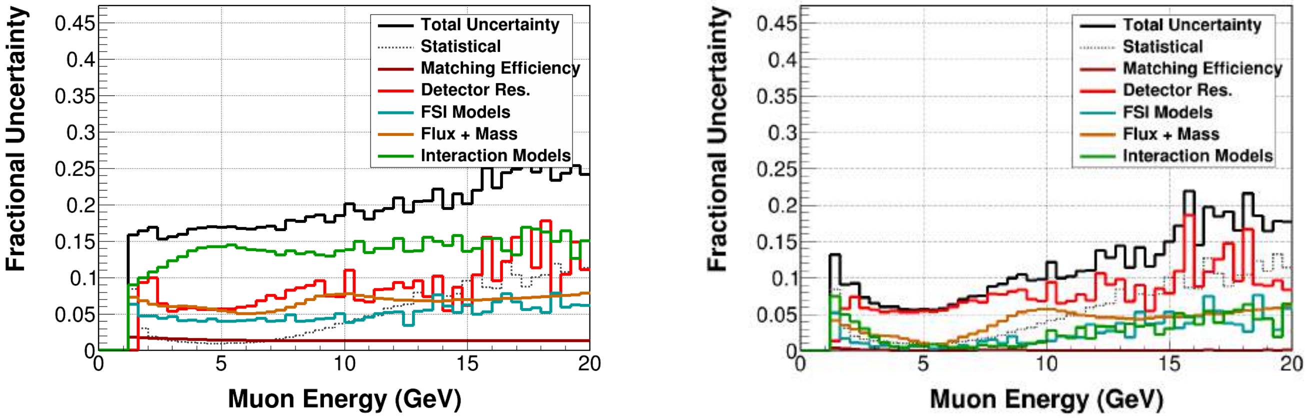

Figure D.8: E_μ distribution in Sideband RES of the statistical and systematic errors. Left: Untuned. Right: Tuned.

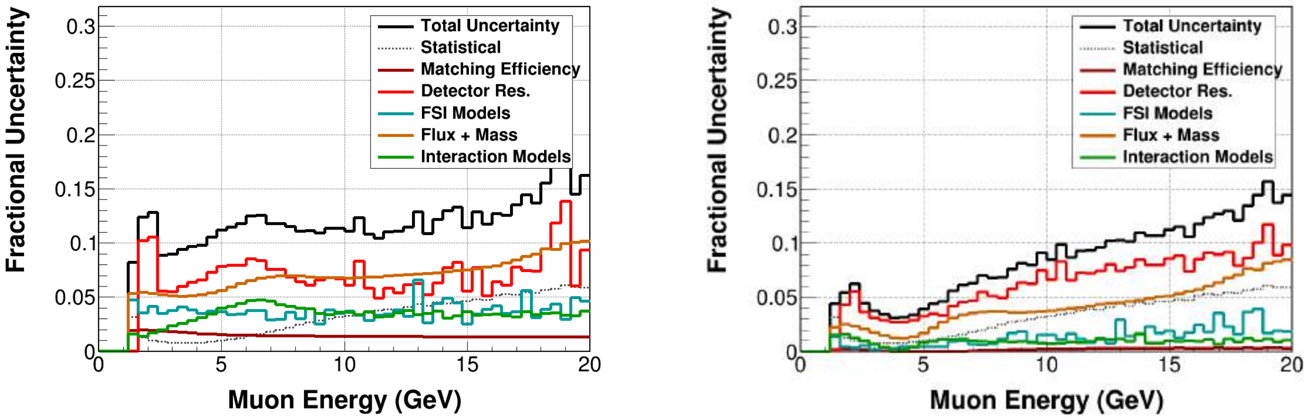

Figure D.9: E_μ distribution in Sideband DIS of the statistical and systematic errors. Left: Untuned. Right: Tuned.

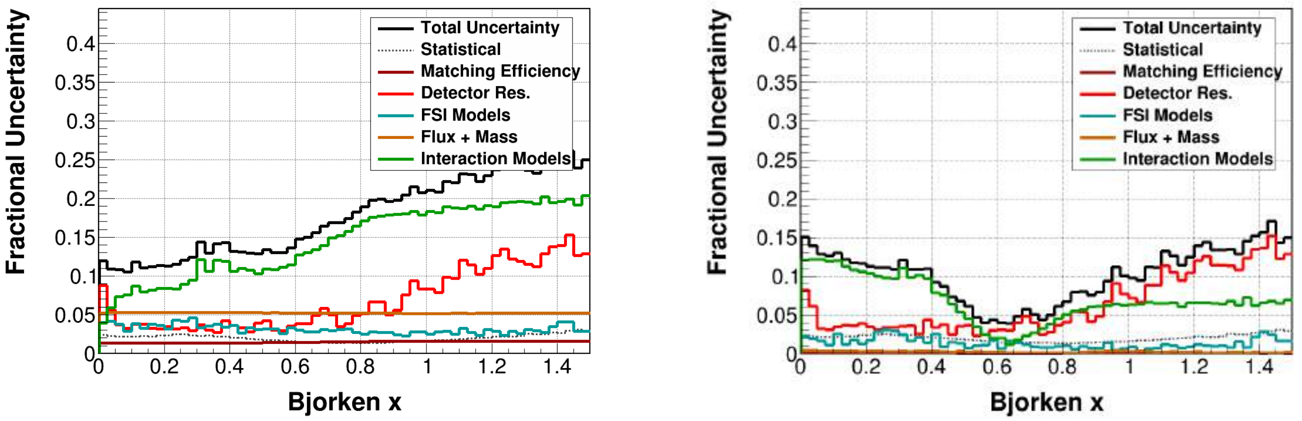

Figure D.10: x_{bj} distributions in Sideband QE of the statistical and systematic errors. Left: Untuned. Right: Tuned.

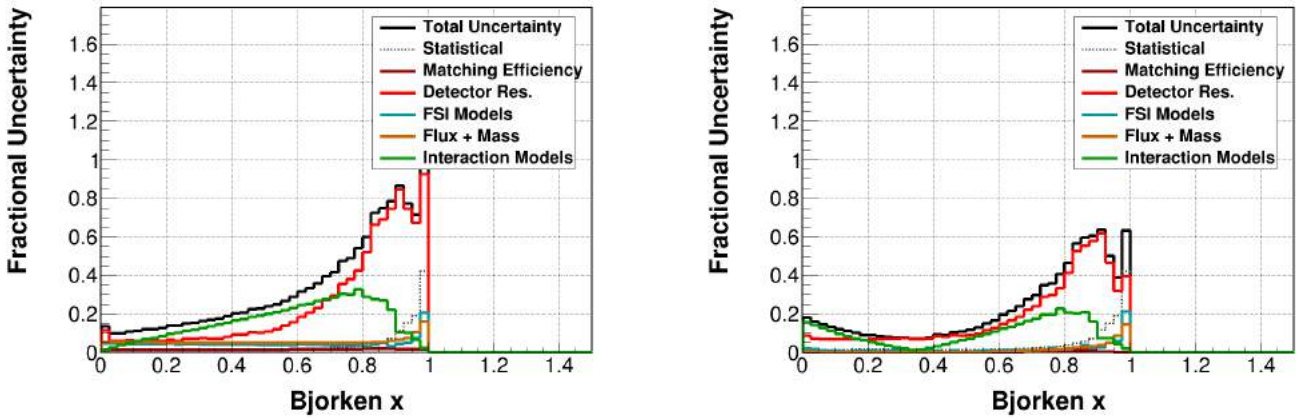

Figure D.11: x_{bj} distributions in Sideband RES of the statistical and systematic errors. Left: Untuned. Right: Tuned.

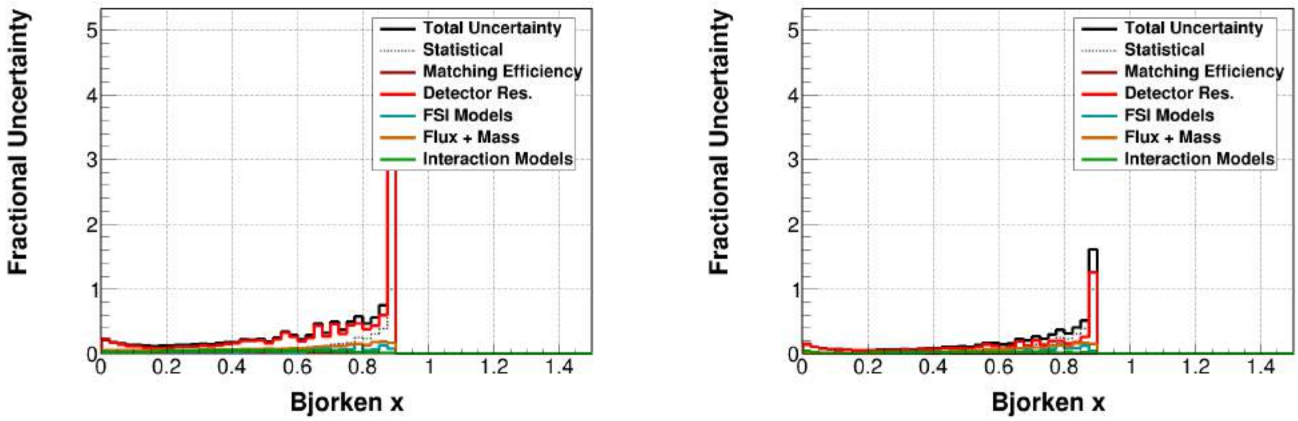

Figure D.12: x_{bj} distributions in Sideband DIS of the statistical and systematic errors. Left: Untuned. Right: Tuned.

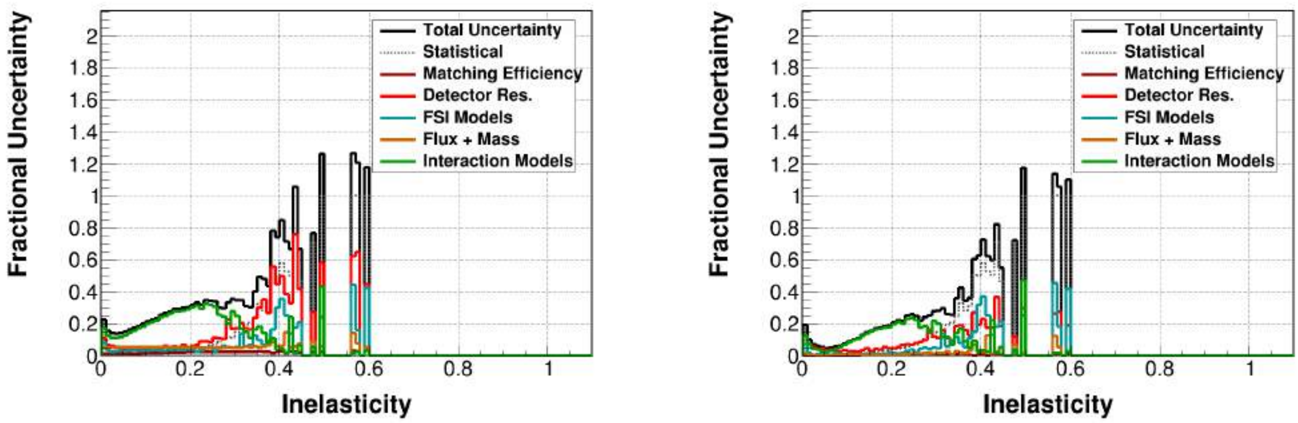

Figure D.13: y distributions in Sideband QE of the statistical and systematic errors. Left: Untuned. Right: Tuned.

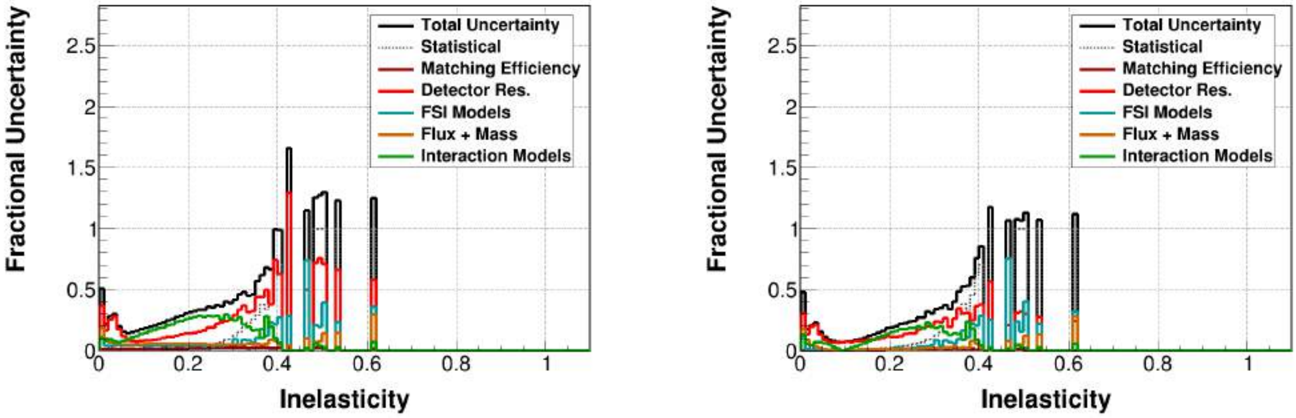

Figure D.14: y distributions in Sideband RES of the statistical and systematic errors. Left: Untuned. Right: Tuned.

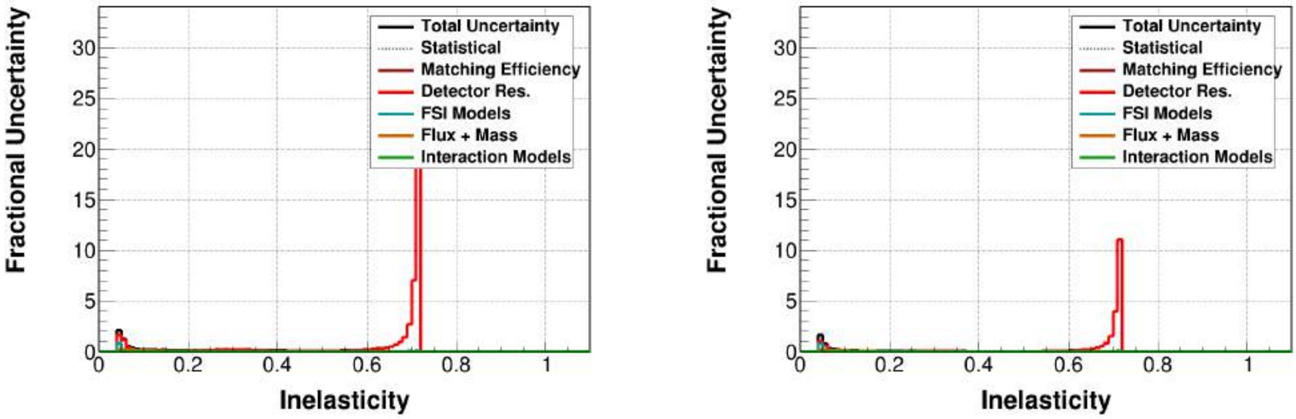

Figure D.15: y distributions in Sideband DIS of the statistical and systematic errors. Left: Untuned. Right: Tuned.

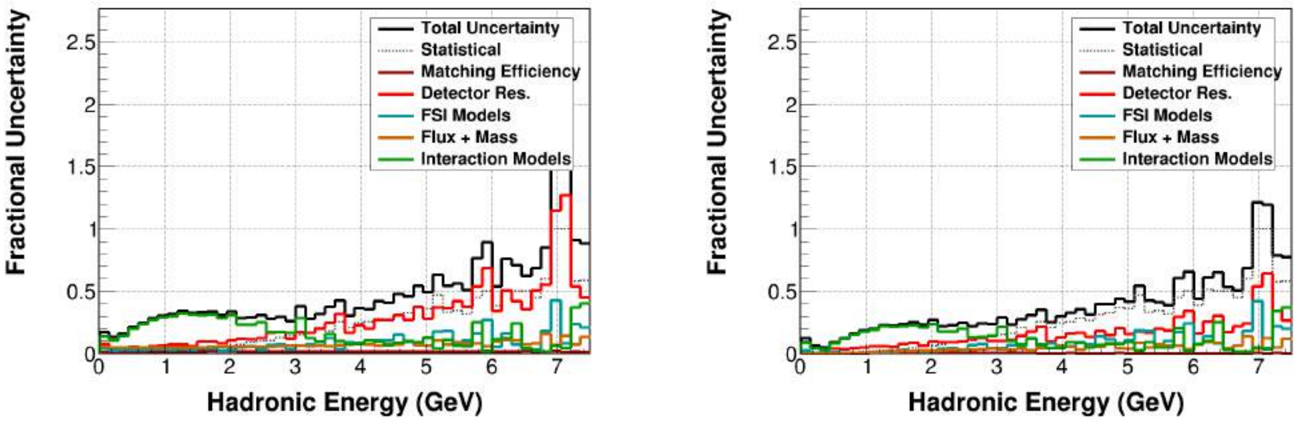

Figure D.16: E_{had} distributions in Sideband QE of the statistical and systematic errors. Left: Untuned. Right: Tuned.

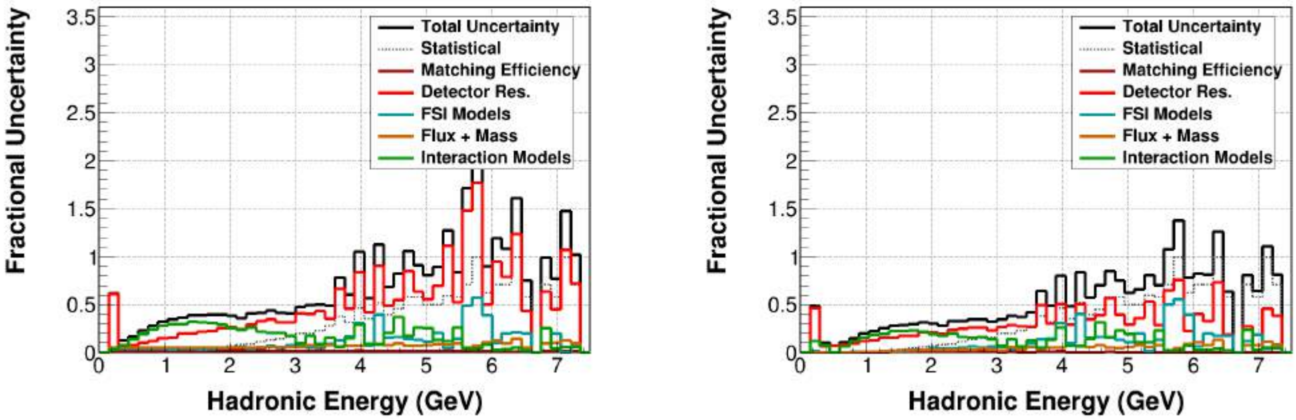

Figure D.17: E_{had} distributions in Sideband RES of the statistical and systematic errors. Left: Untuned. Right: Tuned.

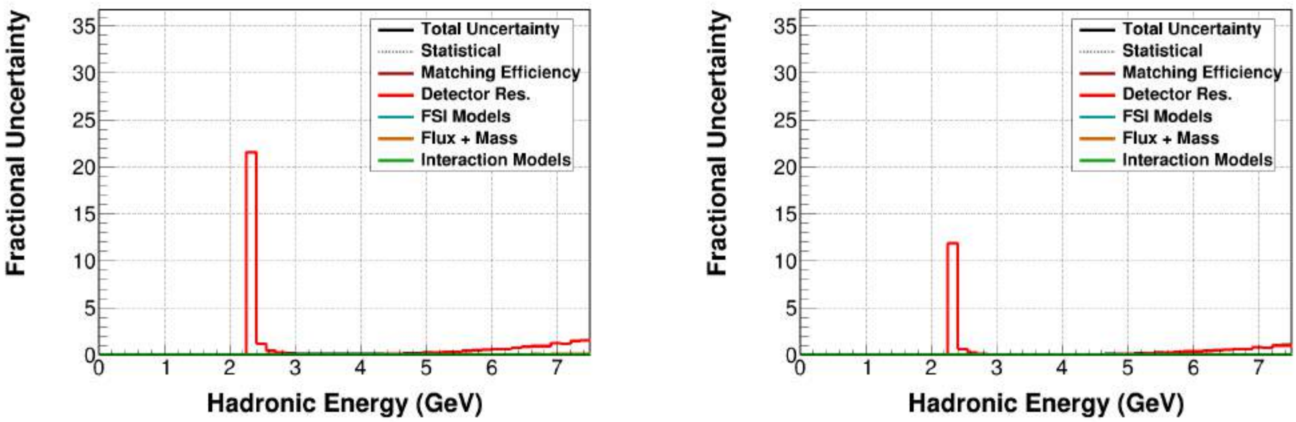

Figure D.18: E_{had} distributions in Sideband DIS of the statistical and systematic errors. Left: Untuned. Right: Tuned.

Appendix E

Migration Matrices

Row normalized Migration matrices for kinematic variables are presented.

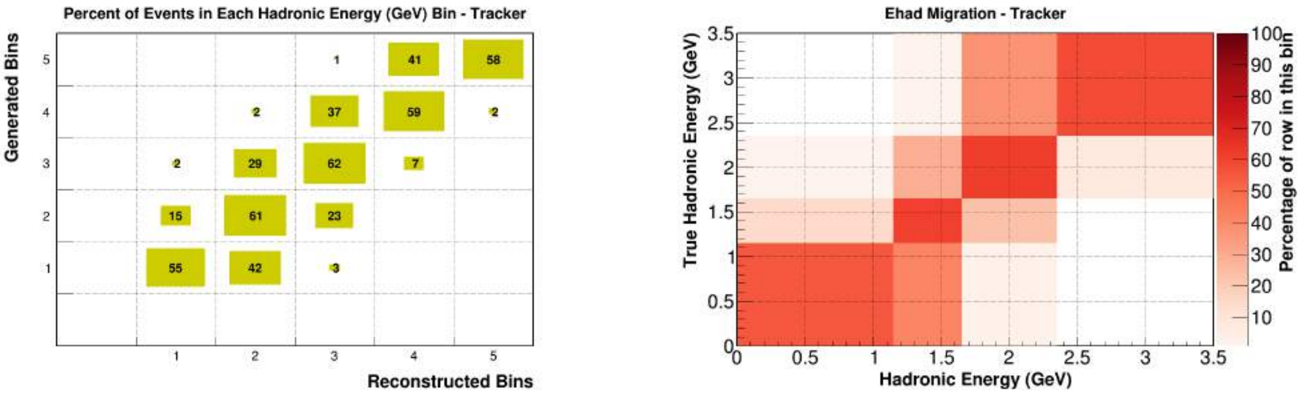

Figure E.1: Migration matrix for E_{had}: purity percentages (left) and bin widths (right)

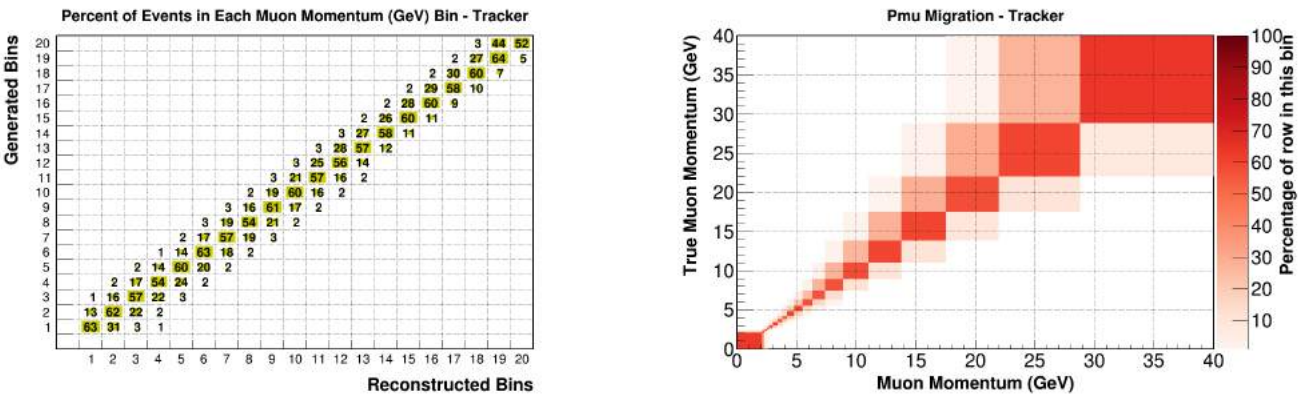

Figure E.2: Migration matrix for p: purity percentages (left) and bin widths (right)

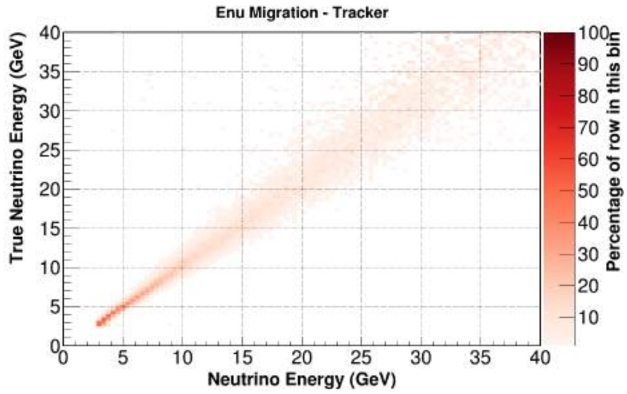

Figure E.3: Migration matrix for E_ν bin widths

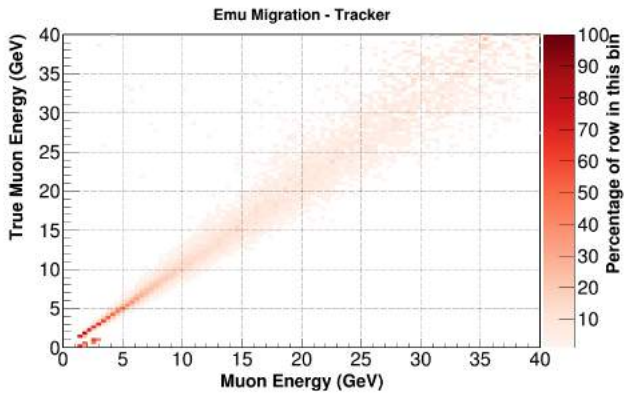

Figure E.4: Migration matrix for E_μ bin widths

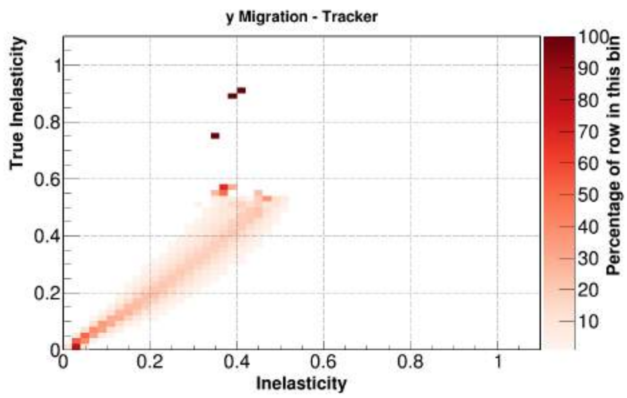

Figure E.5: Migration matrix for y bin widths

Appendix F

Background subtracted sample and Unfolded distributions

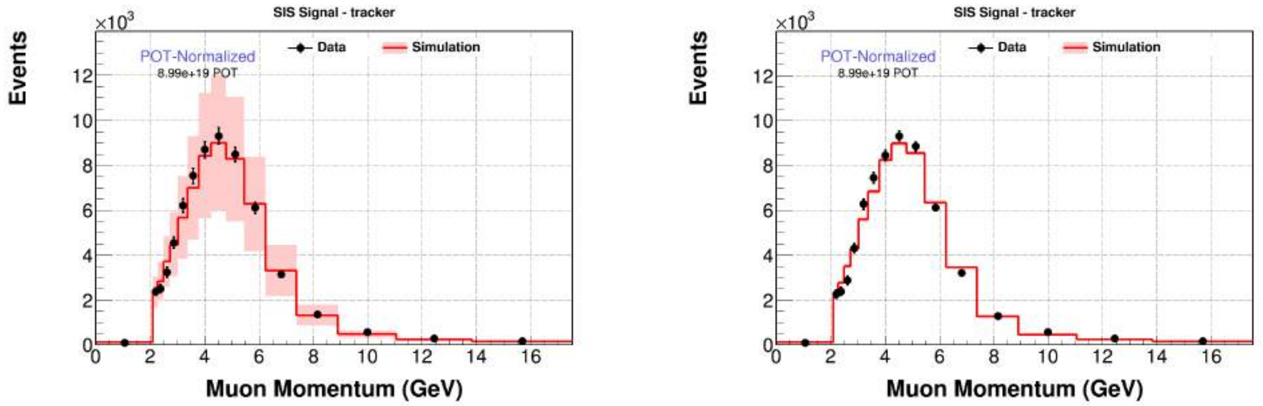

Figure F.1: SIS events in CH per reconstructed p (left) and unfolded (right)

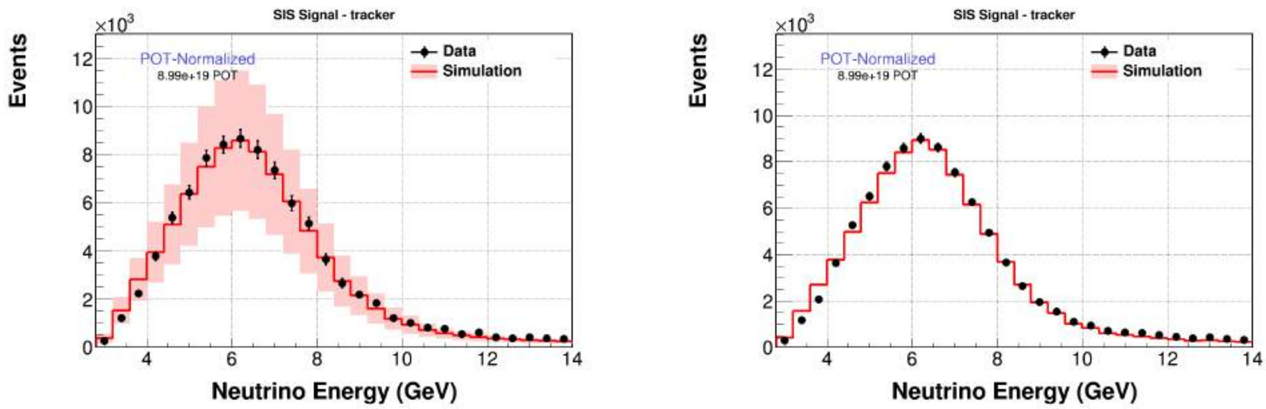

Figure F.2: SIS events in CH per reconstructed E_ν (left) and unfolded (right)

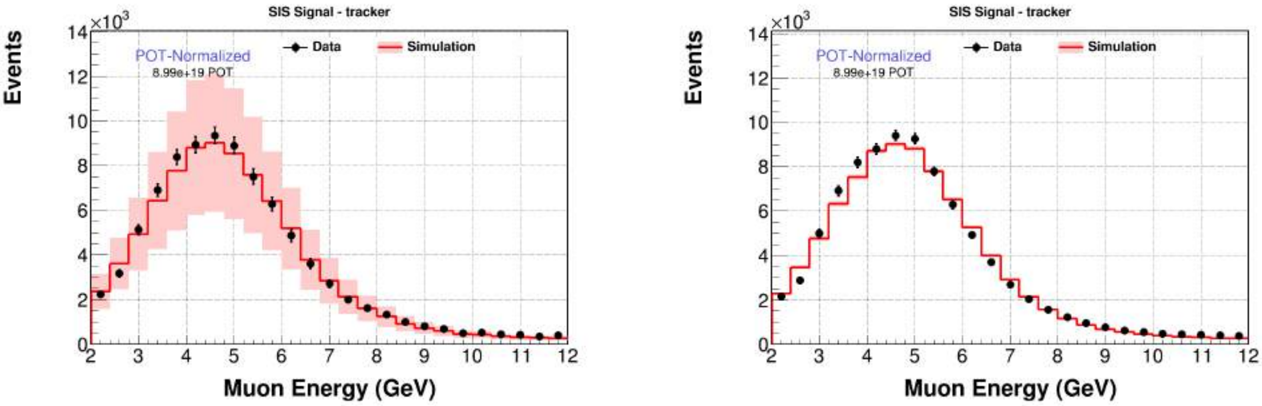

Figure F.3: SIS events in CH per reconstructed E_μ (left) and unfolded (right)

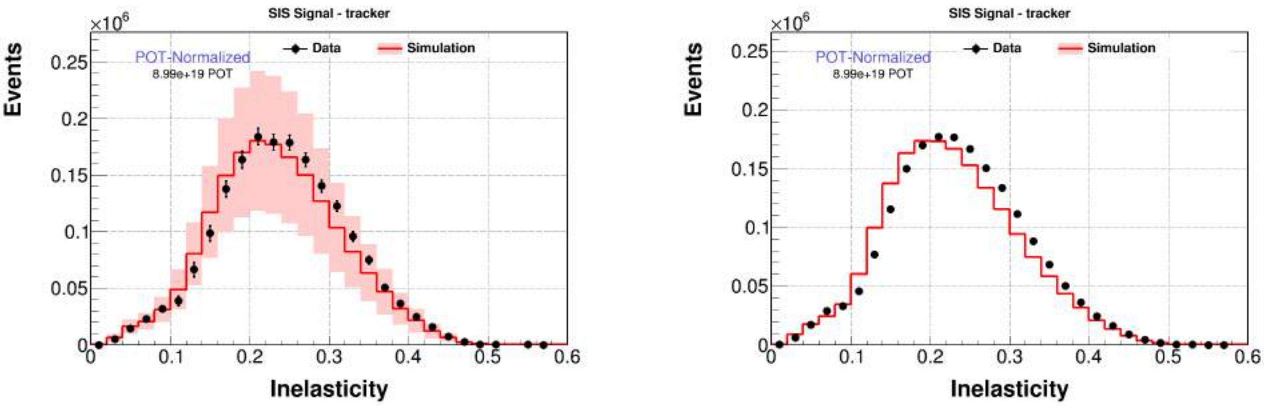

Figure F.4: SIS events in CH per reconstructed y (left) and unfolded (right)

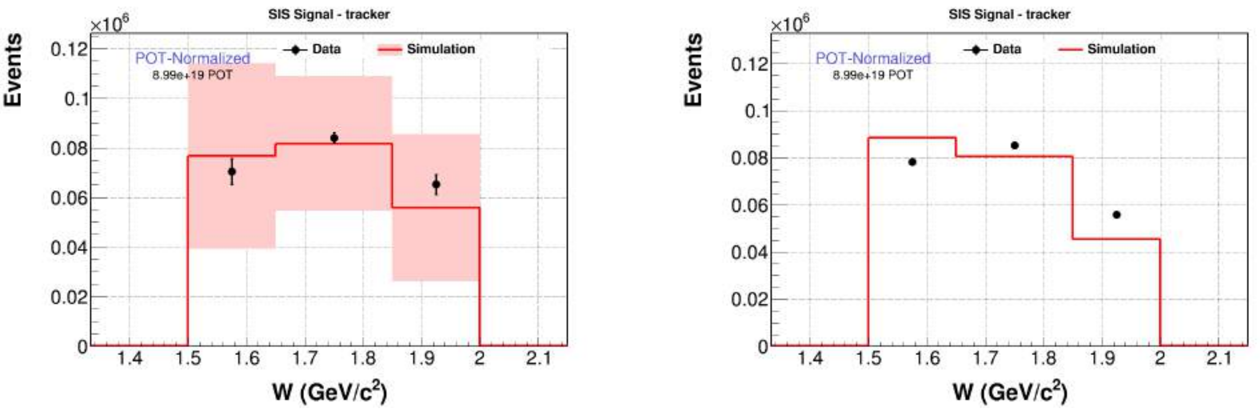

Figure F.5: SIS events in CH per reconstructed W (left) and unfolded (right)

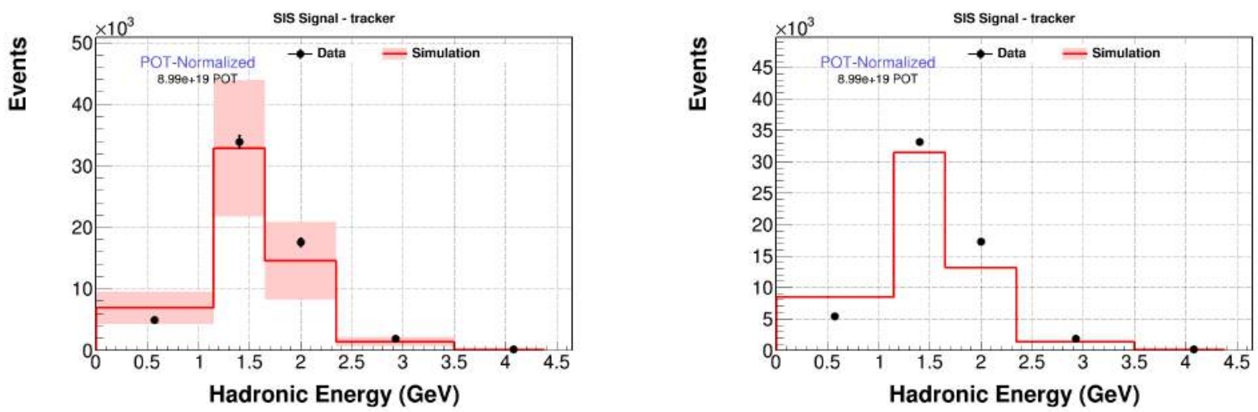

Figure F.6: SIS events in CH per reconstructed E_{had} (left) and unfolded (right)

Appendix G

Efficiency distributions

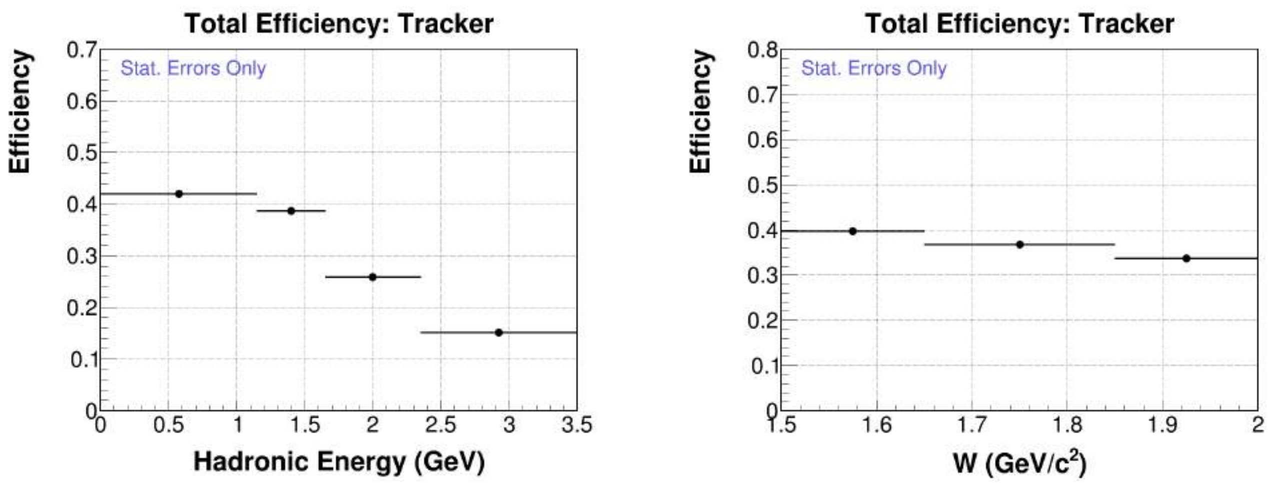

Figure G.1: Efficiency of events in the tracker region (CH) as a function of Hadronic energy (left) and hadronic invariant mass (right).

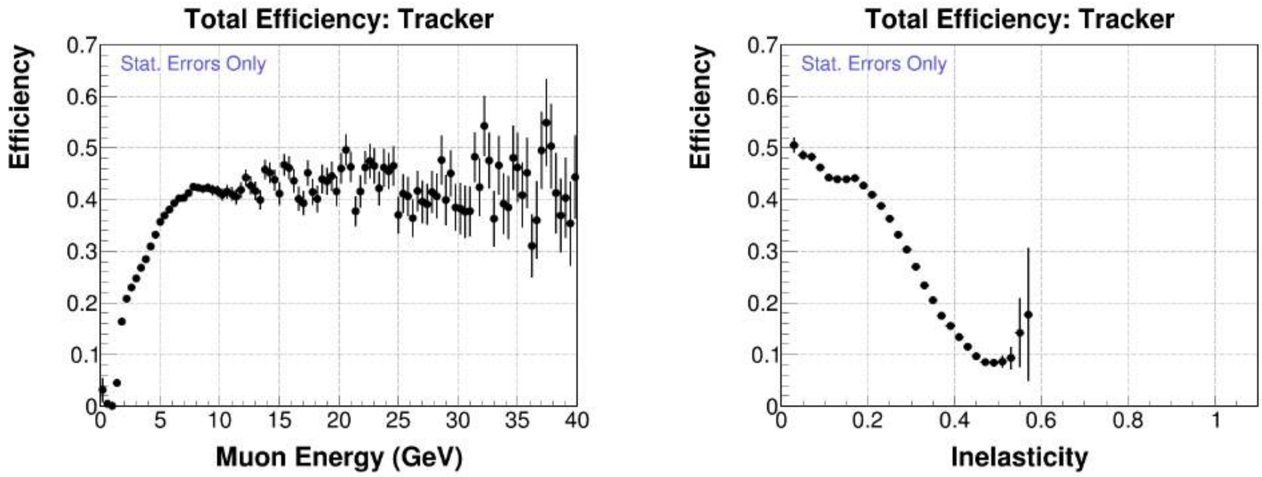

Figure G.2: Efficiency of events in the tracker region (CH) as a function of muon energy (left) and inelasticity (right).

Appendix H

Summary of the Contributions to the MINERνA experiment

This section briefly lists all contributions made to the MINERνA experiment.

H.1 Medium Energy Data Calibration

The medium energy data taken from September 2nd,2017 to February 26th,2019 was calibrated (figure 4.3). The stages I was involved in are the gains and strip to strip calibrations.

H.1.1 Gains calibration

The goal of the gains calibrations is to measure fluctuations in the photomultiplier's production of charge per incoming photoelectron [76]. This is done by injecting a constant amount of light into the PMT using a light injection system (LI). PMT's gains are affected by hardware swaps, detector shutdowns or restarts and NuMI beam shutdowns. Besides running the calibration the knowledge of time and date of any of these actions was crucial to undertand PMT's sudden gain fluctuations.

H.1.2 Strip to Strip calibration

The goal of this calibration is to make the response of the detector uniform by correcting the light levels between scintillator strips [76]. Muons produced by neutrino interactions in the rock (rock muons) are used to probe all scintillators strips. The path length-normalized peak energy deposit by the throughgoing rock muons is used to extract the multiplicative constants. This calibration gives also information about dead channels as can be seen in the figure H.1 which shows the calibration constants for a set of data calibrated.

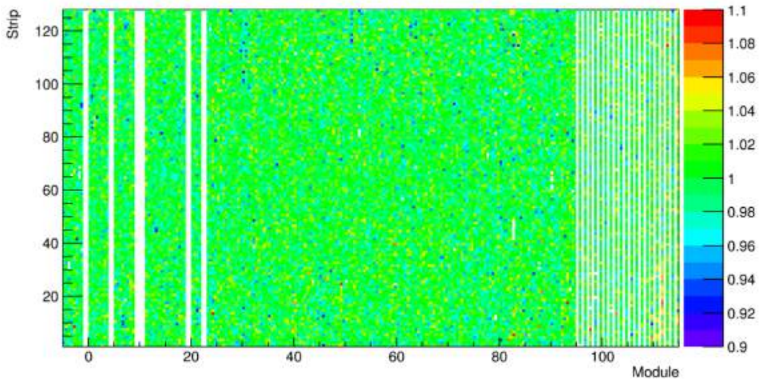

Figure H.1: Strip to strip calibrations factors for a set of data. Calibrations factors for each strip in each module are shown. In this calibration also the death channels can be identified (blank spaces).

H.2 nCTEQ and GENIE DIS Cross Sections Comparison

GENIE uses old Parton Distribution Functions named GRV98 [60] to simulate a cross section. I tested GENIE predictions with calculations made using modern Nuclear and Nucleon Parton Distribution Functions (PDFs) provided by the CTEQ collaboration. nCTEQ15 refers to a set of cross sections that uses charged lepton-nucleus data to extract Nuclear PDFs [92] and nCTEQnu refers to a set of cross sections that uses neutrino-nucleus data to extract Nuclear PDFs [92]. Weights were calculated for the DIS region and GENIE weighted simulation were already used in the double-differential inclusive charged-current ν_μ cross sections publication in 2020 [93]. They will also be used to be compared to the DIS cross section being developed in the MINERνA detector. The dicrepancy of the cross sections as a function of E_ν for events in Iron can be seen in figure H.2.

H.3 Data taking Shifts

All the collaborators of the MINERνA experiment took shifts during the detector lifetime. I had the opportunity to take shifts when I was developing my master's analysis (2015-2016) and my Phd. analysis (2016-2020). MINERνA experiment stop taking data on February 2019.

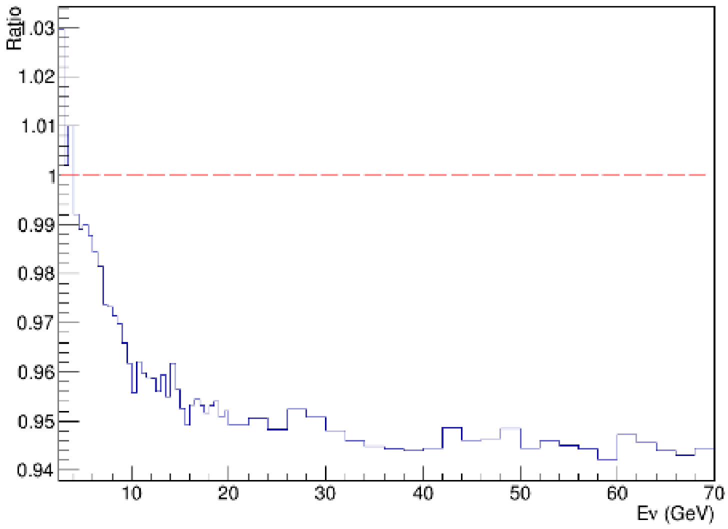

Figure H.2: Ratio of the nCTEQ15 to GENIE Total Cross sections as a function of the Neutrino energy in Iron.

Bibliography

[1] Von Bayer, O. Hahn, L. Meitner, Phys. Zeitschrift, 12, January, 1911, p. 378.

[2] C.D. Ellis, B.A. Wooster, The average energy of desintegration of Radium E,Proc. Roy. Soc. A117(1927) 109-123.

[3] W. Pauli, Letter sent to Tubingen conference, Dec. 1930.

[4] J. Chadwick, F. (1932) Proc. Roy. Soc., A 136, 692708.

[5] Fred L. Wilson, Fermi's Theory of Beta Decay (English translation), American Journal of Physics volume 36, number 12, pagina 1150.

[6] Reines, F. and Cowan, C. L. Nov, (1953), "Detection of the Free Neutrino", Phys. Rev. 92, 830.

[7] C. L. Cowan, F. Reines, F. B. Harrison, H. W. Kruse, A. D. McGuire, (1956), "Detection of a Free Neutrino: a Confirmation", Science Vol 124 , Number 3212.

[8] F. Reines and C.L. Cowan,(1956), "The Neutrino", Nature 178, 446-449.

[9] M. Goldhaber, L. Grodzins, and A.W. Sunyar,(1957), Helicity of neutrinos, Phys. Rev. 109 1015.

[10] R. Davis, (1955),"Attempt to Detect the Antineutrinos from a Nuclear Reactor by the $\mathrm{Cl}^{37}(\overline{\nu}, e^-)\mathrm{A}^{37}$ Reaction" Phys. Rev. 97, 766.

[11] C.S. Wu et al., Phys. Rev. 105 (1957)1413

[12] Danby, G., Gaillard, J.-M., Goulianos, K., Lederman, L. M., Mistry, N.,Schwartz, M., and Steinberger, J. July 1962 Physical Review Letters 9, 3644.

[13] Gargamelle Neutrino Collaboration: F.J. Hasert et al., Observation of neutrino-like interactions without muon or electron in the Gargamelle neutrino experiment, Phys. Lett. B 46 (1973)138.

[14] R. Davis,D.S. Harner, and K.C. Hoffman, Search for neutrinos from the sun, Phys. Rev. Lett. 20 (1968)1205.

[15] Hirata, K.S., Kajita, T., Koshiba, M., Nakahata, M., Ohara, S., Oyama, Y. et al. (1988) Experimental study of the atmospheric neutrino fux. Phys.Lett. B 205, 416-420.

[16] V.N. Gribov and B. Pontecorvo, Phys. Lett B 28(1969)493.

[17] DONUT Collaboration (2001) Phys. Lett. B504, 218224.

[18] Haines, T.J., Bionta, R.M., Blewitt, G., Bratton, C.B., Casper, D., Claus, R. et al. (1986) Calculation of atmospheric neutrino-induced backgrounds in a nucleon-decay search. Phys. Rev. Lett. 57, 1986-1989.

[19] Nakahata, M., Arisaka, K., Kajita, T., Koshiba, M., Oyama, Y., Suzuki, A. et al. (1986) Atmospheric neutrino background and pion nuclear effect for KAMIOKA nucleon decay experiment. J. Phys. Soc. Jpn. 55, 3786-3805.

[20] ALEPH Collaboration:D. Decamp et al., ”Determination of the Number of Light Neutrino Species”, Phys. Lett. B 231(1989)519.

[21] Delphi Collaboration:P.A. Aarnio et al.,”Measurement of the Mass and Width of the Z^0 Paricle from Multi-Hadronic Final States Produced in the e^+ e^- Annihilation”, Phys. Lett. B 231 (1989)539.

[22] L3 Collaboration:B. Adeva et al.,”A Determination of the Properties of the Neutral Intermediate Vector Boson Z^0”, phys. Lett. B 231 (1989)509.

[23] OPAL Collaboration:M.Z. Akrawy et al.,”Measurement of the Z^0 Mass and Width with the OPAL Detector at LEP”, Phys. Lett. B bf 231 (1989)530.

[24] C. Patrignani et al. (Particle Data Group), Chinese Physics C, 40, 100001 (2016).

[25] E.Kh. Akhmedov, G. C. Branco, M. N. Rebelo, 1999, ”Seesaw mechanism and structure of neutrino mass matrix”, arXiv:hep-ph/9911364

[26] Francis Halzen, Alan D. Martin, ”Quarks and Leptons. Introductory Course in Modern Particle Physics”, John Wiley and Sons.

[27] J. A. Formaggio, G. P. Zeller, (2012), From eV to EeV: Neutrino cross sections across energy scales, Rev. Mod. Phys.: Volume 84.1307 .

[28] D.Casper (2002), The NUANCE Neutrino Simulation, and the Future, arXiv:hep-ph/0208030v1.

[29] B.T. Cleveland et al. Astrophys. J 496 , 505 (1998).

[30] Bahcall J N and Pena-Garay C 2004 New J. Phys.6 63.

[31] Q. R. Ahmad et al. (SNO Collaboration), Measurement of the Rate of Interactions Produced by ^{8}B Solar Neutrinos at the Sudbury Neutrino Observatory, Phys. Rev. Lett. 87, 071301 (2001).

[32] Q. R. Ahmad et al. (SNO Collaboration), Direct Evidence for Neutrino Flavor Transformation from Neutral-Current Interactions in the Sudbury Neutrino Observatory, Phys. Rev. Lett. 89, 011301 (2002).

[33] J. Hosaka et al., Solar neutrino measurements in Super-Kamiokande-I, Phys. Rev., D73, 112001 (2006), hep-ex/0508053.

[34] J. N. Bahcall, A. M. Serenelli and S. Basu, New solar opacities, abundances, helioseismology, and neutrino fluxes, Astrophys. J., 621, L85–L88 (2005).

[35] K. Eguchi et al.(2003) (KamLAND Collaboration) First Results from KamLAND: Evidence for Reactor Anti-Neut rino Disappearance , Phys. Rev. Lett. 90, 021802.

[36] F. Suekane et al., An Overview of the KamLAND 1-kiloton Liquid Scintillator, arXiv:physics/0404071.

[37] Abe et al. (The KamLAND Collaboration)2008(), Precision Measurement of Neutrino Oscillation Parameters with KamLANDS., Phys. Rev. Lett. 100, 221803.

[38] Apollonio, M. et al. Limits on neutrino oscillations from the CHOOZ experiment. Phys. Lett. B 466, 415–430 (1999).

[39] Boehm, F. et al. Search for neutrino oscillations at the Palo Verde nuclear reactors. Phys. Rev. Lett. 84, 3764–3767 (2000).

[40] Abe, Y. et al. Indication of reactor electron-antineutrino disappearance in the Double Chooz experiment. Phys. Rev. Lett. 108, 131801 (2012).

[41] Abe, Y. et al. Background-independent measurement of θ_{13} in Double Chooz. Phys. Lett. B 735, 51–56 (2014).

[42] Ahn, J. K. et al. Observation of reactor electron antineutrino disappearance in the RENO experiment. Phys. Rev. Lett. 108, 191802 (2012).

[43] An, F. P. et al. Observation of electron-antineutrino disappearance at Daya Bay. Phys. Rev. Lett. 108, 171803 (2012).

[44] An, F. P. et al. Spectral measurement of electron antineutrino oscillation amplitude and frequency at Daya Bay. Phys. Rev. Lett. 112, 061801 (2014). Determination of the mixing angle h 13 and observation of the associated oscillations at the Daya-Bay reactor experiment.

[45] T. K. Gaisser, M. Honda, (2002), Flux of Atmospheric Neutrinos, arXiv:hep-hp/0203272v2.

[46] Y. Fukuda et al. (Super-Kamiokande Collaboration) (1998), "Evidence for Oscillation of Atmospheric Neutrinos", Phys. Rev. Lett. 81, 1562

[47] T. Kafka, talk presented at 5th International Workshop on Topics in Astroparticle and Underground Physics (TAUP 97), Gran Sasso, Italy, 7–11 Sep 1997, hep-ph/9712281; E. Peterson, talk presented at The XVIIIth International Conference on Neutrino Physics and Astrophysics (NEUTRINO'98), Takayama, Japan, 4–9 June, 1998; H. Gallagher, parallel session talk presented at The 29th International Conference on High-Energy Physics (ICHEP 98), 23–29 Jul 1998, Vancouver, Canada.

[48] Allison, W.W.M., Alner, G.J., Ayres, D.S., Barr, G., Barrett, W.L., Bode, C. et al.(Soudan-2 collaboration) (1999) The atmospheric neutrino flavor ratio from a 3.9 fiducial kiloton-year exposure of Soudan 2. Phys. Lett. B 449, 137-144.

[49] Ambrosio, M., Antolini, R., Aramo, C., Auriemma, G., Baldini, A., Barbarino, G.C. et al. (MACRO collaboration) (1998) Measurement of the atmospheric neutrino-induced upgoing muon flux using MACRO. Phys. Lett. B 434, 451-457.

[50] Ambrosio, M., Antolini, R., Auriemma, G., Bakari, D., Baldini, A., Barbarino, G.C. et al.(MACRO collaboration) (2000) Low energy atmospheric muon neutrinos in MACRO. Phys. Lett. B 478, 5-13.

[51] K. Abe, N. Abgrall, H. Aihara et al., "The T2K experiment," Nuclear Instruments and Methods in Physics Research, Section A, vol. 659, no. 1, pp. 106–135, 2011.

[52] M. H. Ahn, E. Aliu, S. Andringa et al., "Measurement of neutrino oscillation by the K2K experiment," Physical Review D, vol. 74, no. 7, Article ID 072003, 39 pages, 2006.

[53] I. Ambats et al., (MINOS Collaboration). The MINOS Detectors Technical Design Report,1998.

[54] D. Ayres et al., “Letter of Intent to build an Off-axis Detector to study ν_μ to ν_e oscillations with the NuMI Neutrino Beam,” http://arxiv.org/abs/hep-ex/0210005.

[55] D. Ayres et al., “NOvA: Proposal to build a 30 kiloton off-axis detector to study $\nu_\mu \rightarrow \nu_e$ oscillations in the NuMI beamline,” 2004.

[56] D. Ayres et al., The NOvA Technical Design Report FERMILAB-DESIGN-2007-01, 2007.

[57] M. Sajjad Athar, Jorge G. Morfin, Neutrino(Antineutrino)-Nucleus Interactions in the Shallow- and Deep-Inelastic Scattering Regions, arXiv:2006.08603 (2020).

[58] C. Giunti, C.W. Kim, Fundamentals of Neutrino Physics and Astrophysics (Oxford University Press, New York, NY, 2007)

[59] R. Devenish, A. Cooper-Sarkar, Deep-Inelastic Scattering, Oxford University Press .

[60] Andreopoulos, C. et al, Nuclear Instruments and Methods in Physics Research A 614, 87 (2010).

[61] A. Bodek, U. K. Yang, Higher twist, xi(omega) scaling, and effective LO PDFs for lepton scattering in the few GeV region, J. Phys. G29 (2003) 1899–1906. arXiv:hep-ex/0210024, doi:10.1088/0954-3899/29/8/369.

[62] D. Rein and L. M. Sehgal, “Neutrino excitation of baryon resonances and single pion production,” Ann. Phys., vol. 133, p. 79, 1981.

[63] E. C. Poggio, Helen R. Quinn, and Steven Weinberg. Phys. Rev., D13:1958, 1976.

[64] Dominic Brailsford, DUNE:Status and Perspectives, arXiv:1804.04979v1 (2018).

[65] K. Abeet al.[Hyper-Kamiokande Proto-], “Physics potential of a long-baseline neutrinooscillation experiment using a J-PARC neutrino beam and Hyper-Kamiokande,” PTEP2015, 053C02 (2015) doi:10.1093/ptep/ptv061 [arXiv:1502.05199 [hep-ex]]

[66] Y. Hayato, “A neutrino interaction simulation program library NEUT,” Acta Phys.Polon. B40, 2477 (2009).

[67] T. Golan, J. T. Sobczyk and J. Zmuda, “NuWro:the Wroclaw Monte CarloGenerator of Neutrino Interactions,” Nucl. Phys. Proc. Suppl.229-232, 499 (2012).doi:10.1016/j.nuclphysbps.2012.09.136 .

[68] C. Bronner, JPS Conf. Proc.12, 010025 (2016)

[69] Yasuhiro Nakajima, "Status of FNAL SciBooNE experiment", arXiv:0712.4271v1 [hep-ex] 27 Dec 2007.

[70] J. Hylen et al., NuMI Technical Design Handbook, Internal NuMI report (2003).

[71] R. M. Zwaska, Accelerator Systems and Instrumentation for the NuMI Neutrino Beam, PhD thesis University of Texas at Austin, 2005.

[72] G. Arturo Fiorentini Aguirre (2013), Measurement of ν_{mu} Induced Charged-Current Quasi-Elastic Cross Sections on Polystyrene at $E_{\nu_{mu}}$ $2-10$, Ph.D. Theses, Centro Brasileiro de Pesquisas Fisicas (CBPF), Rio de Janeiro - Brazil.

[73] S. Kopp, The NuMI Neutrino Beam at Fermilab, Department of Physics-University of Texas, Austin, TX 78712, U.S.A.

[74] D.G. Michael et al. (MINOS collaboration), (2008), The Magnetized steel and scintillator calorimeters of the MINOS experiment. Nucl. Inst. and Meth., Phys. Res. Sect. A, 596:190–228.

[75] Richard Gran (2007), The MINERνA Neutrino Interaction Experiment, arXiv:0711.3029.

[76] L. Aliaga et. al.; Design, Calibration, and Performance of the MINERvA Detector; Nucl.Inst.Meth. A473 (2014) 130; arxiv:1305.5199.

[77] R. Fruhwirth, Application of Kalman filtering to track and vertex fitting, Nucl. Instrum. Meth. A262 (1987) 444–450. doi:10.1016/0168-9002(87)90887-4.

[78] W. D. Hulsbergen, Decay chain fitting with a Kalman filter, Nuclear Instruments and Methods in Physics Research A 552 (2005) 566–575. doi:10.1016/j.nima.2005.06.078.

[79] Anne Norrick, Calorimetry in MINERνA , MINERνA 's Technical Note 12851-v4.

[80] CERN, ROOT Data Anaysis Framework, https://root.cern.ch/root/htmldoc/guides/users-guide/ROOTUsersGuide.html.

[81] A. Filkins et al. (MINERνA νA Collaboration),Phys. Rev. D 101, 112007

[82] J. Mousseau, GENIE cross section weight note. MINERA internal technical document, DocDB 7565 (2014)

[83] B. Tice, Analysis of charged current neutrino interactions on nuclear targets. MINERA internal technical document, DocDB 8854 (2013)

[84] Leonidas Aliaga Soplin, "Neutrino Flux prediction for the NuMI beamline",fermilab-thesis-2016-03.

[85] Ž. Pavlović, "Observation of disappearance of muon neutrinos in the NuMI beam", Ph.D. thesis, FERMILAB-THESIS-2008-59, University of Texas at Austin, (2008). 99, 100, 101 (2008).

[86] A. Norrick, Our detector is too heavy: The saga, internal Document (2016). URL https://minerva-docdb.fnal.gov/cgi-bin/private/RetrieveFile?docid=11686

[87] Anushree Ghosh,"MINOS matched muons tracking efficiency at medium energy", https://minerva-docdb.fnal.gov/cgi-bin/private/RetrieveFile?docid=20760&filename=quadrant_minos_matched_tracking_efficiency%20_v2%202.pdf&version=1

[88] G. D'Agostini, A multidimensional unfolding method based on Bayes' theorem. Nucl. Instrum. Methods Phys. Res. Sect. A 362, 487–498 (1995)

[89] Wospakrik, Marianette Octovina, "Measurement of Neutrino Absolute Deep Inelastic Scattering Cross Section in Iron, Lead, Carbon, and Plastic using MINERνA detector at $E_\nu = 6$ GeV", FERMILAB-THESIS-2018-22

[90] Joel Mousseau, "First Search for the EMC Effect and Nuclear Shadowing in Neutrino Nucleus Deep Inelastic Scattering at MINERvA", DOI: 10.2172/1226352, 10.1007/978-3-319-44841-1 FERMILAB-THESIS-2015-27

[91] R. P. Feynman, M. Kislinger, and F. Ravndal, "Current matrix elements from a relativistic quark model," Phys. Rev., vol. D3, pp. 2706–2732, 1971.

[92] K. Kovarik et al. "nCTEQ15: Global analysis of nuclear parton distributions with uncertainties in the CTEQ framework", Phys. Rev. D 93, 085037 – Published 28 April 2016.

[93] A. Filkins et al. (MINERνA Collaboration), "Double-differential inclusive charged-current ν_μ cross sections on hydrocarbon in MINERvA at $< E_\nu >\sim 3.5$ GeV", Phys. Rev. D 101, 112007 – Published 23 June 2020.